POLITECNICO DI MILANO

School of Industrial and Information Engineering

Master of Science in Electrical Engineering

OPTIMIZATION OF SYNCHRONOUS RELUCTANCE MOTOR DESIGN AND REDUCTION OF TORQUE RIPPLE BY HARMONIC INJECTION.

Supervisor: Prof. Antonio Di Gerlando

Master thesis dissertation of:

Vikash prabhu palaneeswaran (10625061)

Academic year :2019-2020

ACKNOWLEDGEMENT

I would like to express my special thanks of gratitude to my Professor Antonio Di Gerlando my thesis professor, for his support and guidance throughout the Master thesis as well as the university Politecnico Di Milano who gave me the golden opportunity to do this wonderful project on the topic, which also helped me in doing a lot of Research and I came to know about so many new things.

Milano, December 2020

General Introduction

The present thesis aims to the performance enhancement of the Synchronous Reluctance Machine (SynRM) by machine design and current harmonics injection. In recent years, the need to build low-cost yet efficient machines with high performance essential in several domains especially in the automotive domain [1]. A renewed interest in the reluctance machines has emerged, and in particular in the SynRM [2, 3]. The SynRM has a stator similar to that of an Induction Machine (IM). However, the absence of hard magnetic or conductor material in the rotor makes it robust, cheap and easy to manufacture. In addition, the absence of winding losses in the rotor makes the heat management easier in comparison with the IM. Nevertheless, the SynRM has to overcome several obstacles to become a viable alternative to other AC drives in Variable Speed Drive (VSD) applications. The most important performance obstacles are:

- Low power factor
- Low power and torque densities
- High torque ripple
- Low speed range

This thesis handles mainly the torque density and the torque ripple of the SynRM, and focuses on the machine design and the current harmonics injection and their effect of the whole machine torque-speed envelope.

Chapter 1 introduces the electrical machine in the traction system of the electric vehicle and the main challenges encountered and trends. The SynRM will be also introduced for a VSD application with the several limitations it faces on the whole operation diagram and in particular on its torque-speed envelope.

Chapter 2 proposes an analytical design procedure of the SynRM rotor that can be adapted to different rated power. The design procedure is based on the flux lines in a

solid rotor and the uniformity of the field in the rotor in order to deliver an important machine torque density. This design will be applied to a specific case and compared to another SynRM rotor design. The study of several elements like the ribs and bridges that hold the structure of the rotor and keeps it mechanically strong will be presented as well. A final design is proposed at the end of the chapter and Finite Elements (FE) simulations are used to identify the performance of the SynRM.

Chapter 3 shows a parametric optimization study of the SynRM in order to enhance its performance, in particular, the torque ripple. Therefore, an optimization problem is formalized and treated in order to obtain a better performing machine with lower torque ripple without impacting significantly the other performance criteria of the machine like the torque density and the saliency ratio. At the end of the optimization study, a design is proposed and compared with the design obtained from the analytical procedure in chapter 2.

Chapter 4 deals with the harmonics injection in the phase currents of the SynRM and their impact on the machine average torque and the torque ripple. A general m-phase machine will be used to introduce the current harmonics interaction with the inductance spacial harmonics. Afterwards, the harmonics injection will be applied in the case 2-phase machine and the results show that the harmonics injection have a positive impact in reducing the machine torque ripple. Then, the control issues of injecting harmonics in the phase currents will be presented and the controllers will be synthesized and evaluated using a developed machine model.

Chapter 5 validates experimentally the analytical design procedure and the parametric optimization for the SynRM rotor design. At first, the test bench is presented and the machine is characterized. The performance envelope is validated afterwards and the designs based on the analytical procedure and the optimization study are compared. Finally, the experimental results of the harmonics injection in the phase current are shown.

Chapter 6 proposes a SynRM design for a traction application. First, the electromagnetic specifications linked to traction application are shown. Then, a general optimization method that handles the rotor and the stator is proposed to optimize the machine torque density at a constant current density. The variation of the machine length and the number of conductors is studied in order to obtain a machine that meets the specifications needed.

Chapter 1

Context of the Thesis

Contents

1.1 EV Electric Machines: An Overview

Electric machines represent an essential element in Electric Vehicles (EVs). They can be used in Hybrid Electric Vehicles (HEVs) to operate jointly with an Internal Combustion Engine (ICE) to propel the vehicle. They can also function with a hydrogen fuel cell to propel the hydrogen car. In the case of the Battery Electric Vehicle (BEV or mostly known as the EV), the electric machine uses the energy stored in a battery and provides all the traction power. Besides the positive effects on pollution emissions, the EV is interesting by its high power density and good efficiency over a wide speed range.

1.1.1 Electric Traction System

Three main units constitute the traction system of a BEV:

- Battery unit
- Power electronics unit
- Propulsion unit

The battery unit uses battery cells to store the electric energy. The propulsion unit is made of an electric machine and a reduction gear and converts the electric energy into mechanical energy to propel the vehicle. In traction operation, the battery unit feeds the propulsion unit and moves the car forward. In braking operation, the battery recuperates the electric energy transformed from the excess kinetic energy of the car.

These operations and the corresponding energy flow are controlled by the power electronics unit which is mainly made of an inverter. The role of this inverter is to convert the DC voltage in the battery to AC voltage in order to create torque in the propulsion unit or to convert AC voltage into DC to recharge the battery in the breaking operation. Figure 1.1 shows the mentioned three units in a Renault ZOE car.

Three main criteria are crucial in the EVs market development:

- Power
- Cost
- Driving range

The maximum required EV power is set by the application and vary from around 50 kW for small highway-capable cars upto 600 kW for performance sports cars. The

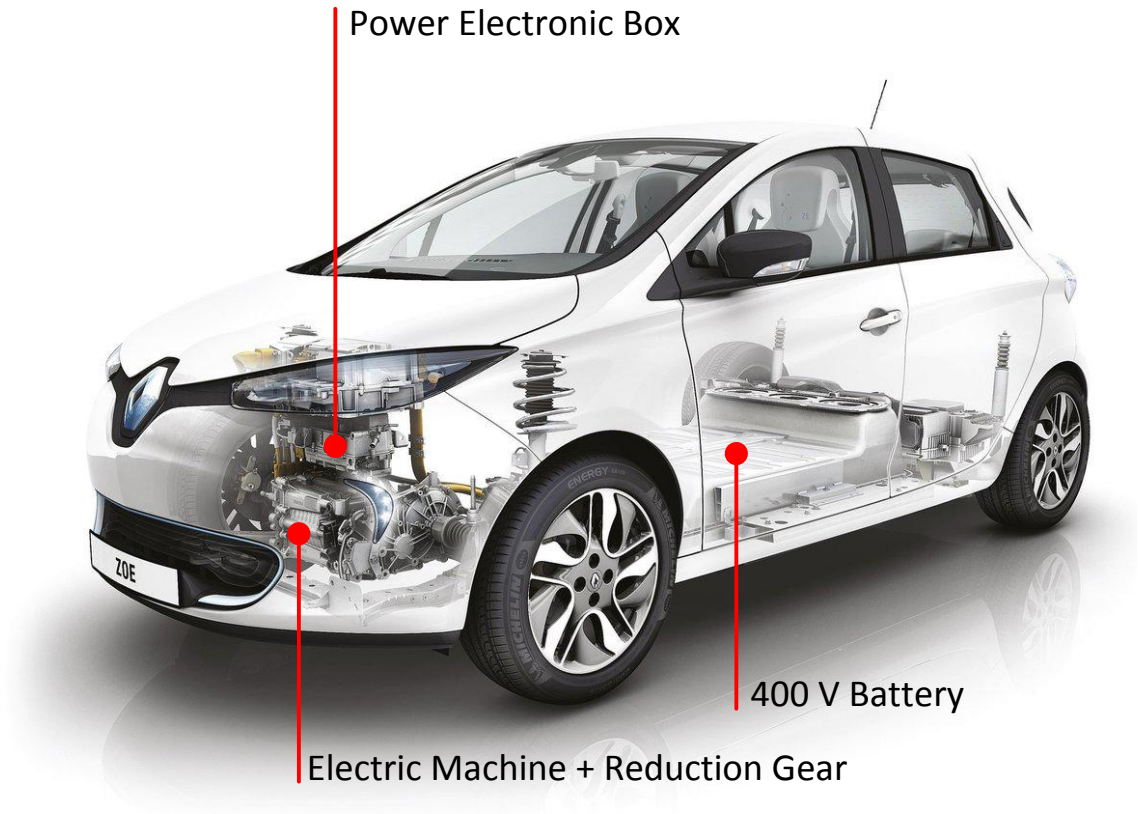

Fig. 1.1 Electric traction system in a Renault ZOE architecture.

EV driving range is determined by the battery storage capacity, the efficiency of the traction system and by the EV traction power. The energy storage capacity of the battery is typically around 20 kWh for small highway-capable cars and goes up to 85 kWh for bigger cars. EV batteries are expensive and significantly impact the vehicle's overall cost, weight an volume. Therefore, many studies have dealt with the issue of the batteries and how to make them more efficient and less expensive. The technology of batteries have considerably evolved in the 20 passed years from technologies based on lead acid in the 1990's to the lithium-ion that dominates the battery market technology today [4].

Another research axis deals with the power electronics and the propulsion units. Four trends are dealt with in order to have a more competitive electric traction system: cost reduction, weight reduction, volume reduction and energy efficiency increase.

The main aim of the weight reduction of the units is to reduce the energy required to accelerate the car. This will lead to a decrease of the energy required and to a better driving range. The energy efficiency increase is achieved by reducing the power

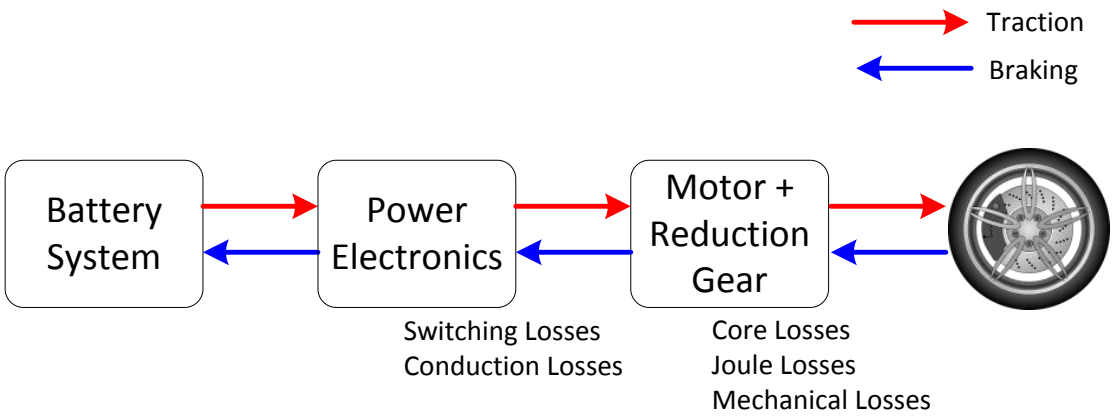

Fig. 1.2 Power losses in the power electronics and the propulsion units.

losses in both the propulsion unit and the power electronics unit. These losses can be summarized as shown on figure 1.2 by the switching losses and the conduction losses for the power electronics unit, and the core losses, the Joule's losses and the mechanical losses in the propulsion unit.

1.1.2 Traction System Performance Requirements

In addition to its cost effectiveness and its energy efficiency, the traction system has performance requirements to respect. Figure 1.3 shows an example of the torque versus speed performance requirements of an EV traction system. The traction system should provide a wide speed range since a multiple-ratio gearbox is not desirable. In addition, a high torque is required to ensure a high acceleration and hill climbing capabilities. This high torque should be acquired for a short period of time (typically $30s$) since the thermal constraints of the machine limits the use of this torque.

High machine efficiency (above 90%) has to be acquired for the overall operation zone of the machine. That's why several driving cycles are introduced to evaluate a design's efficiency. A standard used cycle is the New European Driving Cycle (NEDC) that imposes a speed profile to be able to asses and compare different machine technologies designs for their efficiency and energy consumption (figure 1.4).

Furthermore, the propulsion unit contributes highly to the acoustic and vibrations emissions in the EV which has to be limited in an EV application. For instance, the reduction gear emits an acute sound that should be accounted for. The radial magnetic excitation in the machine's airpag (the gap between the stator and the rotor) actively increases the acoustic noise. Moreover, the machine torque ripple that is transmitted

through the machine bearings has a direct impact on the noise and the vibrations emissions. In addition, the torque ripple reduces the bearings' reliability and is highly undesirable in the propulsion unit.

The traction system in general and the propulsion unit in particular should follow the standards instated by the companies or the states to increase the recyclability of the vehicle. This is achieved through the use of reusable or recyclable material in the traction system without negatively impacting the system performance.

In [5], the EV electric machine requirements are summarized as the following:

- High instant power and high power density
- High torque at low speeds for starting and climbing, as well as high power at high speed for cruising
- Very wide speed range including constant-torque and constant-power regions
- Fast torque response
- High efficiency over wide speed and torque ranges
- High efficiency for regenerative braking
- High reliability and robustness for various vehicle operating conditions
- Reasonable cost

The following requirements can be added to have a more complete list:

- Low torque ripple over wide speed and torque ranges
- Low noise and vibrations emissions
- Low electromagnetic interference with other systems
- High recyclability

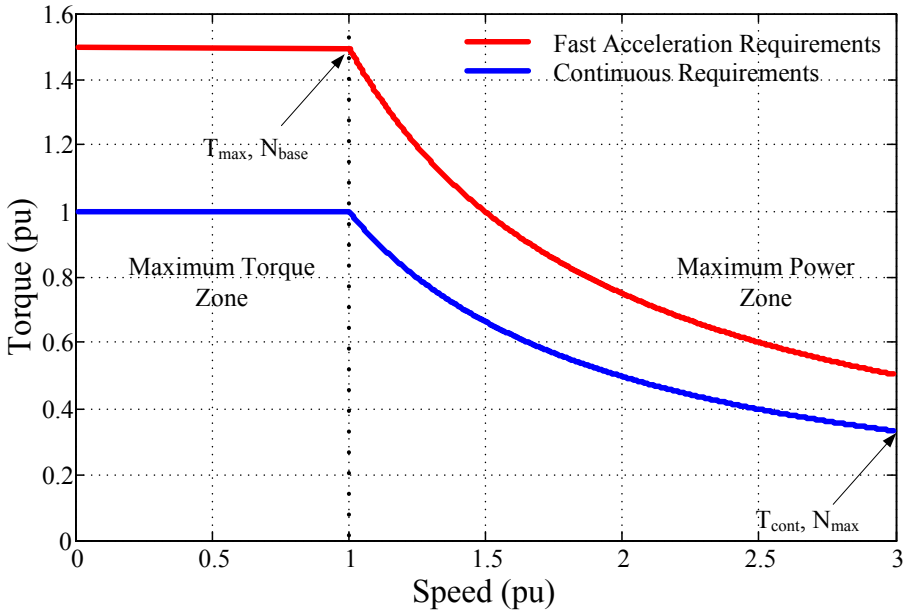

Fig. 1.3 Torque-speed requirements of an EV electric machine.

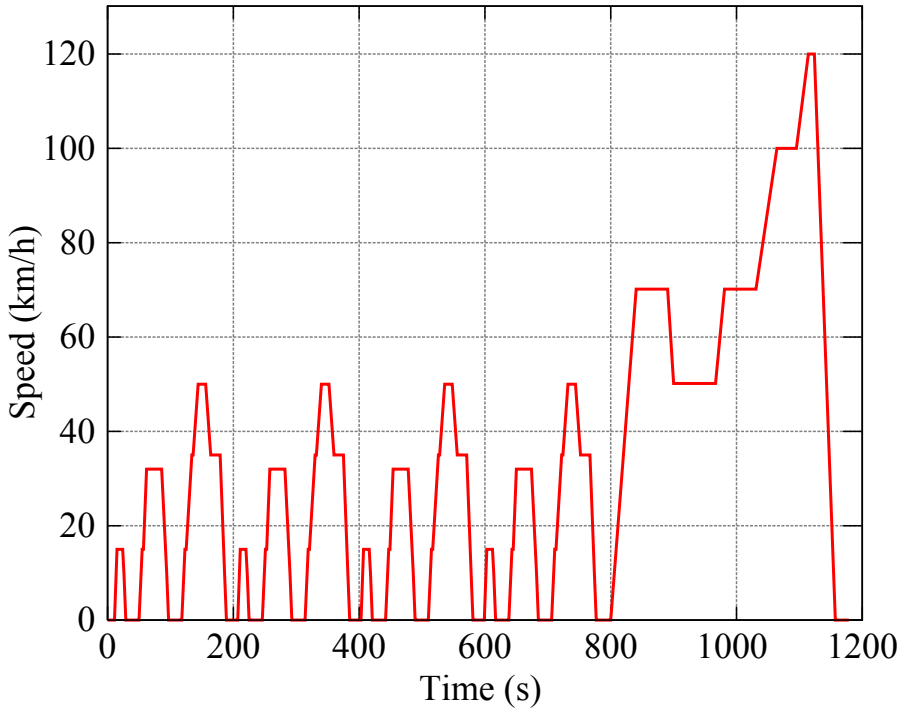

Fig. 1.4 The NEDC cycle for the vehicle speed in km/h.

1.1.3 Electric Machine Technologies in EVs

The presence of an electric motor in an EV can be traced back to the 1820's [6]. However, EVs stayed in niche market like urban delivery vehicles, and not until the 1980's that the interest renewed on the subject after the consecutive oil shocks and the pollution problems the world faces. For this new generation of EVs, the AC machine is widely used since there was a considerable evolution in the power electronics to make the control of the machine possible.

The most adopted technology in propulsion units is the rare-earth Permanent Magnet Synchronous Machine (PMSM) due to its high power density. Table 1.1 shows the dominance of the PMSM in highway capable EVs. However, the volatility of the rare-earth material and their unpredictable cost evolution lead to the search of alternative solutions [7]. Renault has chosen the Externally Excited Synchronous Machine (EESM), also known as the synchronous brushed motor, for their fleet of EVs [4]. Moreover, the Induction Machine (IM), also known as the asynchronous machine or the squirrel cage machine, has been used by Tesla to equip their model S and the roadster [4].

Nowadays, for a vehicle manufacturer, the choice has to be made between compactness with the PMSM since it delivers the highest torque and power density, robustness and cost effectiveness with the IM or controllability and cost effectiveness of the EESM. However, research attempts are present to find a new alternative of these three present technologies.

1.1.4 EV Traction Motor Trends

Although AC machines have been discovered more than a century ago, integrating them in EVs is a recent matter. Therefore, many studies are being made on how to optimize the AC traction machine for EV usage. Four main axes are dealt with in these diverse studies:

- Increasing the specific power (kW/kg)
- Reducing cost ($\$/kW$)
- Increasing the power density (kW/l)
- Increasing the system efficiency

Table 1.2 shows the targets set by the US department of energy for electric machines in EV traction systems for 2020. In order to increase the specific power and the power

	Motor Technology	Power (kW)	Torque (Nm)
Renault ZOE	EESM	65	220
Renault Fluence	EESM	70	226
Nissan Leaf	PMSM	80	280
BMW i3	PMSM	130	250
Mitsubishi i-MIEV	PMSM	47	180
Fiat 500-e	PMSM	80	196
Ford Focus e	PMSM	107	245
Honda Fit EV	PMSM	92	256
Tesla S	IM	270	440
Volkswagen e-Golf	PMSM	85	270
Volkswagen e-Up	PMSM	60	210

Table 1.1 Electric motor technologies and their performance in highway capable EVs.

density of electric machines, an alternative consists of increasing the machine speed. However, this increase of the machine speed introduces supplementary issues to the machine design like mechanical strength and system vibrations. In addition, high speeds presents supplementary challenges in the machine control or can increase the Pulse Width Modulation (PWM) signal frequency which increases the commutations losses of the power electronics. Another research axis for increasing the specific power is to reduce the volume of the machine at a given torque. For that, a higher slot fill is required as well as better heat management. Figure 1.5 shows the current status of specific power for machine in diverse applications and their maximal rotation speed.

The losses present in the machine are the core losses in the iron (hysteresis losses and eddy current losses), the Joule losses in the copper and the mechanical losses (principally aerodynamic losses). The core losses can be reduced either by reducing the system frequency or by using low-loss ferromagnetic material. Reducing the system frequency is somewhat tricky because it can decrease the machine rotation speed and the output power if the pole pair number stays constant. However, if low-loss ferromagnetic material are introduced in the automotive industry, it should come without increasing the cost of the raw material and the manufacturing. Concerning the mechanical losses in the machine, there are some techniques that reduce the aerodynamic losses like using smooth rotor and stator surfaces. The reduction gear

Year	Cost ($\$/kW$)	Specific Power (kW/kg)	Power Density (kW/l)	Power Electronics and Machine Efficiency
2010	11.1	1.2	3.7	>90%
2012	10	1.24	4	>91%
2015	7	1.3	5	>93%
2020	4.7	1.6	5.7	>94%

Table 1.2 EV electric machines technical Targets according the US departement of energy [8].

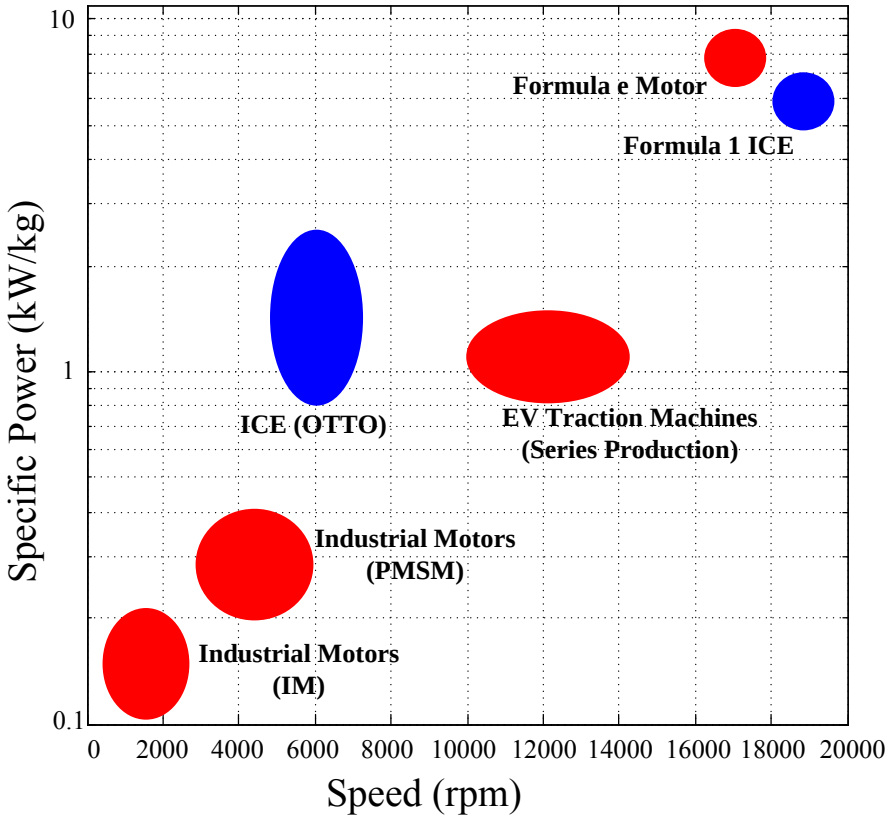

Fig. 1.5 Specific power versus maximum speed for electric machines and ICEs in different applications [9, 10].

and the machine bearings contribute to the mechanical losses in the propulsion unit, mainly, due to friction. These losses can be reduced either by using high performance

ceramic material or optimized dimensions for the bearings, or using a low viscosity oil in the reduction gear.

Another challenge lies in reducing the machine cost to become more competitive compared to the ICE vehicle. This can be achieved by several means. The manufacturing cost of machines should be reduced while keeping a precise automated industrialization. In addition, the material used in the machine is an important element of the machine cost. For instance, an important axis of the development in the cost reduction lies on the reduction or the elimination of rare earth permanent magnets.

1.1.5 Comparison of Different Machine Technologies for the Next Generation of EVs

1.1.5.1 Rare Earth Permanent Magnet Synchronous Machines

The presence of rare earth permanent magnets, like the NeFeB, in the synchronous machines create a high intensity field in the airgap without the presence of excitation. Therefore, the specific density of such a machine is high. However, the permanent magnets are temperature sensitive. Not only does their performance decrease with the increase of the operating temperature, they risk demagnetizing with high temperatures. Moreover, in case of machine fault such as a winding short-circuit, the energy stays in the rotor which in case of continued use could damage the machine winding and could provoke a system instability.

The permanent magnets in a sinusoidal PMSM can have one of two configurations:

- Internal Permanent Magnet (IPM) (refer to figure 1.6)
- Surface-mounted Permanent Magnet (SPM)

The IPM has shown a better overload capability than that of a SPM, but more losses at low speed [11]. On the other hand, The Brush-Less DC (BLDC) PMSM has a trapezoidal magnet excitation and requires a rectangular current waveforms. However, this configuration has a reduced field weakening zone compared to the IPM, a reason for which the IPM is widely used in EV applications. However, at high speed, Joules losses caused by currents needed to reduce the permanent magnet field density increase and the machine efficiency decreases [12]. The PMSM has several advantages that are suitable for EV applications, they can be summarized as the following:

- High efficiency

- Wide speed range
- Low noise
- Absence of Joule losses in the rotor
- Compact
- Fast torque response

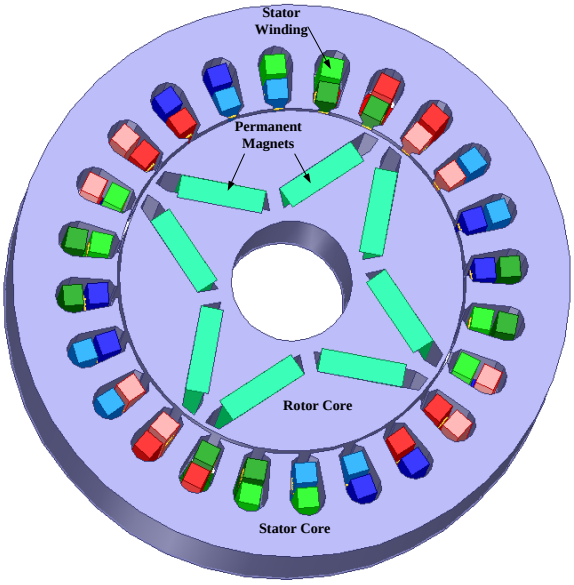

Fig. 1.6 Configuration of an IPM synchronous machine.

1.1.5.2 Non Rare Earth Permanent Magnet Synchronous Machines

Substituting the rare earth PMs by non-rare earth ones is a solution to overcome the volatility and uncertainty of the PM prices. However, the remanent field density of non rare earth PMs is considerably less than that of rare earth PMs. For instance, Ferrite PMs, which are good candidates to replace the NeFeB PMs, can have a remanence as high as $0.47T$ in comparison to $1.5T$ of rare earth material. This technology is not yet used in the automotive market. However, many attempts are being made so that it can be a viable alternative to rare the earth PMSM [1].

1.1.5.3 Externally Excited Synchronous Machine

The EESM is a machine with a double excitation. The stator is fed with sinusoidal currents in order to create a rotating field, while the rotor is fed by a DC current to create the rotor excitation (refer to figure 1.7). Thus, this machine does not contain permanent magnets. The coil in the rotor is connected to a slip ring. A DC/DC converter is required as a supplement with respect to PMSM to ensure the rotor excitation. This conversion allows the regulation of the flux in the rotor to be able to better operate at high speeds. From a mechanical point of view, this machine has a robust structure and can acquire high speeds. However, the rotor windings contributes to the overall Joules losses where the heat should be evacuated.

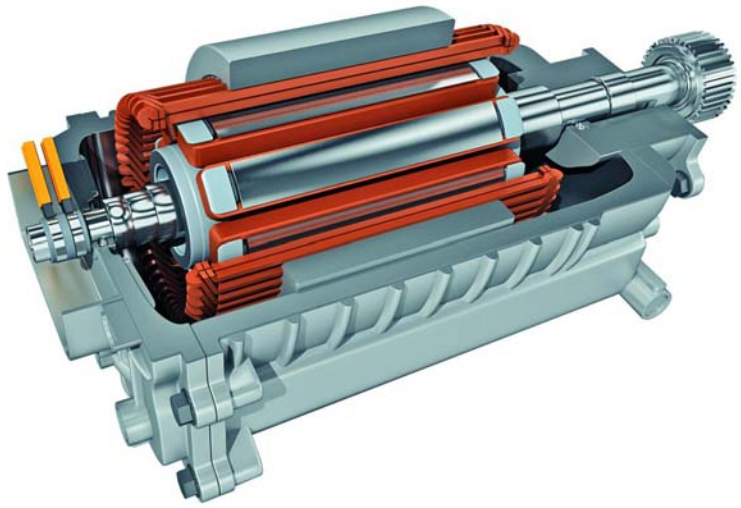

Fig. 1.7 Continental EESM for traction applications.

1.1.5.4 Induction Machines

The IM is currently used by Renault to equip the Renault Twizy and by Tesla to equip the Model S and the Tesla Roadster. The main advantage is that the IM does not contain permanent magnets. The torque production is ensured by the induced currents in the rotor cage when the speeds of the rotor and the stator are different. The cage is usually made of aluminium or of copper for better performance. It has been reported to give a smaller specific power with respect to PMSM. However, the cost of the machine and the overall traction system remains cheaper [13].

1.1.5.5 Switched Reluctance Machines

Switched Reluctance Machines (SRMs)(figure 1.8) are also permanent magnet free and are considered to be a good candidate for EV traction systems. However, until this day, this technology has not been used yet in a commercial car. The machine stator is different from the previously mentioned machine technologies and uses step-by-step control to create torque. The SRM has recorded a high specific power and high speed capabilities. Its structure is robust since it contains just steel in its rotor. Nevertheless, its complex control, its high acoustic noise and its unusual power electronics architecture have been major obstacles to implement it in EV systems. Many research projects work on making this technology feasible for EV drive trains [1, 14–20].

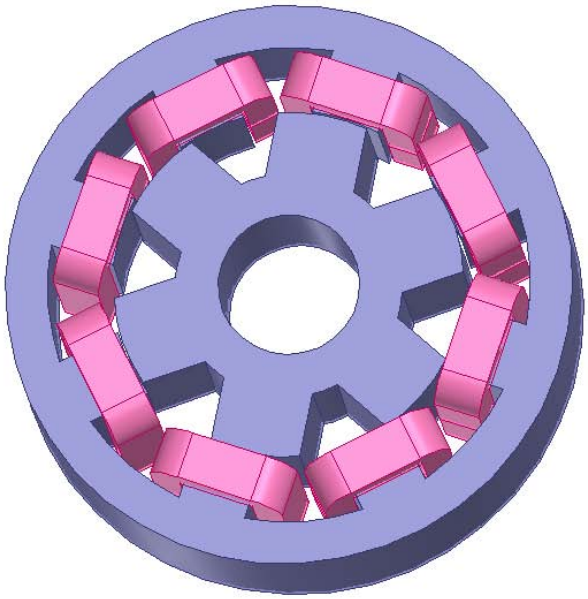

Fig. 1.8 Switched reluctance machine in an 8/6 configuration.

1.1.5.6 Synchronous Reluctance Machines

The Synchronous Reluctance Machine (SynRM) (figure 1.9) uses also the reluctance concept to create motion and torque. Like SRMs, the SynRM does not contain PMs. It is fed by sinusoidal currents in order to create a rotating field as in the case of the IM and the PMSM. It has a robust structure where the stator is similar than that of an IM and the rotor contains neither magnets nor copper windings. Therefore, a higher efficiency can be obtained with respect to the IM due to the absence of the Joule losses

in the rotor. Potentially, this machine technology could be a viable alternative for low cost traction solutions. However, the machine has several main problems: a relative high torque ripple [21, 22], a low power density, a low power factor and a reduced field weakening zone.

Fig. 1.9 Synchronous reluctance machine rotor with 4-pole configuration [23].

1.1.5.7 Quantitative Performance Comparison

Comparison between IM, PMSM and SRM Machines

Many literature studies have dealt with the comparison of machine technologies for HEVs and EVs. In [12], 4 machine technologies are compared for HEV applications: a DC machine, an IM machine, a PMSM machine and a SRM. The main disadvantage in a DC machine is its brushes that require maintenance and the hard commutation it undergoes. This technology is fading away for the next generation EVs. Table 1.3 shows the dimensions and the performance of the IM, PMSM and SRM machines for a nominal speed of 3000 rpm, a nominal power of 30 kW and a nominal voltage of 400 V. The power to volume ratio of the PMSM is highly dominant. In addition, the PMSM is the most efficient. However, in another study [24], the focus is predominantly on the specific power (power to weight ratio) of the machine technologies. Table 1.4 shows the comparison done between the IM, the PMSM (used as the 2^{nd} generation Prius machine) and the SRM's specific power. The SRM shows a competitive specific power that is higher than that of a PMSM. In the same study, the torque density (torque to weight ratio) is examined for the three machines at two operation speeds: 1500 rpm and 6000 rpm. Table 1.5 shows that the SRM gives the best results at both speeds with respect to the other two machines.

	p	Eff_{max} (%)	D_r (mm)	L_a (mm)	D_o (mm)	L_T (mm)	V (dm^3)	PV ratio (kW/dm^3)
IM	2	89	162	127	258	232	12.1	2.5
PMSM	6	97	137	141	196	162	4.9	6.1
SRM	12/8	88	159	159	269	207	11.8	2.6

Table 1.3 Analytical comparison of the power to volume ratio from where p: pole pairs number, Eff_{max}: maximum efficiency, D_r: rotor diameter, L_a: active length, D_o: outer diameter, L_T: total length with end windings, V: machine volume and PV ratio: power to volume ratio [12].

	D_o (mm)	D_{shaft} (mm)	D_r (mm)	g (mm)	L_a (mm)	W_T (kg)	Specific Power (kW/kg)
IM	269	111	180	1.5	84	36.25	1.38
PMSM	269	111	160.5	0.73	84	31.16	1.6
SRM	269	111	170	0.3	84	26.71	1.88

Table 1.4 Specific power comparison from where D_o: outer diameter, D_{shaft}: shaft diameter, D_r: rotor diameter, g: airgap length, L_a: active length and W_T: total weight [24].

SynRM and IM Comparison

Even if the stator of the SynRM and the IM are similar, the absence of the copper in the SynRM's rotor makes the two machine different. The IM structure has two loss sources that the SynRM does not have: the slip losses and the rotor Joules losses. Many studies have compared the IM to the SynRM that found that the SynRM is competitive with respect to the IM. For instance, in [25, 26], the authors compared analytically the performance of the two machines and experimentally tested a 2.2 kW and a 4 kW machine. The rated torque shown in the study is higher in the case of the SynRM between 10% upto 15% the IM rated torque. In [2], a heat run test is run on a 90 kW IM and SynRM. The tested machines have a nominal speed of 1500 rpm and a rated torque of around 570 Nm. No major improvement has been noted in this study on the rated torque at the same current input. However, the SynRM efficiency is 1.5% higher on the tested operation point. In addition, the temperature rise of the SynRM is lower than the case of the IM due to the absence of Joule losses in the rotor. Thus,

	Torque (Nm)	Iron Loss (W)	Copper Loss (W)	Efficiency (%)	Torque Density (Nm/kg)
Speed = 1500 rpm					
IM	297	148	8591	83.1	8.2
PMSM	303	198	4328	91.3	9.7
SRM	294	404	7653	85.2	11
Speed = 6000 rpm					
IM	50.8	439	730	95.2	1.4
PMSM	45.6	953	219	96.1	1.46
SRM	52.1	4074	306	88.2	1.95

Table 1.5 Torque density comparison from for the IM, the PMSM and the SRM for two speeds: less than the nominal speed and greater than the nominal speed (field weakening zone) [24].

at the same temperature rise the stator currents in the SynRM can be increased to lead to more torque.

The SynRM shows competitive performance in comparison with the IM below nominal speed. However, the traction application requires high field weakening capabilities. Therefore, the whole torque-speed range should be studied in order to have a broader idea on the SynRM performance. Nevertheless, the SynRM has acquired a particular interest for Variable Speed Drive (VSD) applications in general and low-cost traction applications in particular in recent years. For instance, in [27], a SynRM sizing methodology is proposed for an automotive application.

1.1.5.8 Machine Selection for the Thesis

A main tendency in finding a new solution for EV traction machines is to reduce or eliminate the rare-earth permanent magnets. In this regard, alternatives of the rare-earth PMSM are being investigated.

The SynRM can be a good candidate for EV applications. It is a robust machine, uses no permanent magnets and is easy to control. In addition, it is easy to manufacture. Compared to the SRM, the SynRM has all of its advantages except the SRM field weakening capability. Furthermore, the SynRM produces less noise and has a simpler control than that of a SRM.

For all these reasons, the SynRM has the capability to be an alternative for traction machines if better performance is reached on the following levels:

- reducing the SynRM torque ripple,
- increasing the machine power factor to reduce the inverter size,
- increasing its speed range,
- and increasing its power and torque densities.

Therefore, the SynRM will be chosen in this work, and the machine design as well as its control will be investigated in the goal to improve the machine performance.

1.2 SynRM in a Variable Speed Drive

The electric traction system is a particular VSD drive with a broad speed range. The aim of this section is to introduce the SynRM concept, properties and operation diagram for a VSD application in order to build an idea on the SynRM in traction systems.

1.2.1 SynRM Concept

The SynRM is a machine that uses the reluctance concept to create torque. This concept can be traced back to the 1830's [28]. However, with Kostko's paper in 1923 [29], the fundamentals of the SynRM were introduced. The main idea behind the machine is to introduce an anisotropic rotor to create saliency. When the stator is powered, the winding in the stator creates an electromagnetic field and the axis of minimal reluctance of the anisotropic rotor will have the tendency to align with the stator field by creating a field distortion.

Figure 1.10(a) shows the flux lines in the case where there is no rotor. The flux lines are created by the stator windings to be parallel to the y-axis. Figure 1.10(b) shows that the flux lines in the case where an isotropic rotor is introduced stay parallel to the y-axis. However, on figure 1.10(c), an anisotropic rotor is introduced and the flux lines change their tendency towards the the axis of the minimal magnetic reluctance (the direct axis). When a rotating field is created by injection sinusoidal currents, the rotor will turn with the same rotation speed of the field and a torque with a non-zero average value is created.

Figure 1.11 shows a rotor pole of a 4-pole Transversally Laminated Anisotropy (TLA) rotor SynRM. The flux segments and the flux segmets are introduced to canalize the flux in the machine as seen on figure 1.12. Moreover, the ribs and the bridges are present to ensure the mechanical strength of the rotor.

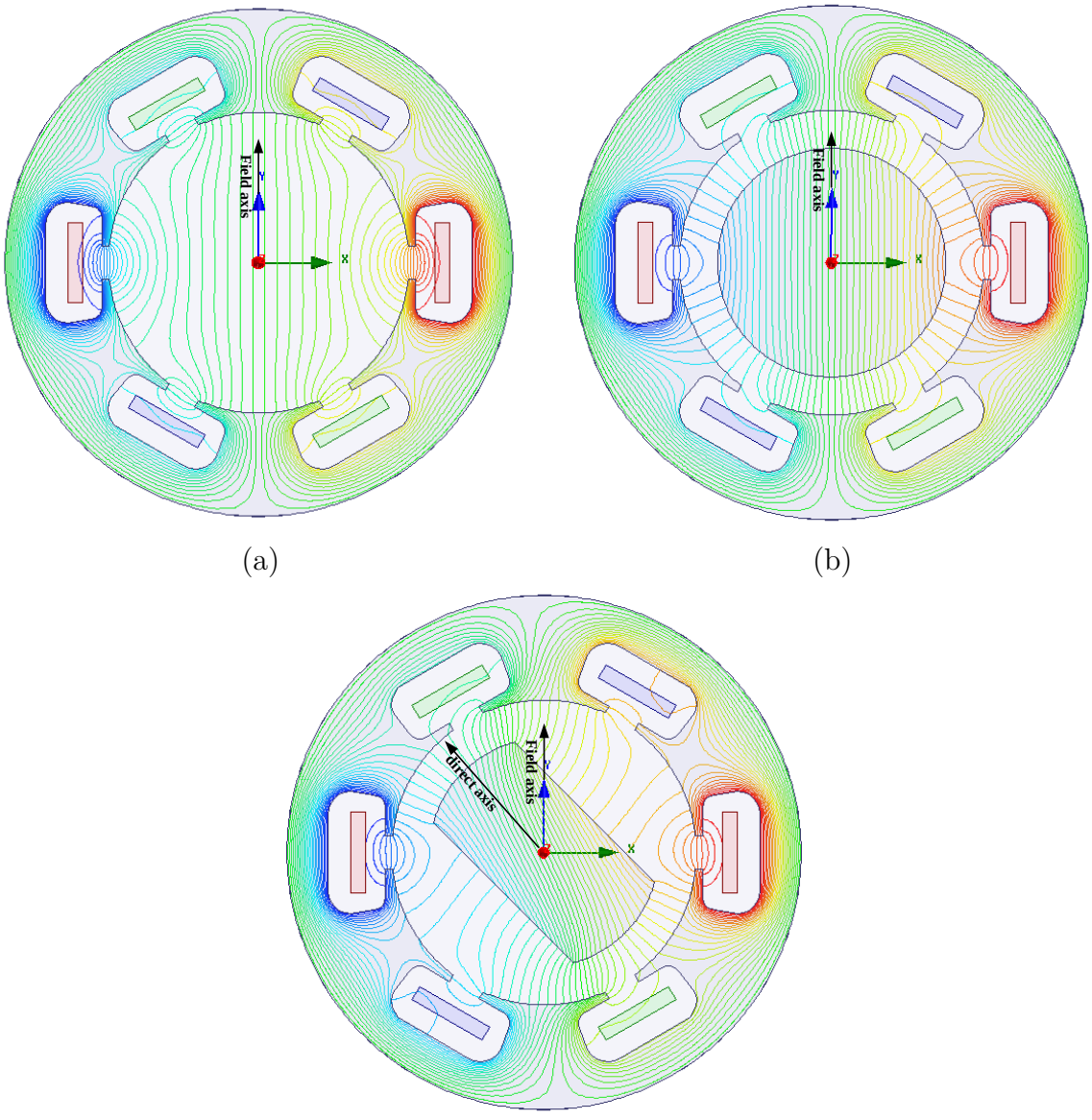

(a) (b)

(c)

Fig. 1.10 Flux lines in: (a) no rotor case, (b) an isotropic rotor and (c) an anistropic rotor.

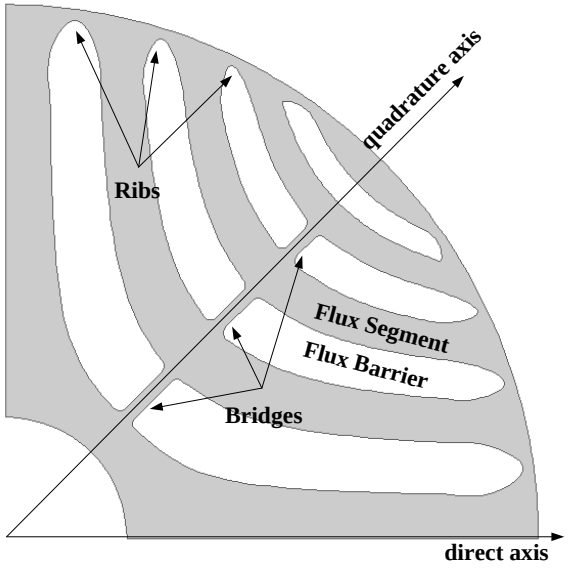

Fig. 1.11 Pole representation of a 4-pole transversally laminated anistropic rotor SynRM and its different elements.

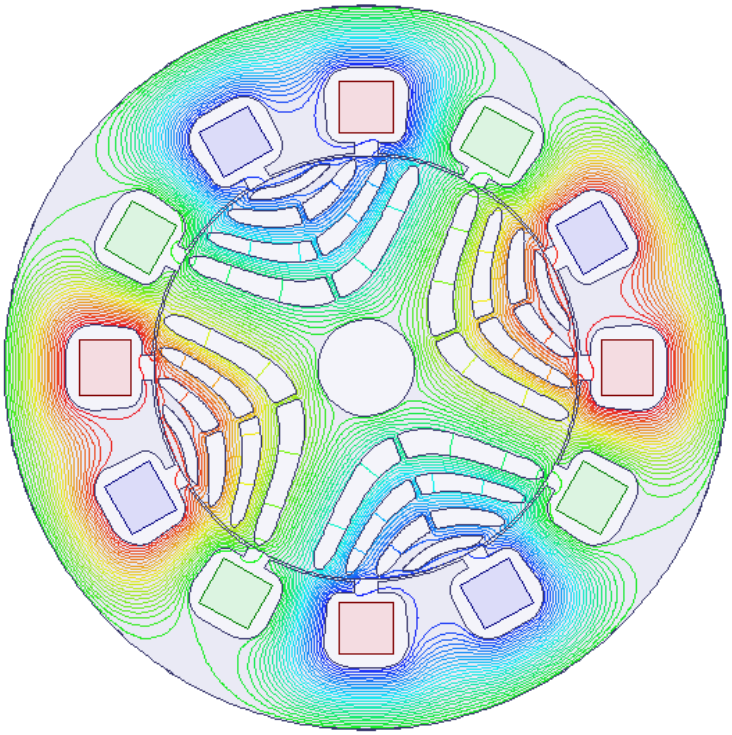

Fig. 1.12 Flux lines in a 4-pole transversally laminated anistropic rotor SynRM.

1.2.2 Vector Diagram and Machine Equations in Park's Reference

Many studies have dealt with SynRM equations in Park's dq synchronous reference. The direct axis (d-axis) is considered as the axis of least reluctance and quadrature axis (q-axis) is the axis of highest reluctance as shown on figure 1.11 for a TLA rotor SynRM.

The stator voltage (V_s), the stator induced voltage (IV), and the stator flux (λ) can be defined by the following equation in the machine steady state [30]:

$$\begin{aligned} V_s &= V_d + jV_q = IV + R_s I_s \\ IV &= j\omega_e \lambda \\ \lambda &= \lambda_d + j\lambda_q = L_d I_d + jL_q I_q \end{aligned} \tag{1.1}$$

The electromagnetic torque equation derived from the co-energy of the system can be written as follows:

$$\begin{aligned} T_{avg} &= \frac{m}{2} p(\lambda_d I_q - \lambda_q I_d) \\ &= \frac{m}{2} p(L_d - L_q) I_d I_q \\ &= \frac{m}{2}\frac{p}{2}(L_d - L_q) I_s^2 sin2\phi \end{aligned} \tag{1.2}$$

where m is the phase number, p is the pole pair number and ϕ is the angle between the current vector and the d-axis. From (1.2), the theoretical angle for Maximal Torque per Ampere (MPTA) of 45 deg is deduced. However, this angle will be re-evaluated when saturation and core losses will be taken into account.

The torque ripple can be expressed as the following:

$$T_{ripple} = \frac{max(Torque) - min(Torque)}{T_{avg}} = \frac{\Delta T}{T_{avg}} \tag{1.3}$$

The saliency ratio (ξ) of the machine is defined by the following equation:

$$\xi = \frac{L_d}{L_q} \tag{1.4}$$

The maximal machine Power Factor (PF) is shown in [31] and is dependant on the machine saliency ratio as in following:

$$cos\phi|_{max} = \frac{\xi - 1}{\xi + 1} \tag{1.5}$$

The vector diagram in the dq reference is shown on figure 1.13.

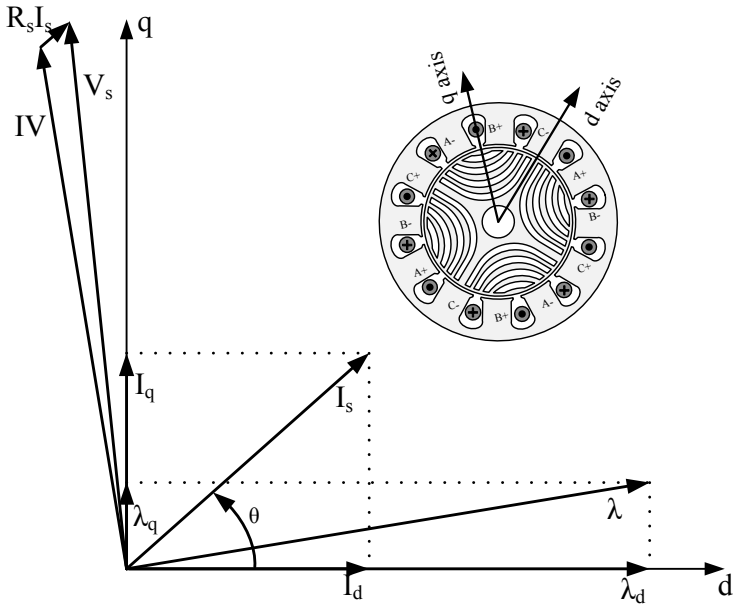

Fig. 1.13 Vector diagram of a SynRM in steady state and a representation of a transversally laminated anisotropic (TLA) rotor SynRM.

1.2.3 SynRM Non-Linearities and Core Losses

The SynRM has several magnetic non-linearities. The most prominent non-linearities are the saturation effects and the cross coupling between the flux of the d-axis and the q-axis. These two non-linearities influence the direct and quadrature inductances that can be written using the following form:

$$\begin{aligned} L_d &= L_d(I_d, I_q) \\ L_q &= L_q(I_d, I_q) \end{aligned} \tag{1.6}$$

1.2.3.1 The Saturation Effect

The non-linear BH curve of the ferromagnetic material used in machine leads to a non-constant inductance in function of the introduced current. This phenomenon is known as the saturation effect in the machine. Mainly, the saturation will lead to the decrease in direct and quadrature inductances when the current increases [32].

Figure 1.14 shows the effect of saturation on the stator flux λ. The d-axis is more involved in the saturation since more flux passes through the ferromagnetic

material. On the other hand, the q-flux is quasi-linear with respect to the evolution of I_q. Furthermore, figure 1.15 shows a comparison of a dq model with nominal L_d and L_q values and FE simulations. This figure shows that at high currents with respect to the nominal current, the saturation impacts the d-axis and the dq-model becomes imprecise with respect to the FE simulations.

The saturation impacts the MTPA phase value (refer to equation (1.2)) since the d-axis saturates more than the q-axis. Thus, when the machine d-axis is partially saturated, increasing I_d doesn't necessarily mean that the produced torque increases. The MTPA phase angle tends to increase to have a slightly larger I_q than the I_d value.

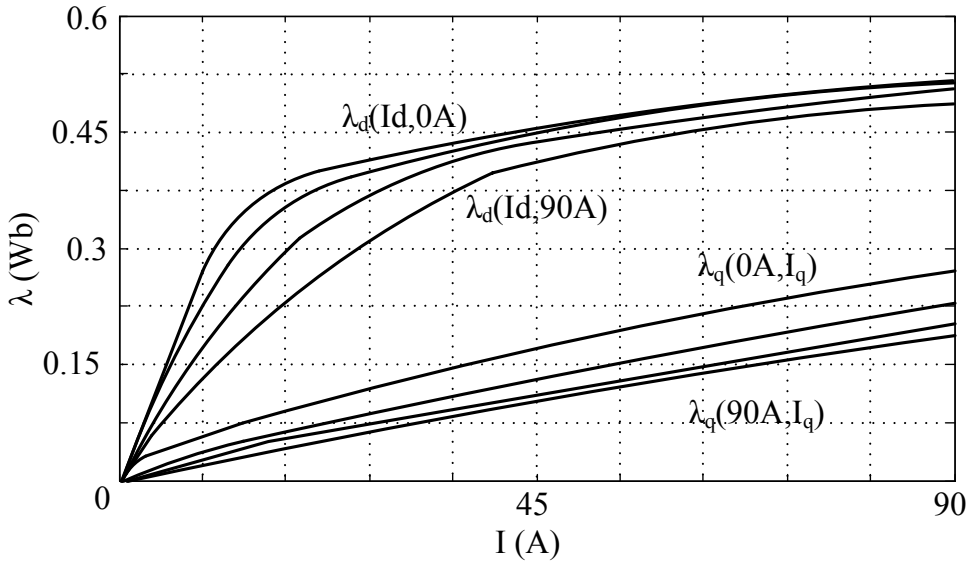

Fig. 1.14 Effect of saturation and cross coupling on the stator flux [30].

1.2.3.2 Cross Coupling Effect

The cross coupling effect are also shown on figure 1.14. The cross coupling is due to the fact that the machine has one core for the d and q axes. Therefore, the passage of a current will not only impact the magnetic properties of the involved axis but the two axes simultaneously. Hence, while increasing the d-current, the q-flux decreases.

1.2.3.3 Core Losses

Due to the absence of excitations in the rotor, the only losses present in the rotor are the core losses. These losses slightly change the operation of the SynRM. In [33], the core losses where represents by a resistance in the SynRM circuit model. Furthermore,

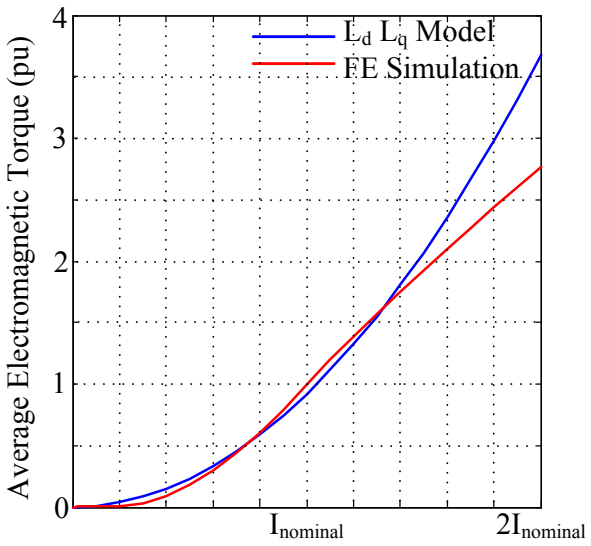

Fig. 1.15 Torque comparison between FE simulations and the dq model with L_d and L_q values at nominal current.

the equivalent vector diagram including core losses is shown on figure 1.16. As shown in the vector diagram, the angle of the phase current I_s increases slightly above θ.

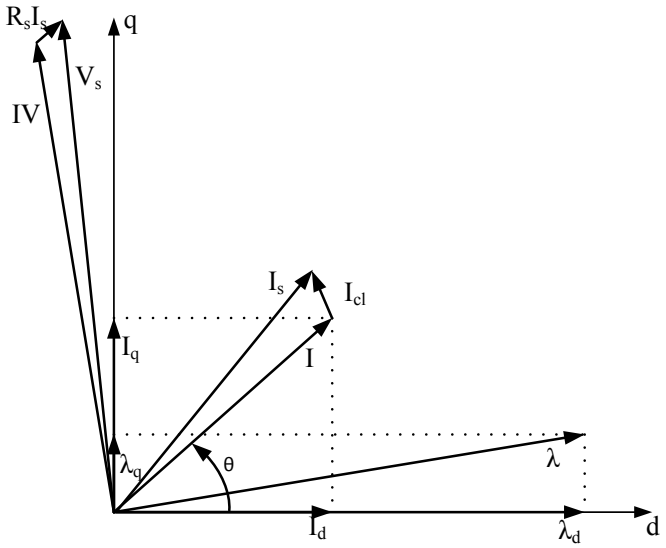

Fig. 1.16 Vector diagram of a SynRM in steady state including core losses.

1.2.4 SynRM Operation Diagram in a Variable Speed Drive

As shown on figure 1.3, machines used in traction systems are required to have a large speed range to insure a wheel speed of 0-130 km/h with a single static gear. However, machines in a battery system connected via power electronics have two main limitations: a current limitation and a voltage limitation. In machine design, the current limitation is mainly due to thermal aspects. A higher current injected in the machine leads to a higher the Joules losses and the winding heat generation. Table 1.6 shows indicative values of the maximal allowed current density in the stator slots for different cooling methods in machines. Therefore, for a specific design and a slot fill factor, a maximal current should not be crossed in order to keep the temperature acceptable and the conductor insulation intact.

Cooling Method	Maximal Current Density (J) (A/mm^2)
Passive Air Cooling	1.5-5
Forced Air Cooling	5-10
Indirect Liquid Cooling (Water Jacket)	7-10
Direct Liquid Cooling (Through Hollow Strands, Immersion Oil Cooling)	10-30

Table 1.6 Maximum current density for different cooling methods in electric machine. [34]

On the other hand, the voltage limitation is due to the battery's DC voltage (V_{DC}). When the machine rotation speed increases, the induced voltage increases. In consequence, the voltage needed across the stator winding increases to maintain the phase currents. Nevertheless, the voltage across is limited and for a 3-phase wye connection as shown on figure 1.17, the limits are the following:

$$max(U_{ab}(t)), max(U_{bc}(t)), max(U_{ca}(t)) < V_{DC} \tag{1.7}$$

where $U_{ij}(t)$ is the instantaneous voltage between phases i and j.

In addition, if the phase voltages are considered symmetrical, balanced and sinusoidal, the voltage limit on the phase-neutral voltage (even if the neutral is a virtual point as is the case of a delta connection) of a given phase is:

$$V_{rms} < \frac{V_{DC}}{\sqrt{6}} \tag{1.8}$$

Finite Elements (FE) simulations are used to determine the maximal performance envelope in the torque speed plane and the corresponding current and phase angle. Representative results are shown on figure 1.18. Similar results were found in [35]. 3 operating speed zones can be differentiated:

- The first operation zone begins from zero speed till the nominal speed. In this zone, the operation limits are defined by the maximal current allowed. Therefore, the torque is constant as well as the phase current angle of about 51 deg (which depends on the saturation state of the machine). This angle is bigger than the theoretical angle of 45 deg found in eqution (1.2) since the core losses and the saturation are taken into account. This current angle is also known as the Maximal Torque Per Ampere (MTPA) angle.

- The second operation zone is when the maximal stator voltage is reached. This occurs starting from the machine nominal speed. Therefore, the field weakening starts by shifting the angle from its MTPA value while keeping the current constant. At the end of this zone, the current angle reaches its Maximal Torque Per Voltage (MTPV) value.

- In the third operation zone, the voltage is not sufficient to maintain the maximal current in the phases. Therefore, the third phase is just voltage limited. The phase currents are decreased to be able to maintain a field weakening operation while keeping the angle to its MTPV value if the performance envelope is respected.

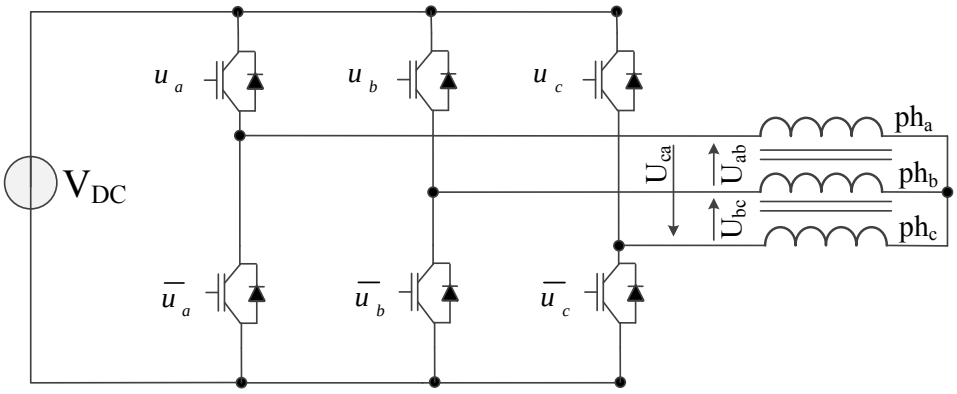

Fig. 1.17 Circuit connection of a 3-phase machine connection.

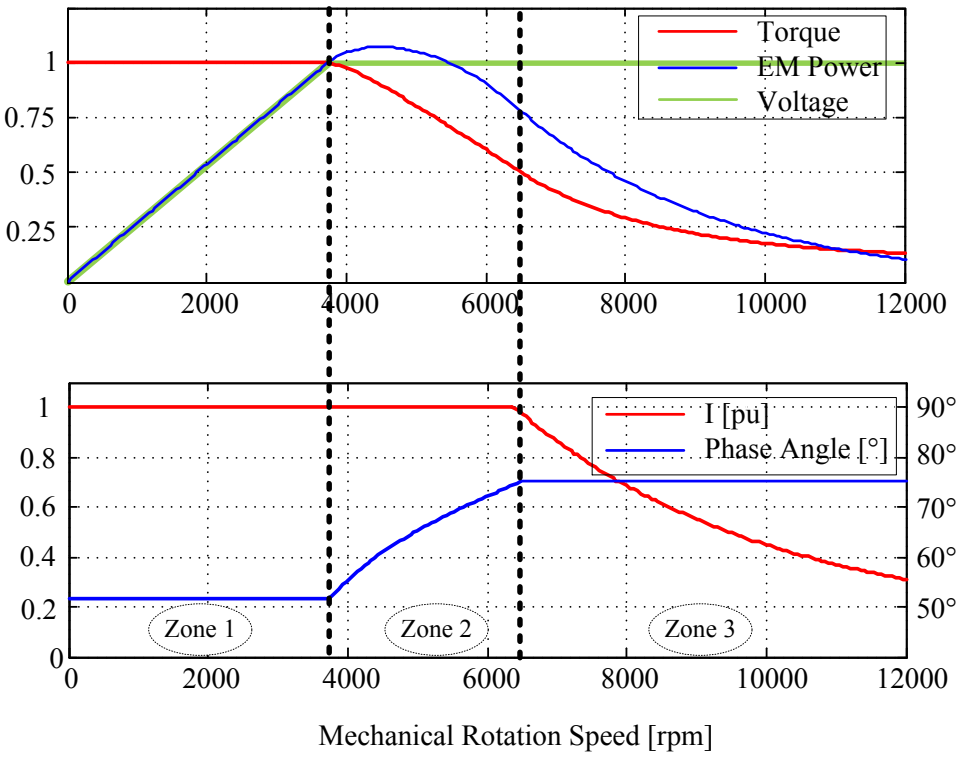

Fig. 1.18 Operation diagram and the performance envelope of a SynRM in pu.

1.3 Conclusion and Scope of the Thesis

Figure 1.19 shows the block representation of a traction system (without the reduction gear) employing a SynRM. A position sensor sends the position of the throttle pedal to a microprocessor where the reference torque is calculated from the measured position. The current reference is imposed as a function of the required torque and is sent the the current controller to generate the PWM signals for the power electronics. The power electronics unit converts the DC battery voltage into AC voltage (frequencies related to the PWM appear in the voltage signal as well). The phase currents of the machine are sinusoidal as well to create a rotating field and to generate motion.

Many obstacles have to be surpassed for the SynRM to be a viable solution for traction applications. Two of these obstacles are the low torque density and the high torque ripple. In this thesis, two study directions are sought in order to enhance the SynRM performance. The first is the machine design in order to maximize the torque density and reduce the torque ripple. While, the second is the SynRM current reference generation from the torque reference. The objectives of the thesis are:

- Developing a design procedure for a SynRM with a high torque per ampere capacity and low torque ripple (chapter 2 and chapter 3).
- Evaluate harmonics injection in the SynRM in the perspective to increase the torque per ampere capacity and to reduce the torque ripple and develop the current control strategy to be able to inject these harmonics (chapter 4).
- Evaluate the design procedure and the current harmonics injection experimentally (chapter 5).
- Adapt the design procedure to an automotive application (chapter 6).

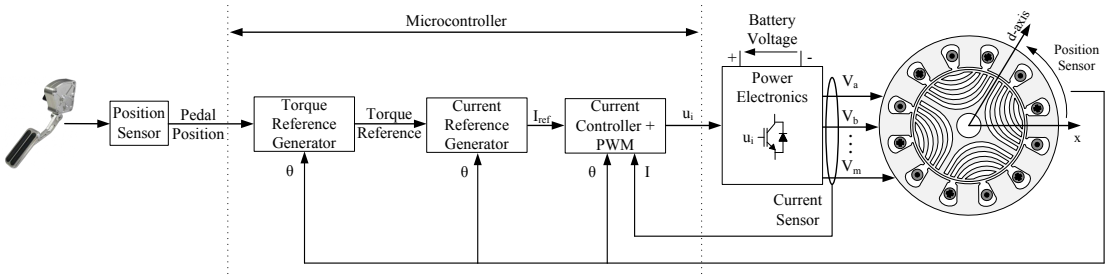

Fig. 1.19 Block representation of the traction system with a SynRM.

Chapter 2

SynRM Rotor Analytical Design

Contents

The SynRM can be traced back to 1923 when Kostko realized an attempt for the first SynRM design [29], after which many studies followed to examine several aspects of the machine.

For instance, from a control point of view, in [36], the basics of the SynRM control and its operation diagram were presented. In [37], a direct torque control was investigated for the SynRM and other control strategies were studied like the field oriented control and other techniques [38–48].

Concerning the SynRM design, the effect of the machine parameters and dimensions on the machine performance such as the torque, the torque ripple and the saliency ratio were studied in [31, 32, 49–55]. Moreover, several rotor designs were introduced like the segmental rotor [56] or the axially laminated anisotropic rotor [57], and several modelling techniques were proposed to understand more the SynRM behaviour [58, 59]. The SynRM field weakening behaviour and the electromagnetic and mechanical performance under high speeds as wwere also treated [23, 35, 60].

The design of the SynRM is a complex task for two main reasons. On one hand, the relatively complex rotor geometry introduces a large number of parameters whose small variations impact significantly the performance of the machine. For instance, the shape of the flux barriers, their number and size must be taken into account [61]. The mechanical bridges and ribs between flux barriers must also be taken into account because their thickness acts directly on the average torque and the saliency ratio [62]. On the other hand, the variation of these different parameters impact several performance criteria simultaneously.

Two of the most prominent performance criteria of the SynRM are the torque per ampere capability and the torque ripple. Several studies in literature have dealt with the minimization of the torque ripple in the SynRM. For instance, in [63–67], the position and the end points of the flux barriers are studied in order to minimize the torque ripple. Conversely, in [68, 69], asymmetrical flux barriers were introduced where significant torque ripple reduction has been documented. In [52], not only asymmetrical flux barriers are introduced, but the skewing impact on the SynRM torque ripple has also been studied. Moreover, in [49], the impact of the slot per pole number and the number of barriers have been studied. Other work studied the SynRM design for a high torque density [50, 70] or for a high saliency ratio [31].

In this study, a novel design procedure of the SynRM's rotor is proposed to achieve a high torque density and a low torque ripple design. The procedure will be divided into two main parts:

- The first part proposes a procedure that determines the flux barriers geometry, position and dimensions. On one hand, the barriers' shape will follow the flux lines in a solid rotor to facilitate the flux passage in the machine's d-axis. On the other hand, the barriers' dimensions will be determined by the flux that passes through to obtain a homogeneous flux distribution. This analytical procedure delivers a SynRM with a high torque density, but does not take into account the torque ripple.

- The second part of the design procedure (presented in the next chapter) proposes a direct finite elements optimization methodology an additional means to reduce the torque ripple of the SynRM.

2.1 Design of the SynRM Rotor: An Overview

2.1.1 Rotor Geometry Classes of the SynRM

Literature presents mainly three types of anisotropic rotor shapes for the SynRM: the simple saliency rotor, the transversally laminated anisotropic (TLA) rotor, and the axially laminated anisotropic (ALA) rotor (refer to figure 2.1). The simple saliency rotor creates a non-uniform airgap in the machine which leads to the pole saliency. Whereas, the TLA and ALA rotor shapes canalize the flux by introducing the flux barriers and the flux segments. The flux barriers are the magnetically isolating material, whereas the flux segments are made up of ferromagnetic steel. The advantage of the simple saliency motor is the fact that it represents a solid block. There is no need for bridges to link the material. Therefore, mechanically wise, it is the sturdiest shape. Moreover, the simple saliency rotor is the simplest to build. However, this shape gives poor electromagnetic performances with respect to the the TLA and ALA machines since no flux canalization exists and more leakage flux is present.

The ALA design uses a screw to hold the flux segments together which are non-laminated massive blocs. However, the TLA design uses bridges and ribs for its mechanical feasibility. The machine stack is made up of laminated steel which leads to a reduction of eddy current effects in the rotor core with respect to the ALA structure. However, the bridges and the ribs act as magnetic short circuit since they let the flux to pass in the q-axis. Therefore, a minor performance advantage in terms of the torque density in an ALA rotor with respect to the TLA rotor can be seen. However, in terms of manufacturing, the ALA rotor requires a more complex process, since a solid non-magnetic material is required to maintain the space constant between the segments.

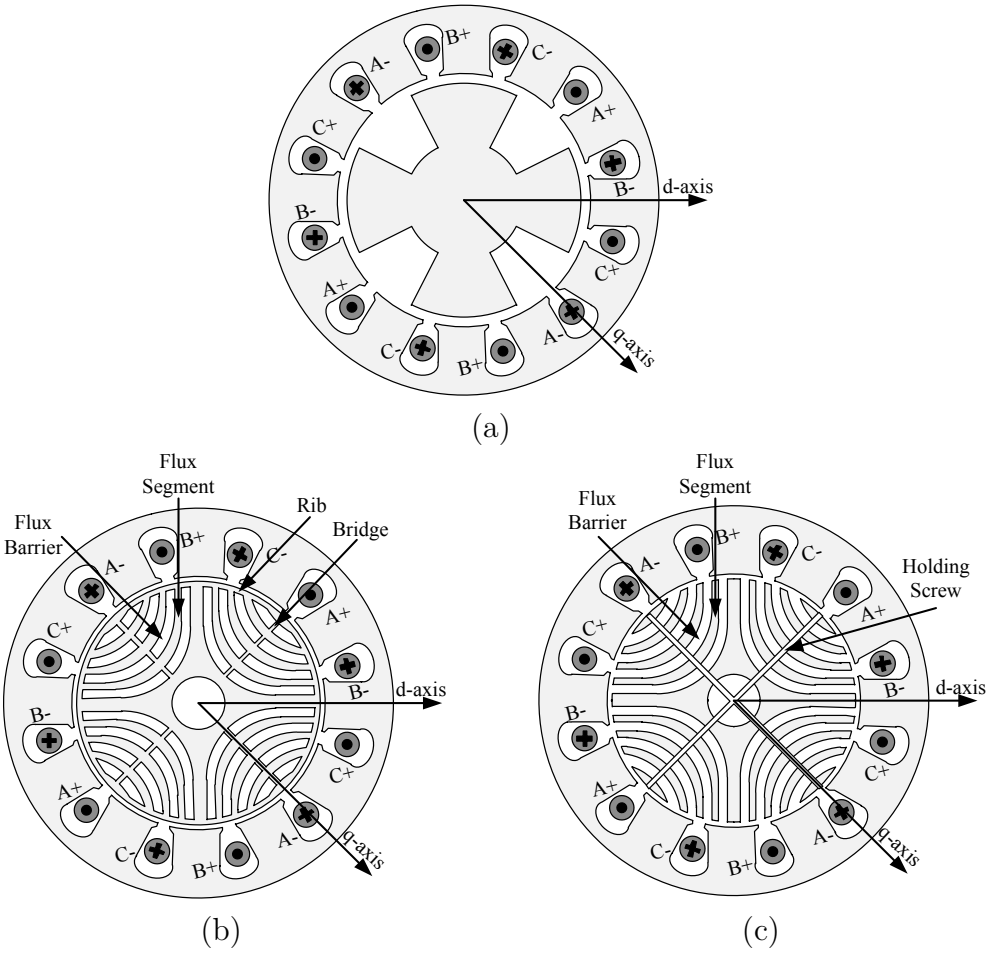

Fig. 2.1 Different rotor designs for a SynRM : (a) simple saliency rotor, (b) transversally laminated anisotropic rotor, (c) axially laminated anisotropic Rotor.

Consequently, the TLA rotor is the most adopted topology in the construction of SynRMs.

2.1.2 Barriers Shape in a TLA Rotor

In the case of a TLA rotor, the flux barriers are made by simply punching holes in the rotor laminations while leaving bridges between the different rotor parts. The barriers are often made of air without adding any additional isolating material. The geometry of the flux barriers is essential for the machine since it is the element that creates the rotor anisotropy. Many shapes have been studied in the literature and corresponding parameters have been defined to determine the machine geometry. A

common geometry can be found in [63, 70] and associates straight lines to define the flux barrier (figure 2.2(a)). Some rounding are added to the edges in some cases in order to make the flux passage in the rotor smoother. Another adopted geometry uses arcs for the barrier definition (figure 2.2(b)) [52, 71].

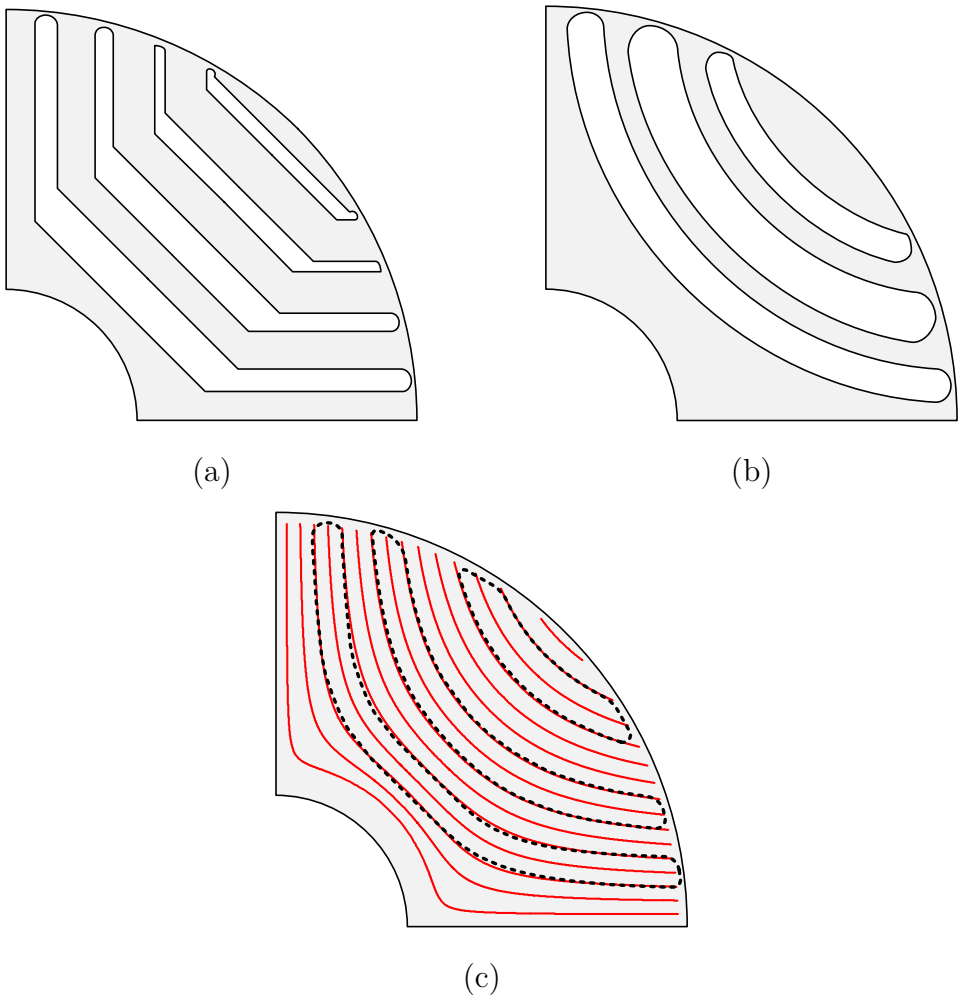

Fig. 2.2 Different rotor designs for a 4-pole TLA SynRM : (a) based on straight lines, (b) based on arcs, and (c) based on the flux lines in a solid rotor.

A more suitable barrier shape can be chosen to follow the flux lines in a solid rotor. This geometry respects the natural flow of the flux lines and has been shown to give competitive results compared with other geometries. However, the flux lines in a solid rotor were rarely put into an equation. It can be noted that in [2], N.E. Joukowski airfoil potential function [72] was used to determine the equation of the flux lines. However, an explicit method based on the electromagnetic equations and

the constitutive principle of the machine materials was never developed and will be developed in the next section.

2.2 Analytical Approach for the Flux Lines in a Solid Rotor

When the flux barriers' contours are placed on the flux lines in this rotor, the smooth passage of the d-flux will be ensured in normal operation when the stator currents are not in phase with the d-axis. The quantity of air in the q-axis should be kept to a maximum to increase the q-axis reluctance as much as possible. However, the increase in air thickness in the q-axis will increase the saturation in the d-axis. Therefore, there is an optimal ratio of air-to-steel thickness.

By definition, the flux lines in an element are the iso-values of the vector potential $\vec{A}$ or the iso-potentials. Putting this vector potential into equation in a solid rotor in a machine while taking into consideration the magnetic non-linearities of the material, the effect of the stator slots, the machine eccentricity and other machine realistic factors, can amount to a complex task from an electromagnetic point of view. In common approaches, some simplifications can be taken into account while maintaining acceptable results. When the analytical equation is determined with the proposed simplifications, a comparison study will be done with the FE simulation to see whether the solution is acceptable. In what follows, two assumptions to simplify the calculation are presented.

2.2.1 Simplified Machine Structure

The two assumptions that are taken in this study are the following:

- The structure is constituted of three concentric cylinders corresponding to the shaft, the rotor and the stator armatures. The length of the machine is great compared to the rotor radius. Consequently, the edge effects are neglected and the field distribution is represented in a two dimensional coordinates system. The vector potential varies only in the (r, θ) plane and its direction follows the z axis. Its expression can be written as follows in the cylindrical coordinates:

$$\vec{A} = A(r, \theta)\vec{e_z} \tag{2.1}$$

- The stator winding is represented by an equivalent current sheet distribution over the stator slot opening. Figure 2.3 shows this substitution by a current sheet where r_{shaft} is the shaft radius, r_{rotor} is the rotor outer radius and r_{stator} is the stator outer radius. The spatial distribution of the conductor density associated to the stator windings is thus reduced to a superficial distribution defined by the following equation in the case of a sinusoidal current:

$$k_{eq} = K_{eq} sin(p\theta) \tag{2.2}$$

where $K_{eq} = \frac{m}{2} I N_s, I$ is the current amplitude, N_s is the total number of conductors per pole and per phase, m is the total phase number, and p is the number of pole pairs of the machine.

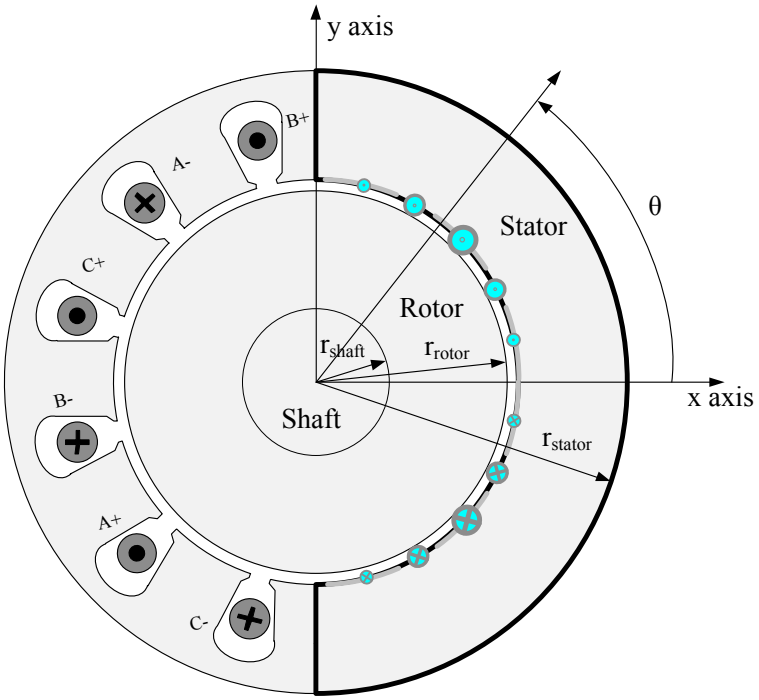

Fig. 2.3 Substitution of the stator excitation by a current sheet.

2.2.2 Vector Potential General Equations

In the approximation of the quasi-stationary states, the modelling of the machine can be made by using Maxwell's equations and the constitutive principle of the materials in the machine. In consequence, the equation to solve can be derived from the potential as follows [73]:

$$\Delta A = 0 \tag{2.3}$$

where Δ represents the Laplacian operator.

A solution for equation (2.3) is:

$$A(r,\theta) = (V_1 r + V_2 r^{-1})(V_3 cosp\theta + V_4 sinp\theta) \tag{2.4}$$

where r represents the distance of a given point from the center of the shaft, θ is the angle of the same point with respect to the x axis, and V_1, V_2, V_3, V_4 are to be determined using the boundary conditions of each sub-domain.

Furthermore, the flux density B and the H field in the structure can be derived from the vector potential:

$$\vec{B} = r\vec{o}t\vec{A} = \begin{vmatrix} B_r = \frac{1}{r}\frac{\partial A}{\partial \theta} \\ \\ B_\theta = -\frac{\partial A}{\partial r} \end{vmatrix} = \begin{vmatrix} \mu_0\mu_r H_r \\ \\ \mu_0\mu_r H_\theta \end{vmatrix} \tag{2.5}$$

where μ_0 is the magnetic permeability of vacuum and μ_r is the relative magnetic permeability of the material with respect to vacuum.

2.2.3 Fields at Interfaces

Two equations dictate the flow of the B and H fields at interfaces. First, the radial component of the flux density crosses unchanged through. This is deduced from Maxwell's equation (2.6).

$$div\vec{B} = 0 \tag{2.6}$$

Secondly, the tangential component of the H field undergoes a discontinuity in the presence of a superficial current distribution. These two phenomena are written as the following:

$$|B_{rDomaine1}|_{r=r_i} = |B_{rDomaine2}|_{r=r_i} \qquad \forall\theta \tag{2.7}$$

$$|H_{\theta Domaine2}|_{r=r_i} - |H_{\theta Domaine1}|_{r=r_i} = kp(\theta) \quad \forall\theta \tag{2.8}$$

where $r_i \in \{r_{shaft}, r_{rotor}, r_{stator}\}$.

Another assumption is carried out at this level in order to reduce the number of equations to solve and to simplify the vector potential calculation. The airgap is considered to impact only the amplitude of the vector potential but not its form. This assumption is considered to be true since the airgap length is constant and negligible with respect the rotor radius. It will be applied since only the flux lines form is sought for in the presented study.

2.2.4 Vector Potential in the Case of a Non-Magnetic Shaft

In the case of a non-magnetic shaft, only two expressions of the potential vector are calculated: the vector in the rotor A_1 and the vector in the stator A_2. Using equations (2.7), (2.8), (2.4) and (2.5) for the three interfaces: shaft-rotor, rotor-stator and stator-exterior, the expression of the vector potential in the rotor is obtained:

$$A_1(r,\theta) = \frac{\mu_0\mu_r m N_s I}{4}\frac{r_{stator}^2 - r_{rotor}^2}{r_{stator}^2 - r_{shaft}^2}(r - \frac{r_{shaft}^2}{r})sinp\theta \qquad r_{shaft} < r < r_{rotor} \tag{2.9}$$

Since the flux lines are found along the iso-potential lines, they are determined by imposing (2.9) equal to a constant. The analytical equation of the flux lines can be written as the following:

$$(r - \frac{r_{shaft}^2}{r})sinp\theta = C \tag{2.10}$$

C is constant for every flux line and it lies in the interval shown in (2.11). When C tends to zero, the described flux line is close to the shaft. Whereas, when the C tends to $(r_{rotor}^2 - r_{shaft}^2)/r_{rotor}$, the described flux lines get closer to the rotor periphery. The values in between these two limits describe all the flux lines in the rotor:

$$0 < C < \frac{r_{rotor}^2 - r_{shaft}^2}{r_{rotor}} \tag{2.11}$$

Figure 2.4 compares the flux lines in a solid rotor between a FE simulation of a machine containing a typical stator and the obtained analytical solution in a four pole machine. The analytical solution is representative of the FE simulation that takes into account the slotting effect and other non-linear aspects. Therefore, the several

considered assumptions are acceptable from what the results have shown. The flux lines are shown for different pole pair number on figure 2.5.

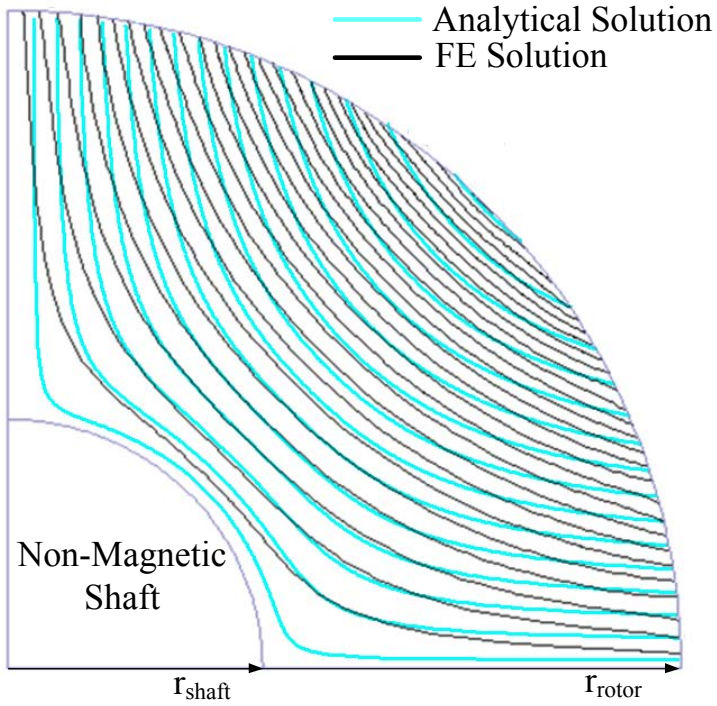

Fig. 2.4 Comparison between the FE simulation and the analytical solutions of the flux lines for a 4 pole SynRM.

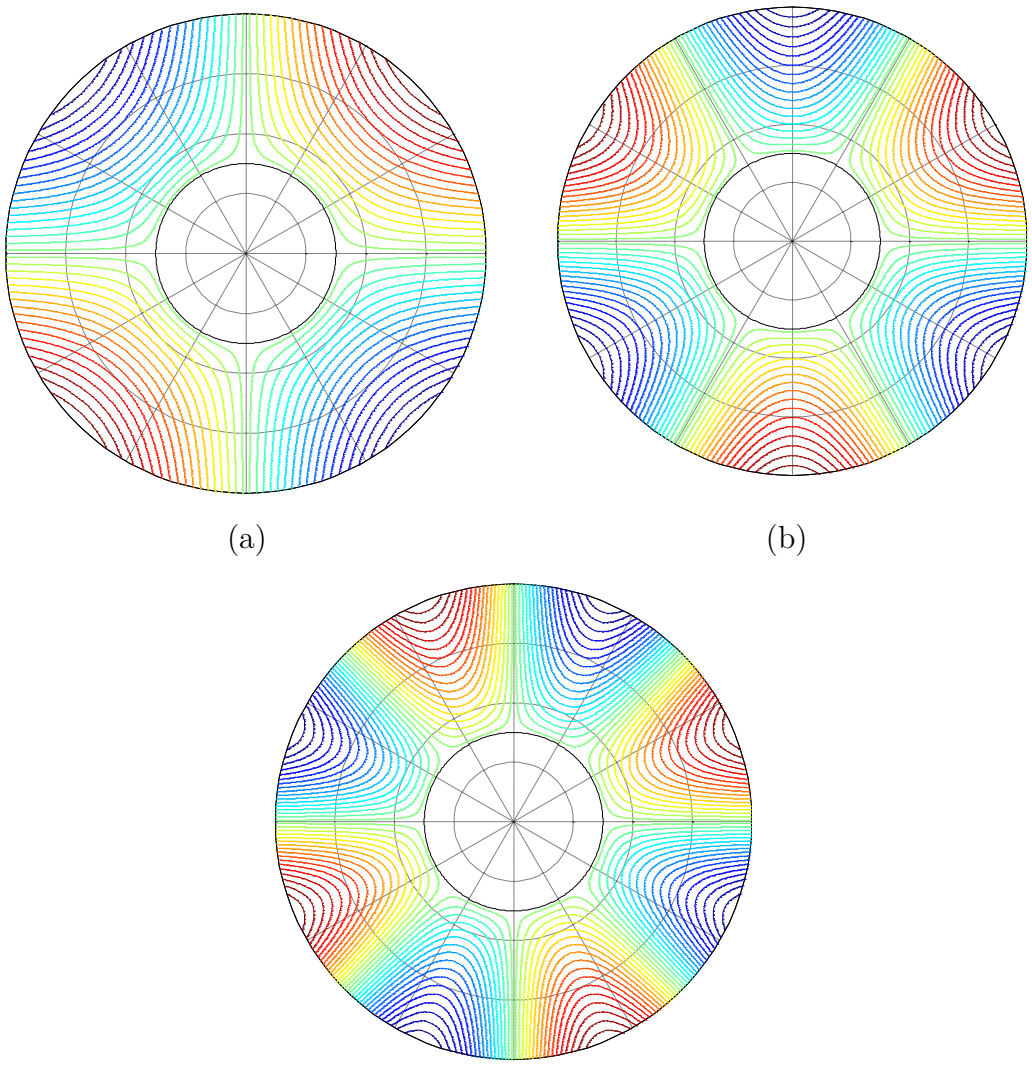

Fig. 2.5 Flux lines in a solid rotor : (a) for p = 2, (b) p = 3, and (c) p = 4.

2.3 Rotor Design Based on the Magnetic Flux Uniformity

In the previous section the shape of the flux barriers following the flux lines in a solid rotor has been put into equation. Now, the flux barriers and flux segments' dimensions (figure 2.6) have to be determined. A novel idea that is based on the uniform distribution of the flux in the rotor is proposed in this section. The idea behind the uniformity of the flux is to not saturate locally the rotor. The local saturation negatively impacts the passage of the flux in the rotor which is penalising for the machine performance. It leads to a reduction in torque and saliency ratio. In order to obtain a uniform distribution of the flux, the flux segments' thickness (L_i on figure 2.6) is proportional to the quantity of flux passing through their respective zones.

The procedure follows these macro steps:

- First, the rotor is divided into N zones, where N represents the desired number of flux barriers.
- Second, the magnetic flux passing through each zone is calculated after the determination of the flux density in a solid rotor.
- Then, the flux segments' dimensions are calculated to be proportional to the quantity of magnetic flux passing through, while imposing an important air-to-steel ratio in the q-axis to ensure a high saliency ratio.

The flux density in a solid rotor can be derived from (2.5), and is shown in equations (2.12) and (2.13) for any point that belongs to the rotor having the polar coordinates (r, θ) in the case of a non-magnetic shaft.

$$\vec{B} = r\vec{o}t\vec{A} = \begin{vmatrix} B_r = pV_1(1 - \frac{r_{shaft}^2}{r^2})cosp\theta \\ \\ B_\theta = V_1(1 + \frac{r_{shaft}^2}{r^2})sinp\theta \end{vmatrix} \tag{2.12}$$

where

$$V_1 = \frac{\mu_0 \mu_r m N_s I}{4} \frac{r_{stator}^2 - r_{rotor}^2}{r_{stator}^2 - r_{shaft}^2} \tag{2.13}$$

The rotor will be then divided into N zones (refer to figure 2.7). In order to determine the quantity of iron in each zone with respect to air, it is assumed that the magnetic field in the zone passes only through the iron. Furthermore, the quantity of iron is determined to be proportional to the magnetic flux passing through. For that,

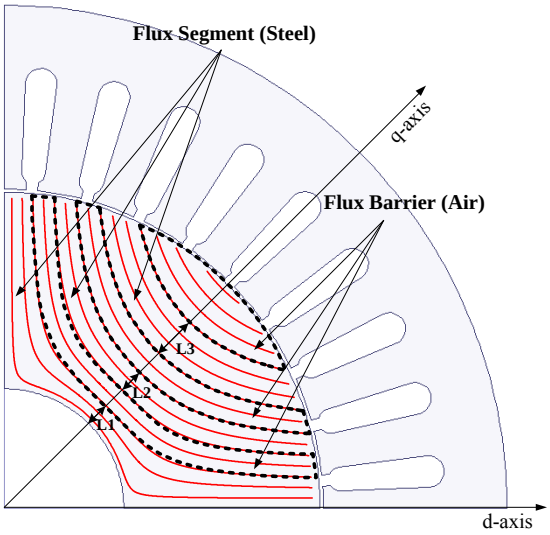

Fig. 2.6 Positioning of the flux barriers and the flux segments inside the rotor.

the flux passing perpendicular to the axis of $\theta = \frac{\pi}{2p}$ is considered. Since, at this axis, the peripheral rotor effects are negligible. The equation of the flux density on this axis is shown in equation (2.14). The flux density is drawn along the axis of $\theta = \frac{\pi}{2p}$of the rotor on figure 2.8.

$$\vec{B} = \begin{vmatrix} B_r = 0 \\ B_\theta = V_1(1 + \frac{r_{shaft}^2}{r^2}) \end{vmatrix} \tag{2.14}$$

Since the machine has a constant active length, the proportionality of the flux in each zone along the q-axis can be written as the following:

$$\frac{L_i}{L_j} = \frac{\int\limits_{Zone_i} B_\theta(r)dr}{\int\limits_{Zone_j} B_\theta(r)dr} \tag{2.15}$$

where $(i, j) \subset \{1, 2, ..., N\}^2$ and L_i is the width of the i^{th} flux segment.

An important anisotropy is required to increase the saliency ratio. Therefore, the flux passage should be limited through the q-axis. This lead to a reduction of iron in the q-axis [31, 32, 38]. Hence, an insulation ratio K_{wq} can be defined as the ratio of air to rotor width (the difference between the exterior and the interior radii of the rotor) and is shown in (2.16). The quantity of iron is shown in (2.17).

$$K_{wq} = 1 - \frac{\sum_{i=1}^{N} L_i}{r_{rotor} - r_{shaft}} \tag{2.16}$$

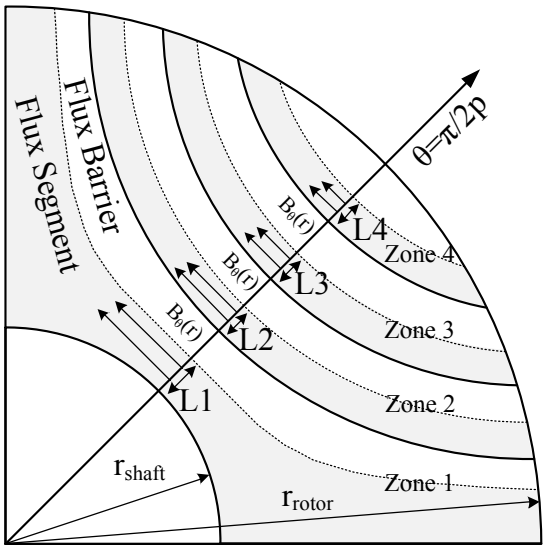

Fig. 2.7 Flux zones in the rotor and the representqtion of the flux density passing perpendicular to the $\theta = \frac{\pi}{2p}$ axis.

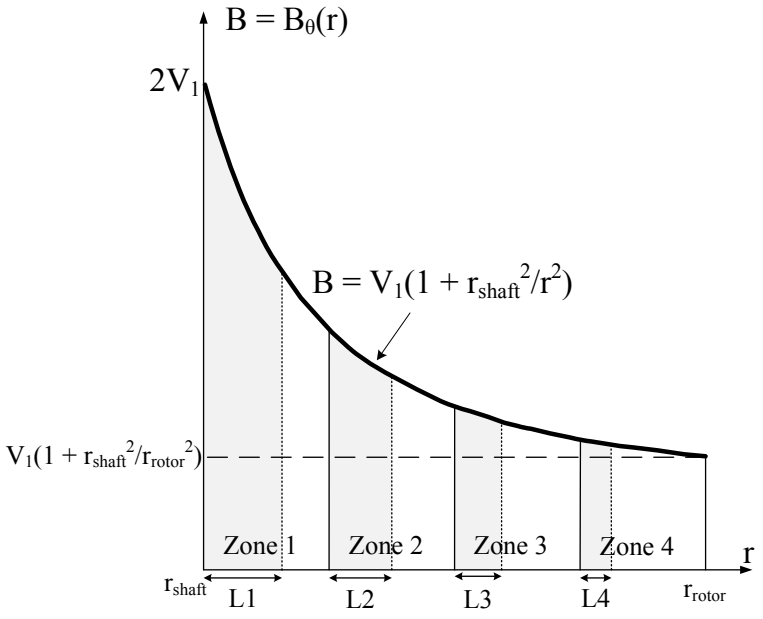

Fig. 2.8 Field density passing through the flux zones at $\theta = \frac{\pi}{2p}$.

$$\sum_{i=1}^{N} L_i = (r_{rotor} - r_{shaft})(1 - K_{wq}) \tag{2.17}$$

By defining K_{wq}, (2.15) and (2.17) can be solved in order to determine the width of the iron part in each zone. This ratio was studied in [53, 70] and the optimal value is found to be around 0.5 in both studies. In other terms, around half of the rotor in the q-axis is made up of iron and the other half of air. The width of a flux barrier(W_i) adjacent to a flux segment of width L_i can be determined using the equation (2.18).

$$W_i = \frac{K_{wq}}{1 - K_{wq}} L_i \tag{2.18}$$

Figure 2.9 shows the flux density distribution in the rotor from the proposed design procedure. Bridges and ribs are added to insure mechanical strength. Concerning flux densities, the zones with highest values are the ribs and the bridges. Flux density values around $2T$ are found in these elements. The resulting saturation of the ribs and bridges is desirable since they act as a magnetic short-circuit and increase L_q. On the other hand, the flux density values is the main rotor structure are quasi-uniform except a low flux density in the last flux segment on the periphery of the rotor. The presence of this segment is important since, as will be shown in section 2.4.2, it greatly reduces the torque ripple. Furthermore, another low flux density is reported around the shaft. For an electromechanical point of view, this part does not have a major influence. Therefore, iron can be removed in order to decrease the weight of the machine and increase its power density.

The design based on flux lines in a solid rotor is compared with a rotor design based on arc barriers (figure 2.10). The two designs contain 4 flux barriers and the same stator. The same ribs and bridges are used for both designs to compare correctly the electromagnetic performance. Table 2.1 presents the FE simulations performance comparison of the two designs. It shows that the design based on the flux lines in a solid rotor gives better results in all criteria except the phase induced voltage where it delivers 1.8% more voltage. The saliency ratio increases by 9.5% and that by mainly decreasing L_q (-9.1%). Moreover, the average torque increases as well by 5%. The torque ripple is high in both cases for the reason that a low stator slot number is taken (16 slots stator).

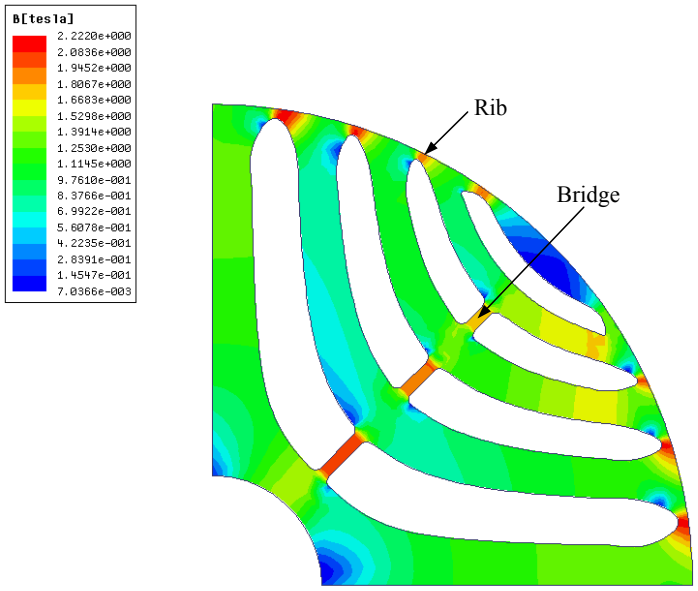

Fig. 2.9 Flux density distribution in the rotor in a design based on the proposed procedure.

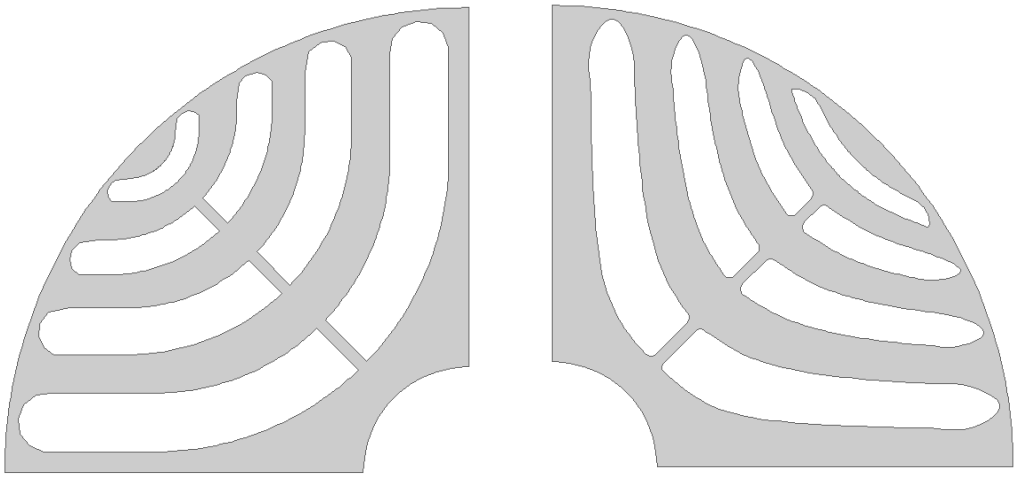

(a) (b)

Fig. 2.10 Two designs used for comparison, (a) arc flux barriers and (b) flux barriers based on flux lines in a solid rotor.

	Arc Barriers Design	Flux Lines Design	Difference
Current Amplitude I (A)	10	10	–
Current Angle θ (°)	51	51	–
Rotation Speed (rpm)	500	500	–
Induced Voltage (V_{rms})	15.7	16	+1.8%
L_d (mH)	38.4	38.7	+0.7%
L_q (mH)	14.3	13.2	−9.1%
Saliency Ratio (−)	2.69	2.94	+9.5%
Average Torque (Nm)	2.1	2.21	+5%
Torque Ripple (−)	30.5%	28%	−8%
Power Factor at MTPA (−)	0.52	0.54	+3.9%

Table 2.1 Comparison between two SynRM rotor designs: the design based on arc flux barriers and the design based on the flux lines in a solid rotor.

2.4 Proposed Design Procedure in a Practical Case

The proposed design procedure will be applied to a machine with the following specifications:

- Rated nominal electromagnetic torque = 2.2 Nm
- Rated nominal speed = 3500 rpm
- Maximum speed = 7000 rpm
- No-load maximum speed (for mechanical strength) = 10500 rpm
- Battery voltage = 200 Vdc

Table 2.2 shows the fixed parameters for the design procedure to take into account. The stator design is fixed. A 2-phase SynRM will be used for harmonics injection reasons presented in the chapter 4. Concerning the current excitation density, the maximal accepted value is $5A/mm^2$ to avoid forced air or liquid cooling (refer to section 1.2.4). The slot filling ratio is 0.5 which represents the ratio of the copper section to the total slot section. The airpap value is fixed to a minimum value of $0.5mm$

taking into consideration the mechanical constraints (manufacturing constraints and the expansion due to centrifugal forces). As a result, the rotor external diameter is fixed at $D_{rotor} = D_{airgap} - 2g = 79mm$. Furthermore, the shaft diameter is imposed by the mechanical requirements. The shaft should be rigid enough to endure the electromagnetic torque and has to overcome the vibration due to high speeds, the bending torque, torsion and the corresponding applied stresses. In addition, the rigidity of the shaft impacts the machine eccentricity at high speeds. All these mechanical constraints are accounted for and impose a minimal value of shaft diameter of $18mm$ considering a mechanical strength security margin as well. Concerning the flux barriers number, it has been shown in [31] that a number 4 of barriers or above is acceptable for the SynRM. However, the machine performance stays constant with a barrier number higher than 5. Therefore, a 4-barriers rotor will be chosen for the study. On the other hand, a pole pair number ($p = 2$) is common in SynRMs [27, 69, 74, 75]. In addition, the slot number ($N_{slot} = 16$) is fixed by the stator geometry as well as the phase number ($m = 2$). Therefore, a full-pitch winding is possible if $p = 2$. The resulting winding configuration will be of one layer and 2 slots/pole/phase. The stator geometry and the winding configuration are shown on figure 2.11.

Parameter	Symbol	Value	Unit
Stator External Diameter	D_{stator}	123	mm
Stator Internal Diameter	D_{airgap}	80	mm
Active Length	L_a	100	mm
Phase Number	m	2	–
Slot Number	N_{slot}	16	–
Slot Section	S_{slot}	140	mm^2
Current Excitation Density	J_s	5	A/mm^2
Slot Filling Ratio	K_{fill}	0.5	–
Airgap Length	g	0.5	mm
Shaft Diameter	D_{shaft}	18	mm
Flux Barriers Number	$N_{barriers}$	4	–
Pole Pairs Number	p	2	–

Table 2.2 Fixed parameters for the design procedure of the SynRM.

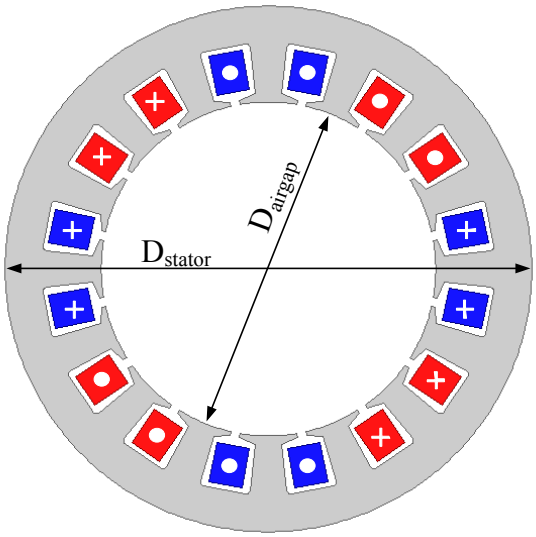

Fig. 2.11 Stator geometry and winding configuration of the SynRM used for the machine design.

2.4.1 K_{wq} Sensitivity Study

A sensitivity analysis is performed on the SynRM performance when the insulation ratio (K_{wq}) varies and is shown on figure 2.12. In order to simplify the study, the ribs and the bridges are kept with constant dimensions even if the mechanical stress vary with the variation of K_{wq}. Figure 2.12 shows that a K_{wq} value between 0.5 and 0.6 is optimal for both the average torque value and the torque ripple value. However, they are not achieved at the exact same value of K_{wq}.

2.4.2 Cut-Off

The presence of the cut-off in the SynRM TLA rotor means the absence of the rotor last flux segment towards the rotor periphery (refer to figure 2.13). The last segment's weight is around 4% of the total rotor weight. Therefore, its presence affects the specific power and the torque density of the machine. The cut-off's impact on the machine performance is necessary to evaluate a competitive design. Table 2.3 shows the electromagnetic performance comparison of the rotor with cut-off with the rotor without cut-off using FE simulations. On all shown performances, the two designs are similar except on the torque ripple level. The torque ripple in the case of a rotor without cut-off is 42% less than the case of the presence of the cut-off. The torque

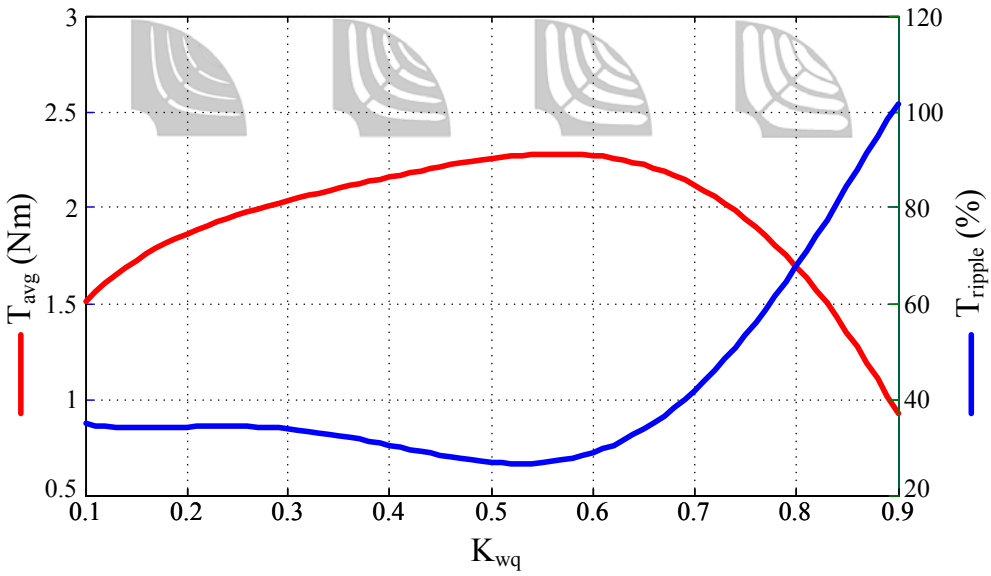

Fig. 2.12 Sensitivity study on K_{wq} using FE simulations.

ripple is an important criteria in most applications and in particular the automotive traction application.

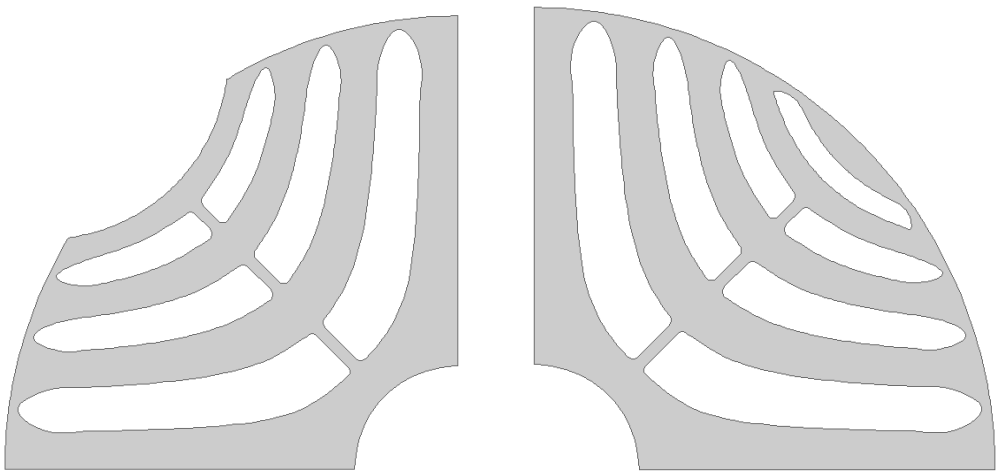

(a) (b)

Fig. 2.13 Cut-off comparison: (a) rotor with cut-off and (b) rotor without cut-off.

	Rotor with Cut-Off	Rotor without Cut-Off	Difference
Current Amplitude I (A)	10	10	–
Current Angle θ (°)	51	51	–
Rotation Speed (rpm)	500	500	–
Induced Voltage (V_{rms})	16.1	16	−0.4%
L_d (mH)	37.73	38.7	+2.7%
L_q (mH)	12.9	13.2	+1.7%
Saliency Ratio (−)	2.91	2.94	+1%
Average Torque (Nm)	2.23	2.21	−0.1%
Torque Ripple (−)	48%	28%	−42.3%
Power Factor at MTPA (−)	0.54	0.54	+0%

Table 2.3 Performance Comparison between two Designs: Rotor without Cut-Off and Rotor with Cut-Off.

2.4.3 Ribs and Bridges

The ribs and the bridges (figure 2.14) are the only elements that hold the different flux segments together in a TLA rotor. Therefore, their dimensions are important to have a mechanically strong rotor. However, from an electromagnetic point of view, they act as a magnetic short circuit. Hence, they increase the leakage inductance, and most importantly the quadrature inductance. In this regard, their dimension should be a small as possible but big enough to keep the structure mechanically strong. It can be also noted that, at a nominal operation point, the ribs and the bridges are saturated. Thus, their relative permeability decreases leading to better electromagnetic performance. Figure 2.9 shows the saturation of the ribs and bridges.

The work presented in literature treats one element at a time. For instance, in [50], the authors studied the effect of the ribs and showed that the torque difference is proportional to the rib width. Similar results were presented in [32], but this time on the bridges. In addition, the simultaneous effects of the ribs and the bridges were never treated in literature.

On figure 2.15, the effect of the rib width on the machine torque, torque ripple and machine saliency ratio is plotted. It can be noted that the saliency ratio, the torque produced by the machine and the torque ripple decrease with the increase of

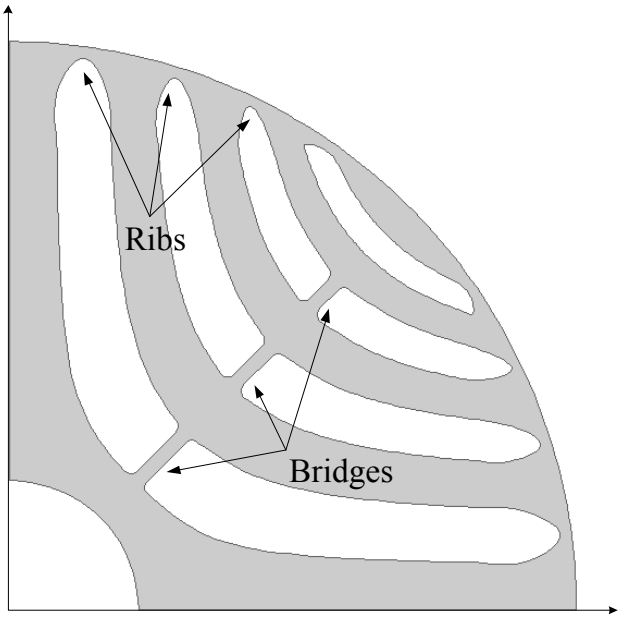

Fig. 2.14 Ribs and bridges in a SynRM.

the ribs width. When the ribs' width increases, the equivalent air gap of the machine is smoother. Even if the torque ripple decreases which is beneficial to the machine performance, the torque and the saliency ratio decrease dramatically, deteriorating the machine performance.

On figure 2.16, the effect of the bridge width is studied at a constant rib width. The torque and the saliency ratio have the same tendency as in the case of the ribs varying. However, the torque ripple could increase or decrease without a uniform tendency.

If the ribs and the bridges are considered simultaneously, it can be noted that the ribs impact on the saliency ratio and the torque value is more intense than the bridge width effect. For example, an increase of 20% of the rib width leads to a decrease of 20% of the torque. However, a same decrease of 20% of the bridge width accounts for the decrease of only 5% of the torque. Therefore, when the mechanical constraints are considered, it would be preferred to put more importance on decreasing the dimensions of the ribs than decreasing the bridge width.

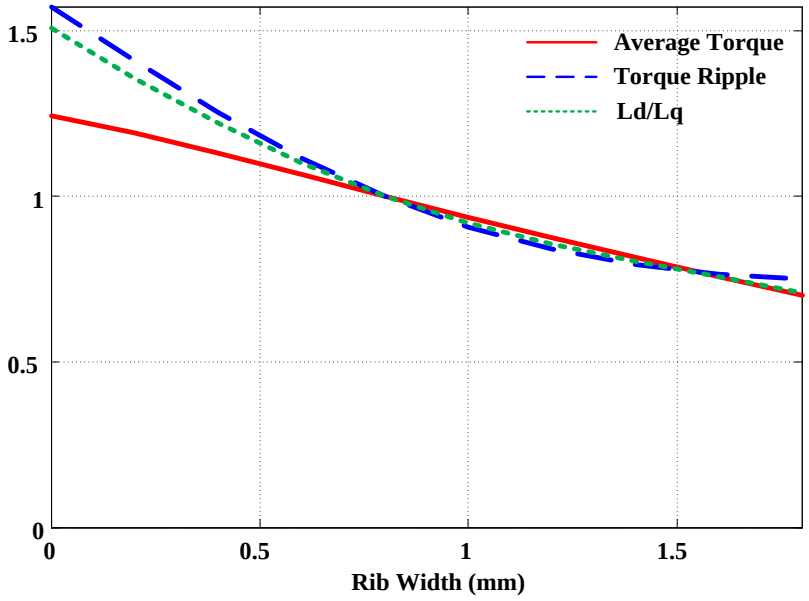

Fig. 2.15 Average torque, torque ripple and saliency ratio of a SynRM in p.u. as a function of the rib width at a constant bridge width of 1mm.

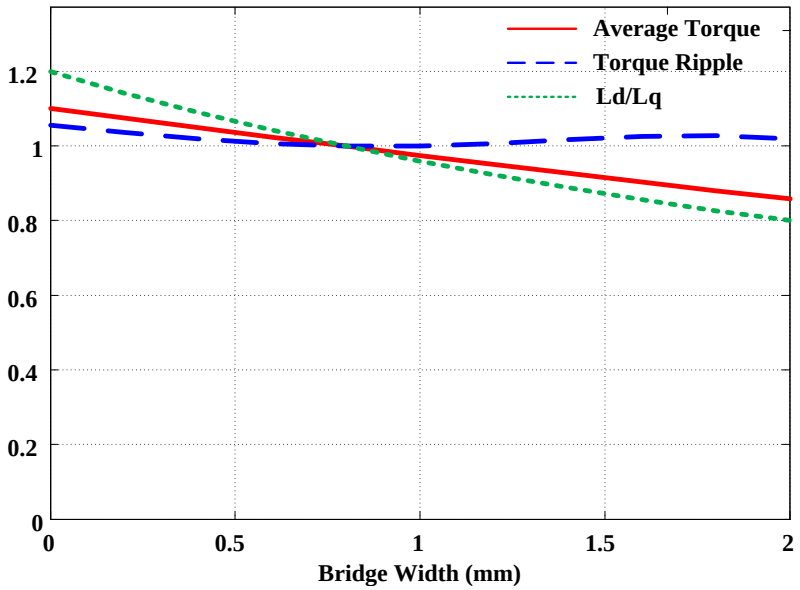

Fig. 2.16 Average torque, torque ripple and saliency ratio of a SynRM in p.u. as a function of the bridge width at a constant rib width of 0.8 mm.

2.4.4 Final Design and Mechanical Performance Analysis

The chosen parameters for the machine design are shown in table 2.4 and the corresponding machine cross section on figure 2.17. In order to verify that the design is mechanically viable, an element Von Mises stress test is performed and shown on figure 2.18. The steel used for the study is $M400-35A$ for which the elastic limit is 385 MPa and the Young's modulus is of 225000 MPa. The maximal reported stress at 10500 rpm is around 100 MPa which is largely underneath the elastic limit of the machine and is considered safe at the maximal speed. Moreover, the maximal deformation of the rotor for the 10500 rpm is 7.77 μm or 1.5 % of the airgap length.

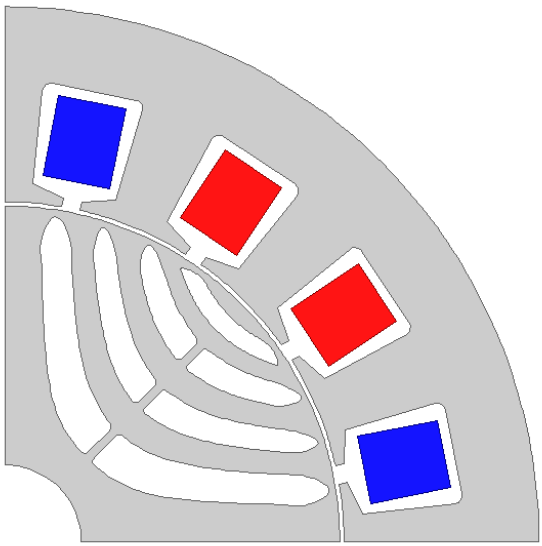

Fig. 2.17 Cross section of the SynRM based on the proposed analytical design procedure with the design parameters shown in table 2.4.

Parameter	Symbol	Value	Unit
Stator External Diameter	D_{stator}	123	mm
Stator Internal Diameter	D_{airgap}	80	mm
Active Length	L_a	100	mm
Phase Number	m	2	–
Slot Number	N_{slot}	16	–
Slot Section	S_{slot}	140	mm^2
Airgap Length	g	0.5	mm
Shaft Diameter	D_{shaft}	18	mm
Rotor Diameter	D_{rotor}	79	mm
Bridges Width	$W_{bridges}$	1	mm
Ribs Width	W_{ribs}	0.8	mm
Flux Barriers Number	$N_{barriers}$	4	–
Pole Pairs Number	p	2	–
q-axis Insulation Ratio	K_{wq}	0.52	–

Table 2.4 Final design parameters.

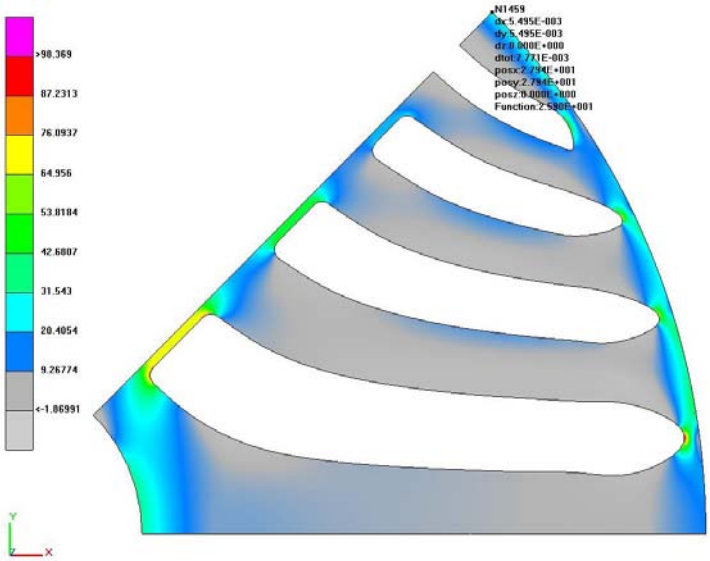

Fig. 2.18 Rotor stress (Von Mises stress) and mechanical deformation for the proposed design at 10500 rpm.

2.4.5 Electromagnetic Performance of the Proposed SynRM Design

The performance of the machine at nominal speed is found in table 2.5, and on the torque-speed envelope on figure 2.19 obtained from FE simulations using Maxwell 2D and Matlab for $V_{DC} = 200\ V$. The specifications imposed for the machine are met. Two main undesirable values can be seen in the machine performance: the power factor of 0.54 and the torque ripple of 28%. The power factor can be enhanced by reducing the ribs and bridges dimensions, by optimizing the stator geometry or by introducing ferrite permanent magnets in the flux barriers [76–78]. Moreover, the torque ripple can be decreased by displacing the flux barriers since they are the result of the interaction of the stator slots and the flux barriers. However, a model of these interaction cannot be easily obtained. The next chapter will present an optimization method that alters the position of the barriers to decrease the torque ripple without impacting neither the saliency ratio nor the torque density of the machine.

	Symbol	Value	Unit
Current Amplitude	I	10	A
Current Angle	ϕ	51	$^\circ$
Rotation Speed	Ω_{mec}	3500	rpm
Induced Voltage	IV	112	V_{rms}
Direct Inductance	L_d	38.7	mH
Quadrature Inductance	L_q	13.2	mH
Saliency Ratio	ξ	2.94	–
Average Torque	T_{avg}	2.21	Nm
Torque Ripple	T_{ripple}	28%	–
Power Factor	PF	0.54	–
Efficiency	η	93	%

Table 2.5 Performance of the proposed design at nominal operation point obtained from FE simulations.

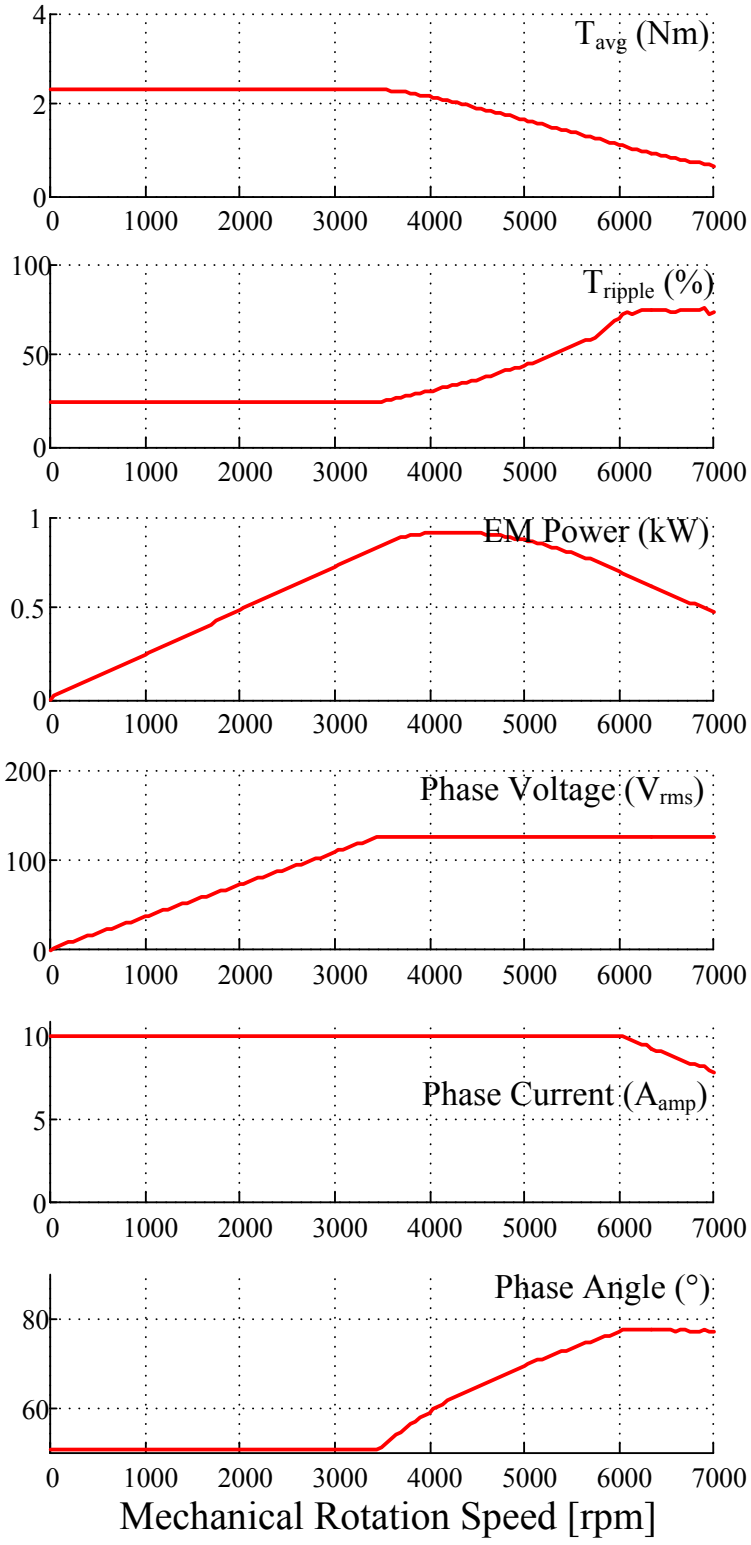

Fig. 2.19 Performance at torque-speed envelope and the current values of the proposed design obtained from FE simulations for $V_{DC} = 200\ V$.

Chapter Conclusion

This chapter presents an analytical design procedure of the SynRM rotor. This design procedure is based on the flux lines and the uniformity of the flux in a solid rotor and showed better results in comparison with the rotor with arc flux barriers. The proposed design procedure is applied in a concrete case where the ribs and the bridges' dimensions, the presence of the cut-off and K_{wq} are studied. A mechanical study is shown at the end to verify that the rotor is strong to undergo 10500 rpm and the electromagnetic performance is shown on the machine torque-speed envelope.

Chapter 3

Parametric Optimization for the SynRM Rotor Design

Contents

This chapter presents a supplementary design level to the analytical design procedure proposed in the last chapter. It is based on the direct finite elements optimization on the machine. The main goal of this method is to reduce the torque ripple without reducing the torque density or the saliency ratio of the SynRM.

3.1 Performance Indicators

The torque capability of the machine is an important factor to determine its competitiveness [54, 79]. A common way to evaluate the machine torque capability is by evaluating the difference between the direct and quadrature inductances ($L_d - L_q$) [31, 50, 53]. Nevertheless, the torque capability can be measured by several means: torque per ampere unit, torque per mass unit or torque per volume unit [54]. In the current problem, since neither the stator diameter nor the machine active length (L_a) change, the machine volume is constant. Therefore, the torque per ampere unit is directly proportional to the torque per volume unit and will be chosen as the first Performance Indicator (PI).

The saliency ratio (L_d/L_q) (see equation 1.4) directly influences the power factor of the machine (see equation 1.5). It has been shown in [38] that the field weakening capabilities of the SynRM increase with the increase of the machine saliency ratio. Consequently, the saliency ratio is an important performance indicator that has to be taken into account.

The machine torque ripple is an important issue for the machine since the interaction between the flux barriers and the stator slots develop a high torque ripple [49, 68, 71]. Several work have evaluated designs for torque ripple minimization [63, 66, 80].

The three chosen performance indicators are the following:

- PI_1 : Torque mean value per ampere
- PI_2 : Torque ripple rate
- PI_3 : Saliency ratio (L_d/L_q)

3.2 Optimization Variables

A set of parameters have to vary the geometry of the rotor in the parametric optimization proposed in this chapter. In addition, these following elements should either be identified by fixed parameters or by the optimization parameters:

- Flux barriers (shape, position, width and number)

- Ribs and bridges
- Pole pair number
- Shaft diameter
- Rotor diameter
- Cut-off

For the number of flux barriers, the pole pairs number, the shaft diameter and the rotor diameter, no changes occurs with the initial design method and the values from table 2.2 are maintained. The absence of the cut-off was proven to be crucial for lower torque ripple in section 2.4.2. Hence, the last flux segment in the rotor will be added and the rotor will be without a cut-off. The ribs and the bridges are determined by a compromise between two considerations: the mechanical strength and the electromagnetic performance. Section 2.4.3 shows the effect of these elements on the SynRM electromagnetic performance. When the rotor geometry changes, the mechanical constraints in the machine change as well. A solution can be to adapt the ribs and bridges dimensions to achieve optimal performance. However, given the complexity this adaptation adds to the optimization algorithms (since mechanical simulations or mechanical models should be used), the variation of their dimensions will not be added within the rotor optimization. Their form are determined *a priori* to ensure the mechanical stability for a maximal rotation speed of $12000rpm$ for the initial design. At the end, of the optimization, a mechanical study will ensure that the rotor structure is still mechanically strong. The values of the fixed rotor parameters are shown in table 3.1.

Parameter	Symbol	Value	Unit
Rotor Diameter	D_{rotor}	79	mm
Air Gap Length	e	0.5	mm
Active Length	L_a	100	mm
Shaft Diameter	D_{shaft}	18	mm
Pole Pairs	p	2	–
Flux Barrier Number	$N_{barriers}$	4	–
Bridges Width	$W_{bridges}$	1	mm
Ribs Width	W_{ribs}	0.8	mm

Table 3.1 Fixed rotor design parameters of the SynRM used in the optimization.

The flux barriers following the flux lines pattern (equation (2.10)) in a solid rotor this pattern is used to draw the flux barriers. This automates the drawing of the flux barriers. Moreover, two main criteria influence the torque and the torque ripple in the SynRM rotor when the flux barriers' shape is imposed:

- Insulation ratio K_{wq}
- Flux barriers endpoints position

Several set of optimization variables can be chosen for the optimization study keeping in mind that they should be kept to a minimum since the optimization algorithm time increases exponentially with the number of variables used. The intersection points (Y_i) between the sides of the barriers and the $\theta = \pi/2p$ axis are chosen as the optimization variables (refer to figure 3.1). This leads to 2 variables per flux barrier. When Y_i is chosen during an optimization algorithm process, a corresponding constant C_i is found from equation (3.1) which is derived from equation (2.10) for $\theta = \pi/2p$. Figure 3.2 shows how the flux barrier side is drawn using equation (2.10).

$$C_i = (Y_i - \frac{r_{shaft}^2}{Y_i}) \tag{3.1}$$

The advantage of this approach is that only two variables are used to define a flux barrier unlike in [81] where 3 variables are used for defining a flux barrier. The decrease of the number of variables will exponentially decrease the computing time of the optimization. Moreover, adapting the variables Y_i, the insulation ratio K_{wq} will be automatically adapted and the barriers' endpoints will change position.

Some geometrical constraints have to be applied to respect the manufacturing constraints of the machine. These constraints on the rotor variables are shown in the following equation:

$$\begin{aligned} &Y_1 > R_{shaft} + \varepsilon, \\ &Y_j > Y_i + \varepsilon, \\ &\quad \forall i = j - 1 \quad \& \quad j \in \{2, 3, \ldots, 8\}, \\ &Y_8 < R_{rotor} - \varepsilon. \end{aligned} \tag{3.2}$$

where ε is the minimal limit of the width of the flux barriers and the flux segments. This limit is determined by the manufacturing precision, and by the deterioration of the magnetic material due to the manufacturing of the rotor. $\varepsilon = 1mm$ in the present case.

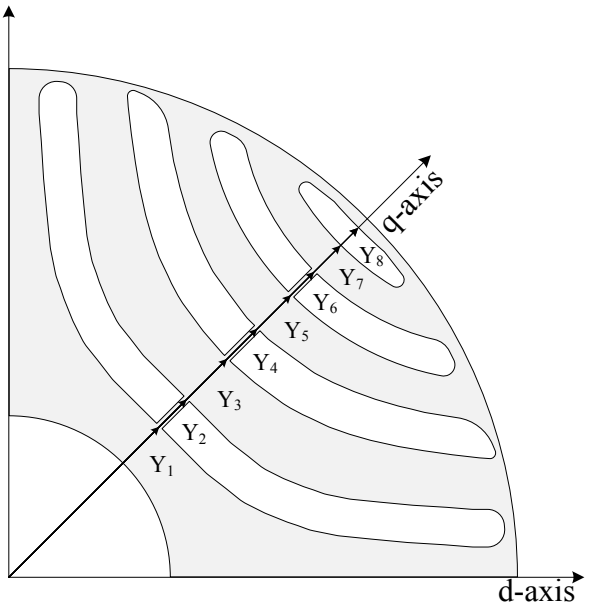

Fig. 3.1 Rotor optimization variables that define the geometry of the rotor.

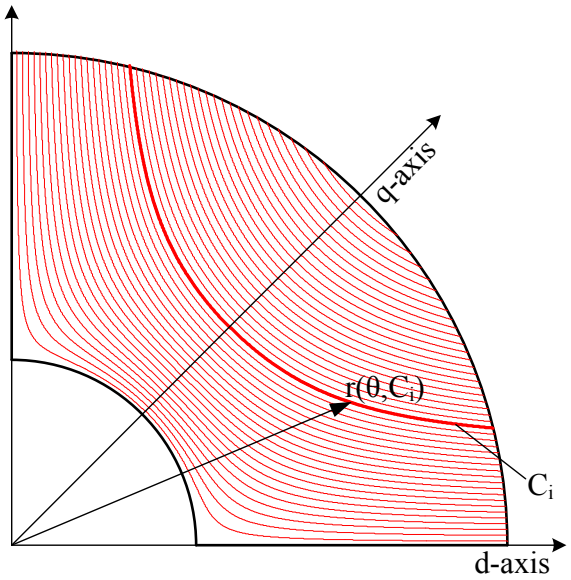

Fig. 3.2 Flux line i is drawn when C_i is determined.

3.3 Optimization Methodology

An optimization algorithm is associated with a FE simulations software in order to find optimal solutions for the machine design. In a general manner, optimization algorithms work as shown on figure 3.3. The iterative nature of the optimization problem linked to the important time of execution of a single FE iteration can be considered as a disadvantage for the presented method. However, the accurate results this method ensures, outweigh this disadvantage. Furthermore, a refined design is essential for high performance machines.

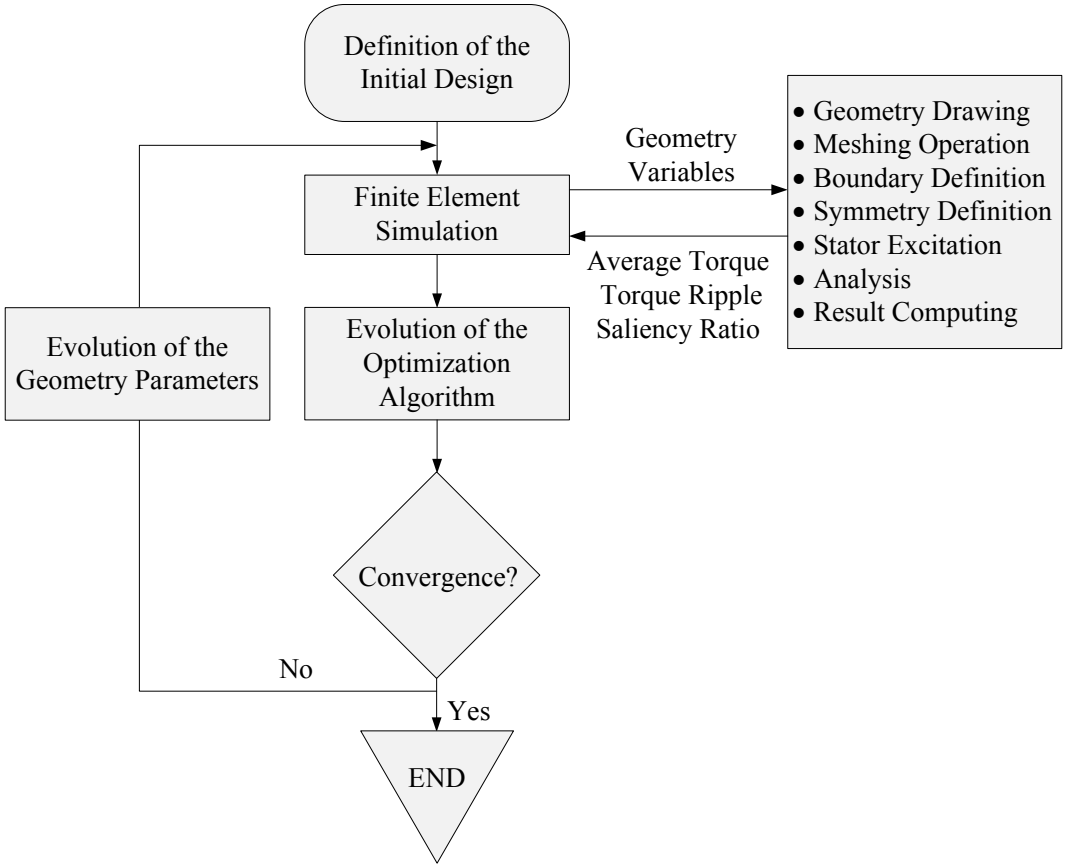

Fig. 3.3 Optimization methodology schematic for determining the SynRM design.

3.4 Elementary Finite Element Simulation

The FE simulation delivers the average torque, the torque ripple and the saliency ratio results to the optimization algorithm in Matlab for the optimization evolution. One machine pole is sufficient to acquire the simulation results given the symmetries of the machine. Figure 3.4 shows a drawing in Maxwell 2D simulation software with the master and the slave axes. A simulation boundary is added to define the simulation limits. Figure 3.5 shows the meshing adapted for the simulation, and figure 3.6 shows a zoom on the airgap area. The most critical parts of the simulation are the airgap, the ribs and the bridges. In the airgap, Maxwell virtual forces are calculated to obtain the torque and the ribs and bridges undergo a high saturation effect. Therefore, a fine meshing process is adapted in these parts. For instance, the drawing imposes 4 meshing layers in the airgap and 3 meshing layers in the ribs. Moreover, for the core losses estimation, the Bertotti model [82] in used.

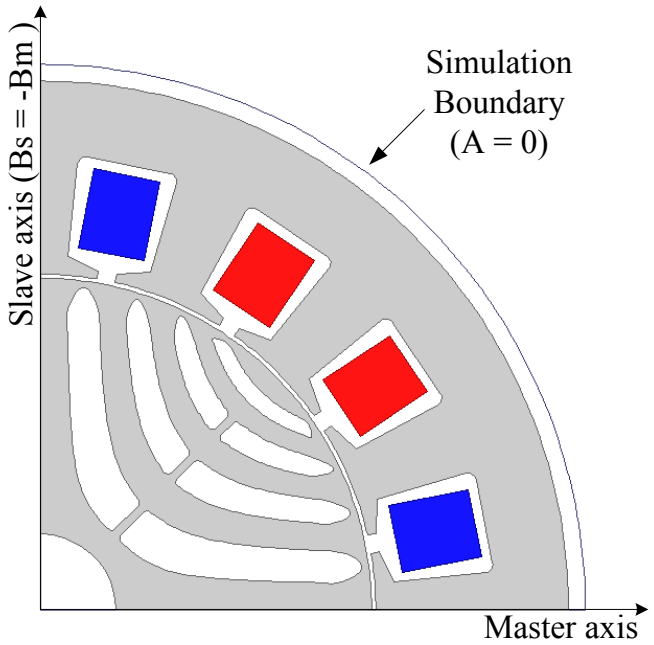

Fig. 3.4 Machine drawing in Maxwell 2D software with the simulation boundary and the master and slave axes.

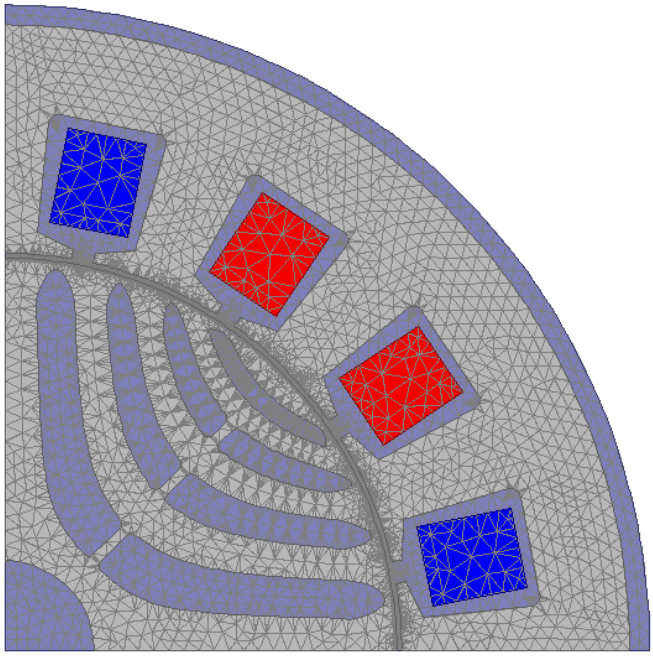

Fig. 3.5 Mesh operation of the machine for simulation.

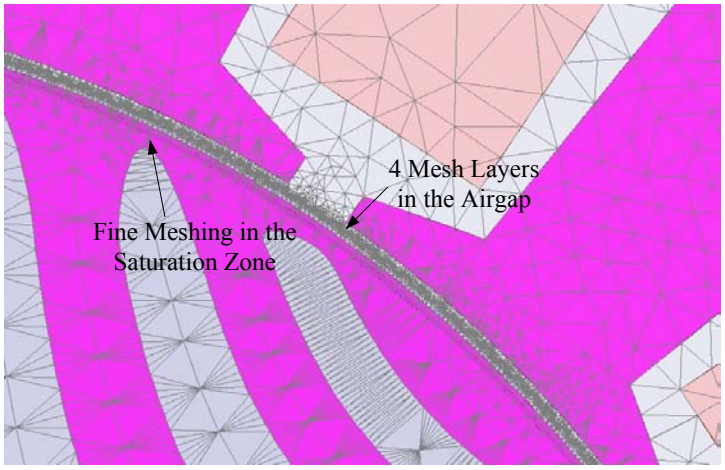

Fig. 3.6 Zoom on the airgap area meshing operation. The ribs zone as well as the airgap area are mesh finely for accurate results.

3.5 Cost Function

The optimization problem consists in solving a multi-objective cost function that can be solved in several manners. For instance, one of the possibilities can be the construction of a "Pareto Front" [83]. The evaluation of the "Pareto Front" can be a complex task, especially when the number of the objectives is equal to or greater than three as in the studied case.

Another possibility consists in transforming the multi-objective problem into a single-objective problem. In what follows, three possibilities will be considered:

- Normalized quadratic error
- Normalized absolute error
- Transformation of the performance indicators into constraints

3.5.1 Normalized Quadratic Error

Opt_i is the mono-objective optimal solution for the performance indicator PI_i. The normalized quadrature error nqe_i of a given solution with respect to the optimal solution is given by:

$$nqe_i = \left(\frac{PI_i - Opt_i}{Opt_i} \right)^2 \tag{3.3}$$

The general cost function F_1 that groups the three performance indicators can then be defined based on the normalized quadrature error as the following:

$$F_1 = \sum_{i=1}^{3} a_i.nqe_i = \sum_{i=1}^{3} a_i \left(\frac{PI_i - Opt_i}{Opt_i} \right)^2 \tag{3.4}$$

where $i \in \{1, 2, 3\}$ and $\sum_{i=1}^{3} a_i = 1$. a_i is defined according to relative importance of a criterion to the other two criteria.

3.5.2 Normalized Absolute Error

For a given Opt_i resulting of a mono-objective optimization of the performance indicator PI_i, a normalized absolute error nae_i is defined as follows:

$$nae_i = \left| \frac{PI_i - Opt_i}{Opt_i} \right| \tag{3.5}$$

The cost function F_2, grouping the three performance indicators, can be defined based on the normalized absolute error as:

$$F_2 = \sum_{i=1}^{3} b_i.nae_i = \sum_{i=1}^{3} b_i \left| \frac{PI_i - Opt_i}{Opt_i} \right|, \tag{3.6}$$

where $i \in \{1, 2, 3\}$ and $\sum_{i=1}^{3} b_i = 1$.

3.5.3 Transformation of the Performance Indicators into Constraints

Among the three performance indicators, two of them could be changed into constraints. This can be done by multiplying the obtained Opt_i by a percentage of tolerance. For instance, when Opt_i is multiplied by 0.8 and transformed into an inequality constraint, the algorithm would not except a deterioration of the given PI_i for more than 20% from its optimal value. In this study, the PI related to the torque and the saliency ratio are transformed into constraints and the cost function F_3 will handle the minimization of the torque ripple:

$$\begin{aligned} &F_3 = PI_2, \\ &C_1 : PI_1 > c_1 * Opt_1, \\ &C_2 : PI_3 > c_2 * Opt_3, \end{aligned} \tag{3.7}$$

where $(c_1, c_2) \in [0, 1]^2$.

The same optimization algorithm (Fminsearch in Matlab) was performed using the three different cost functions proposed. The variation of PI_i with respect to the mono-objective optimization Opt_i is presented in table 3.2. A uniform weight is given to the performance indicators in F_1 and F_2, therefore (a_i and b_i) are equal to 1/3. Moreover, in F_3, $\{c_1, c_2\}$ are considered equal to 0.8.

The smaller the absolute value of the variations with respect to the Opt_i, the better the cost function is.

F_1 and F_3 give similar results, and on the torque ripple level, they give better results than F_2. However, F_2 gives better results in both average torque and saliency ratio. In order to change the resulting $PI's$ after the optimization, the coefficients a_i, b_i and c_i can be changed. The condition on the saliency ratio is the most strict in F_3, and by making this constraint more lenient, the torque ripple can be reduced. In that sense, the performance indicators are better controlled in cost function F_3 with respect

	Average Torque (PI_1)	Torque Ripple (PI_2)	Ld/Lq (PI_3)
F_1	-7.3%	+20%	-20%
F_2	-5.4%	+27%	-15%
F_3	-7.5%	+20.8%	-20%

Table 3.2 Variation of the performance indicators (PI_i) with respect to the mono-objective optimum (Opt_i) for the three proposed cost functions.

to the other two where the user is obliged to evaluate (a_i, b_i) whose direct influence on the optimization is hard to evaluate from a performance point of view.

3.6 Optimization Algorithm

For a non-convex mathematical problem like the case in the present study, the local search based optimization algorithm cannot guarantee a global optimum point. Therefore, an optimization algorithm can be evaluated upon two criteria : the value of the cost function on the local optimum point and the time of execution. In the present case, the cost function is not an explicit algebraic function but a result of a simulation. This kind of problem is known as a black box optimization problem. The optimization algorithms makes decisions depending on the evolution of the results of the simulation. The time of execution (linked to the number of iterations of the FE simulations) is a crucial point to study since the simulation iteration costs heavily in terms of CPU time.

In the goal of evaluating the different algorithms, their families are presented. In general, optimization algorithms can be divided into 2 large families:

- Gradient based algorithms: This family groups all algorithms that involve a numerical estimation of the gradient vector or/and the Hessian matrix (example: Quasi-Newton algorithm).
- Derivative free algorithms: This family groups all the algorithms that do not compute any derivative, and it can be divided in 2 parts: evolutionary algorithms and non-evolutionary algorithms:
  - Evolutionary algorithms generate numerous random points (known as a population) and its evolution is inspired by biological phenomena, such as

reproduction, mutation, recombination, and selection (example: Genetic algorithms).

– Non-evolutionary algorithms evolves by try-outs on the objective function directly (example: Nelder-Mead simplex algorithm).

The choice of the algorithm is not obvious, and a comparison of the different algorithm families is important. The properties of the optimization problem are:

- Number of variables : 8
- Black box optimization
- Long elementary evaluation of the cost function (3 - 5 minutes) due to the FE simulations.

Table 3.3 gives a basic idea of the behaviour of different algorithms from different families:

	Quasi-Newton Algorithm	Nelder-Mead Simplex	Genetic Algorithm
# of FEM simulations	about 50	about 300	more than 1000
CPU Time	around 6 hrs	around 20 hrs	around 60 hrs
Convergence	close to the initial point	surpasses local optima	surpasses local optima

Table 3.3 Comparison of the optimization algorithms for an 8 variables optimization problem.

The CPU time is directly linked to the number of FE simulation calls multiplied by the elementary time of each simulation. For our study, the Quasi-Newton algorithm converges with the minimal CPU time but to an optimum close to the starting point. Therefore, local minima are hard to overcome using this algorithm in our case. To get a better optimum point, several initial geometry points should be explored. Nevertheless, this increases the execution time, and this algorithm becomes comparable in time consumption to the Nelder-Mead simplex algorithm.

The genetic algorithm provided by Matlab is heavily time consuming even though good results could be obtained if a wise choice of the code parameters were made. In addition, another disadvantage of the genetic algorithm is the fact that it is not deterministic. In other terms, the solution of two distinct optimizations from the same initial geometry point give two different results.

The Nelder-Mead Simplex algorithm represents a good candidate for this type of optimization problem since it has a relatively low iteration number and has the capability to overcome local optima. In this regard, this algorithm will be adapted to integrate the mechanical constraints of the problem and will be used to optimize the machine performance.

Since the Nelder-Mead algorithm provided by Matlab does not allow us to introduce constraints, the cost will be modified in order to integrate these constraints (refer to equation (3.8)). An extra term of a high value is added to the cost function which will penalize it if the constraints are not satisfied. This leads to the automatic elimination of the solution not satisfying the constraints, and the algorithm will evolve accordingly.

$$F = F + Penality \tag{3.8}$$

3.7 Optimization Results

The initial rotor geometry used for the optimization algorithm will be the design obtained from the analytical design procedure (refer to section 2.4). The stator and other design parameters are shown in table 2.2.

The first step in the optimization process is to determine Opt_1 and Opt_3, the respective mono-objective optimization of the average torque and the saliency ratio. The values are shown in equation (3.9). $c1$ and $c2$ are chosen at 0.9 and 0.8 respectively (refer to 3.7). In other terms, neither a deterioration of the torque to less than 90% of its mono-objective optimal value (average torque $> 2.16Nm$) is accepted, nor a deterioration of the saliency ratio to less than 80% of its mono-objective optimal value (saliency ratio > 2.54).

$$\begin{aligned} Opt_1 &= Opt_{T_{avg}} = 2.4Nm \\ Opt_3 &= Opt_{L_d/L_q} = 3.17 \end{aligned} \tag{3.9}$$

The overall performance of the optimized machine is shown in table 3.4. The overall value of the performances has minimally changed except for the torque ripple and L_q.

The value of L_q has increased (decreasing the saliency ratio) in favour of decreasing the torque ripple. In other terms, the optimization has put more iron in the rotor to decrease the torque ripple. The design of the initial and optimized machines is shown in figure 3.7, and the comparison of their torque evolution is shown in figure 3.8. Finally, a comparison of the torque, torque ripple and machine electromagnetic power between the initial design and the optimized design from $0rpm$ up till $7000rpm$ is shown on figure 3.9. Even if a slight deterioration in the optimized machine torque is detected with respect to the initial, an improvement on the torque ripple of the machine on the whole speed range is observed. Consequently, the optimization on one operation point of the machine can lead to the minimization of the torque ripple on the entire performance envelope of the machine.

	Analytical Design	Optimized Design	Difference
Current Amplitude I (A)	10	10	–
Current Angle θ (°)	51	51	–
Rotation Speed (rpm)	3500	3500	–
Phase Induced Voltage (V_{rms})	112	111.5	−0.4%
L_d (mH)	38.4	38.0	−1%
L_q (mH)	14.3	14.9	+4.2%
Saliency Ratio (−)	2.69	2.55	5.2%
Average Torque (Nm)	2.21	2.16	−2.2%
Torque Ripple (−)	28%	13%	−53.6%
Power Factor (−)	0.52	0.50	−3.8%
Efficiency (η)	93	94	+1.06%
Core Losses (W)	31	20.8	−32.9%

Table 3.4 Performance comparison between the design based on the analytical approach and the optimized machine design on nominal operation point.

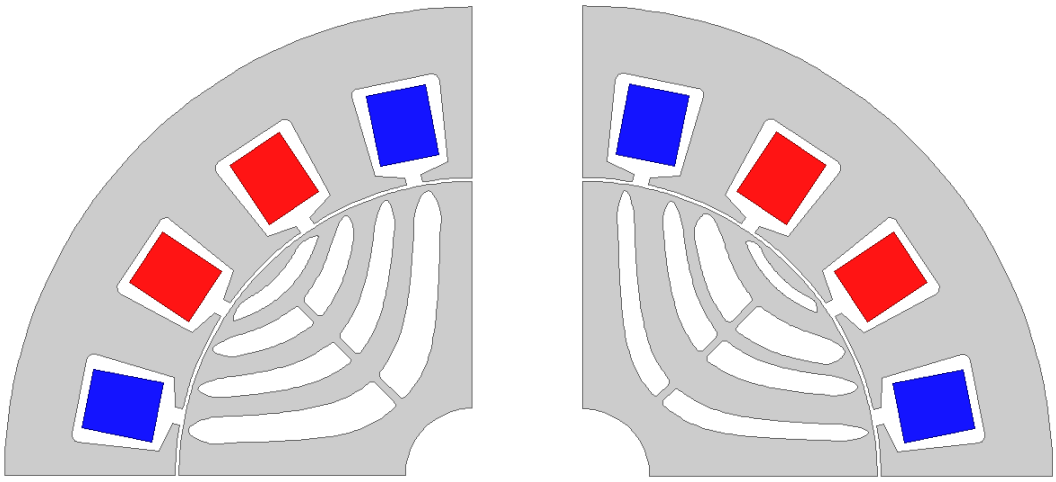

(a) (b)

Fig. 3.7 Design optimization of the SynRM :(a) the design based on the analytical procedure and (b) the optimized design.

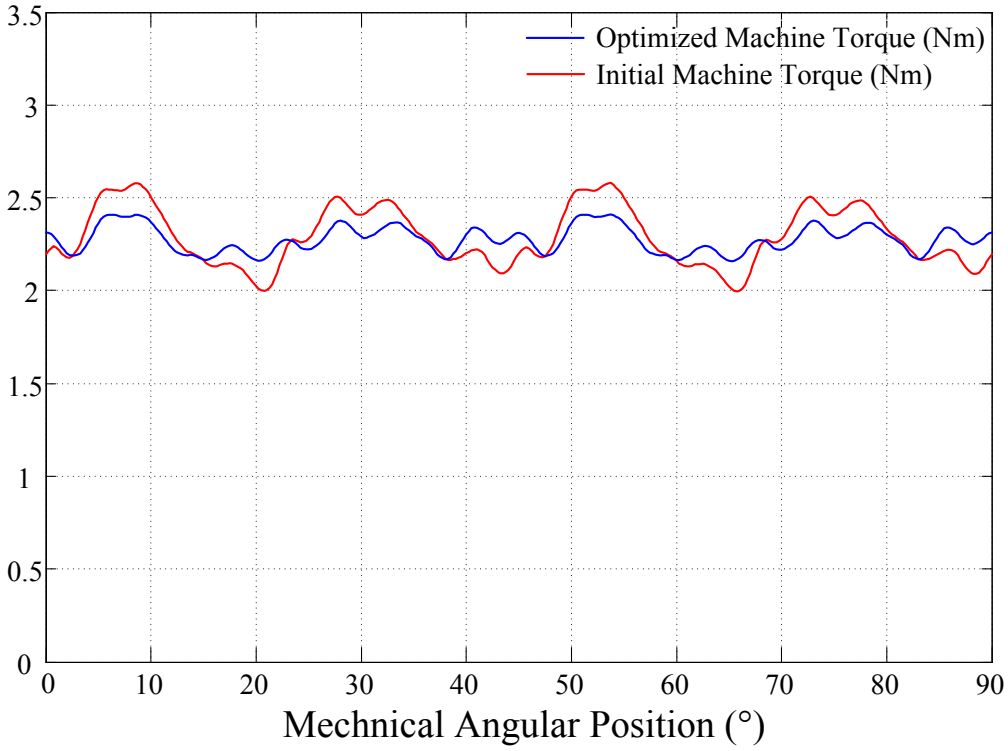

Fig. 3.8 Torque comparison between the initial and the optimized designs.

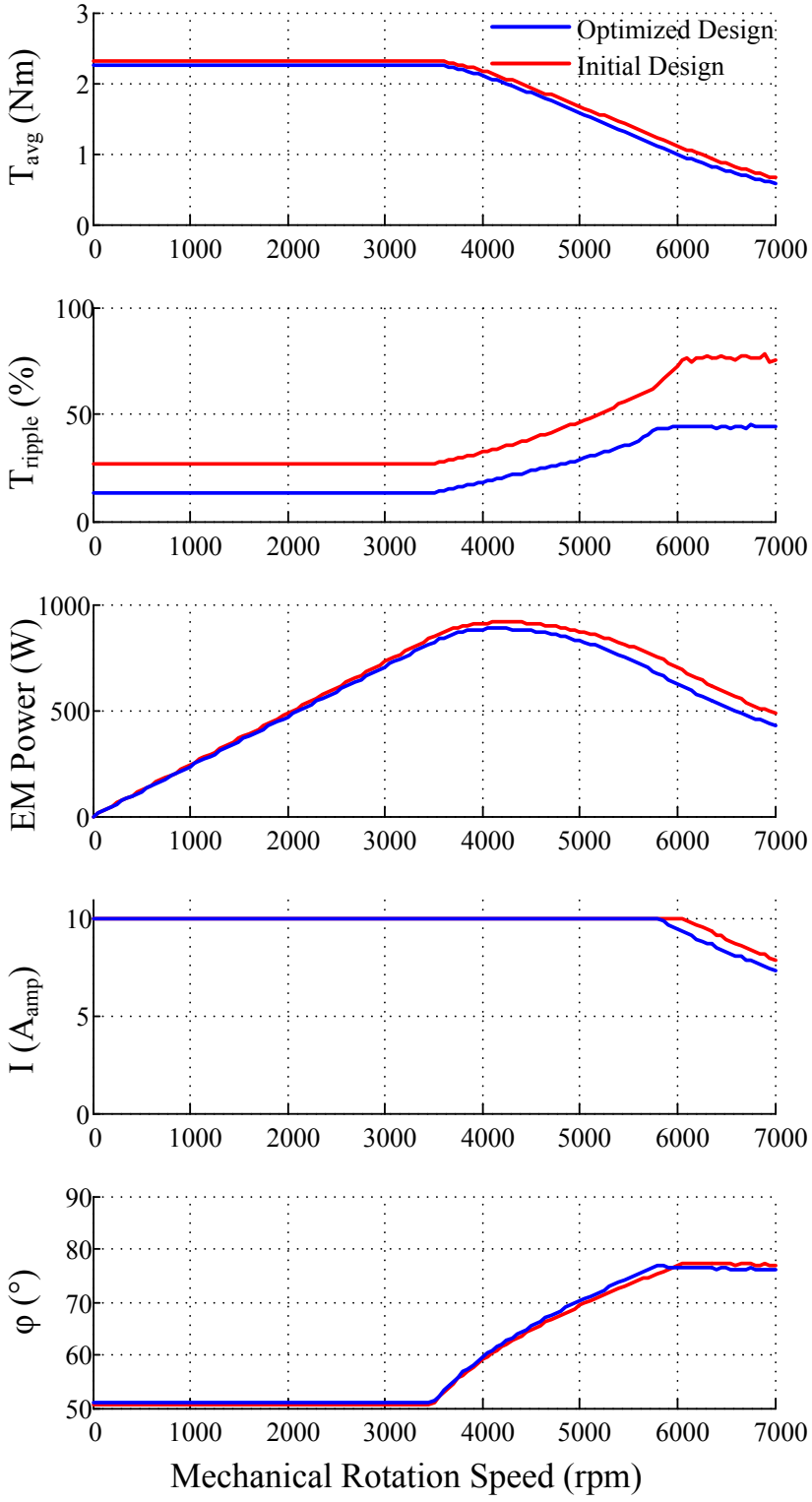

Fig. 3.9 Performance comparison between the optimized and the initial machine designs on the performance envelope.

3.8 Mechanical Validation of the Optimized Design

The Von Mises element stress test is shown on figure 3.10. The steel used for the design is $M400-35A$ the same as the one used in chapter 2. The elastic limit is 385 MPa and the Young's modulus is of 225000 MPa. The maximal reported stress at 10500 rpm is around 90 MPa which is largely underneath the elastic limit of the machine and is considered safe at the maximal speed. Moreover, the maximal deformation of the rotor for the 10500 rpm is 5.7 μm or 1.1 % of the airgap length.

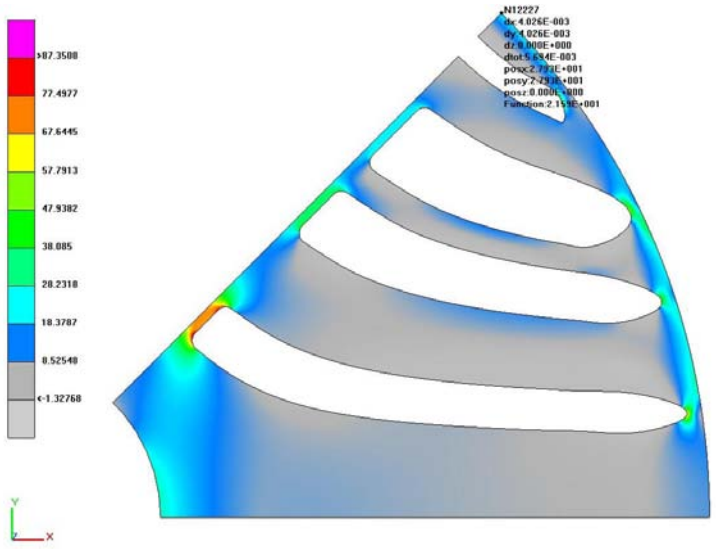

Fig. 3.10 Rotor stress (Von Mises stress) and mechanical deformation for the optimized design at 10500 rpm.

Chapter Conclusion

This chapter presents an optimization study aimed to decrease the torque ripple of the SynRM keeping the saliency ratio and the average torque at an acceptable level. The rotor design is automated using 2 variables per flux barriers, and the flux barriers' border are drawn following the flux lines in a solid rotor. The optimization algorithm is coupled with transient Maxwell 2D FE simulations to find the form of the machine torque and deduce the torque ripple and the average torque. Three optimization algorithms belonging to the optimization algorithms' main families are discussed are the Nelder Mead Simplex is found appropriate for this type of optimization. In addition, several cost functions are proposed and tested to choose the most appropriate one.

The optimized designs shows a significant decrease in torque ripple with a minimal impact on the machine torque and saliency ratio.

Chapter 4

Harmonics Injection Evaluation for Enhanced Performance

Contents

Besides design, another way to impact the machine performance can be by altering the waveforms of the phase currents and injecting non-sinusoidal components. This concept is not new and is used, for instance, for PMSMs in torque increase [84, 85] or in torque ripple reduction [86]. The current harmonics impact the machine performance since the flux linkages seen by the machine phases are non-sinusoidal [59]. Furthermore, developments in power converters have allowed to easily impose non-sinusoidal current waveforms [87].

Harmonics injection in the SynRM was treated in several studies. In [88, 89], it has been proven that injecting a third harmonic current component can increase a simple saliency rotor SynRM torque per ampere capability. However, adding the third harmonic into a three phase machine with an ordinary winding cannot lead to this torque generation. Therefore, different winding topologies or different phase numbers have to be considered. For instance, in [90, 91], a 3-phase full-pitch 2-pole winding for 12-slots is used for the generation of the fundamental Magneto-Motive Force (MMF) from the fundamental current component. A 2-phase 6-pole is added to the winding to add the third harmonic component. The final circuit configuration will impose the use of a dual 3-phase machine having 6 isolated winding. Moreover, in [87–89, 92–94], the use of a 5-phase machine is considered. This will reduce the number of windings, reducing the number of power converter switches used. It is stated in these works that using a 5-phase machine leads to the minimal number of switches when the use of the third harmonic is desired. In addition, in [93], it has been revealed that the 3^{rd} harmonic injection in a 5-phase ALA SynRM deteriorates the torque per ampere capability. However, this chapter will put these hypotheses to the test by developing a general harmonics injection study.

The aim of this chapter is to evaluate harmonics injection in the phase current in a general manner (harmonics 3, 5, etc..) for an m-phase machine and the harmonics effect on torque ripple and average torque. To do that, the torque will be first modelled and the developed model will be compared to finite elements simulations. The harmonic injection will be studied on the developed model and will be tested for the 2-phase SynRM developed in chapter 2. Finally, the adapted control laws are developed and simulated in order to implement them on the test bench.

4.1 Model of an m-Phase SynRM

The SynRM can be modelled using three domains: The electric domain, the electromagnetic domain and the mechanical domain. The electric domain describes the behaviour of the phase voltages and the phase currents. Whereas, the electromagnetic domain specifies the behaviour of the developed electromagnetic torque. Finally, the mechanical domain describes the angular speed (Ω_{mec}) and the angular position (θ_{mec}) of the machine taking into account the torques acting on the SynRM.

4.1.1 Electric Model

In order to develop the electric model of the machine, first the fundamental equation of the stator voltages can be written under their matrix form as the following:

$$V_s = R_s I_s + \frac{d\lambda_s}{dt} \tag{4.1}$$

where V_s, R_s, I_s, λ_s are the stator phases' voltages, resistances, currents and flux linkages respectively. These variables can be written in their matrix form for a m-phase machine:

$$\begin{aligned} V_s &= \begin{bmatrix} V_a & V_b & \dots & V_m \end{bmatrix}^t \\ I_s &= \begin{bmatrix} I_a & I_b & \dots & I_m \end{bmatrix}^t \\ \lambda_s &= \begin{bmatrix} \lambda_a & \lambda_b & \dots & \lambda_m \end{bmatrix}^t \end{aligned} \tag{4.2}$$

$$R_s = r_s.\mathbb{1}_m \tag{4.3}$$

where r_s is the resistance of each coil as we assume that the coils are identical and $\mathbb{1}_m$ is the identity matrix of dimensions $m * m$.

The flux linkages of the winding , λ_s, can be expressed as a function of the stator currents by using the inductance matrix:

$$\lambda_s = L_{ss} I_s \tag{4.4}$$

$$L_{ss} = \begin{bmatrix} L_{aa} & L_{ab} & \dots & L_{am} \\ L_{ab} & L_{bb} & \dots & L_{bm} \\ \vdots & \vdots & \ddots & \vdots \\ L_{am} & L_{bm} & \dots & L_{mm} \end{bmatrix} \tag{4.5}$$

Therefore, substituting (4.4) in (4.1), the stator voltages can be written as:

$$V_s = R_s I_s + L_{ss}\frac{dI_s}{dt} + \Omega_{mec}\frac{dL_{ss}}{d\theta_{mec}}I_s \tag{4.6}$$

where Ω_{mec} represents the rotor mechanical speed and is defined as:

$$\Omega_{mec} = \frac{d\theta_{mec}}{dt} \tag{4.7}$$

4.1.2 Co-Energy and Electromagnetic Torque

The electromagnetic torque can be derived from the machine's co-energy W_{co} as the following [95]:

$$T_{em} = \left|\frac{\partial W_{co}}{\partial \theta_{mec}}\right|_{I_s constant} \tag{4.8}$$

If the system is considered as magnetically linear, the coenergy can be written as in (4.9) since there are no excitation in the rotor.

$$W_{co} = \frac{1}{2} I_s^t L_{ss} I_s \tag{4.9}$$

Hence, by replacing (4.9) in (4.8), the following equation is written:

$$T_{em} = \frac{1}{2} I_s^t \frac{\partial L_{ss}}{\partial \theta_{mec}} I_s \tag{4.10}$$

The angle θ_e represents the rotor displacement in electrical radians:

$$\theta_e = p\theta_{mec} \tag{4.11}$$

where p is the number of pole pairs. Hence,

$$T_{em} = \frac{1}{2} p I_s^t \frac{\partial L_{ss}}{\partial \theta_e} I_s \tag{4.12}$$

4.1.3 Mechanical Model

The mechanical model of the machine can be represented using Newton's second law for rotating objects:

$$\sum Torque = J.\frac{d\Omega_{mec}}{dt} \tag{4.13}$$

where J is the system's angular inertia. The mechanical losses in the system will be neglected as well as the static friction. Therefore, the mechanical model of the machine can be written as:

$$T_{em} - T_{load} = J.\frac{d\Omega_{mec}}{dt} + f_v\Omega_{mec} \tag{4.14}$$

where f_v and T_{load} represent the mechanical viscous friction and the load torque introduced to the machine respectively.

4.1.4 Comparison with the Finite Element Simulation

The inductances used for simulating the model are the result of FE simulations at nominal operation point. The saturation issue is due to the fact that the inductances are in function of the current amplitudes in addition to the rotor position. This leads to a non-linear system. In the present chapter, the inductances are considered independent of the current amplitude and the inductance values at nominal operation point are obtained from Maxwell 2D FE simulations. For that reason, the developed models have a domain of validity where the inductances vary slightly with respect to the current amplitude.

In figure 4.1, the average electromagnetic torque derived from the co-energy theorem is plotted as well as the average torque from an FE simulation. During model verification, the current used does not contain harmonic components. The model estimates well the FE simulation in a good manner until $1.5I_{nominal}$ after which the models diverges from the FE solution. This is primarily due to the reason that the model does not take the saturation into account while the machine highly saturates when the current increase.

In figure 4.2, the torque response of the machine is shown when a voltage excitation is applied. The value of the voltage is chosen in order to stay in the unsaturated regime. The model developed in the previous paragraph is shown to be a good approximation of the finite element simulation in estimating the instantaneous torque. Therefore, the model can help us estimate the torque ripple of the machine without having to carry out the FE simulation.

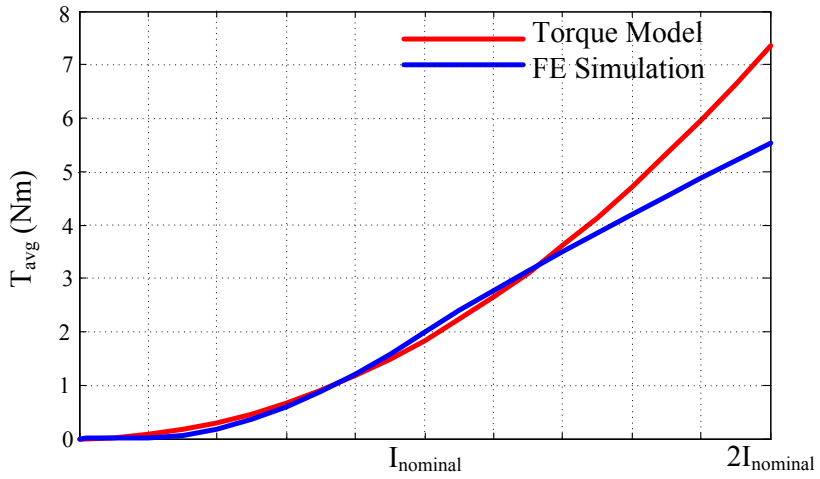

Fig. 4.1 Comparison of the average torque as a function of the phase currents amplitude.

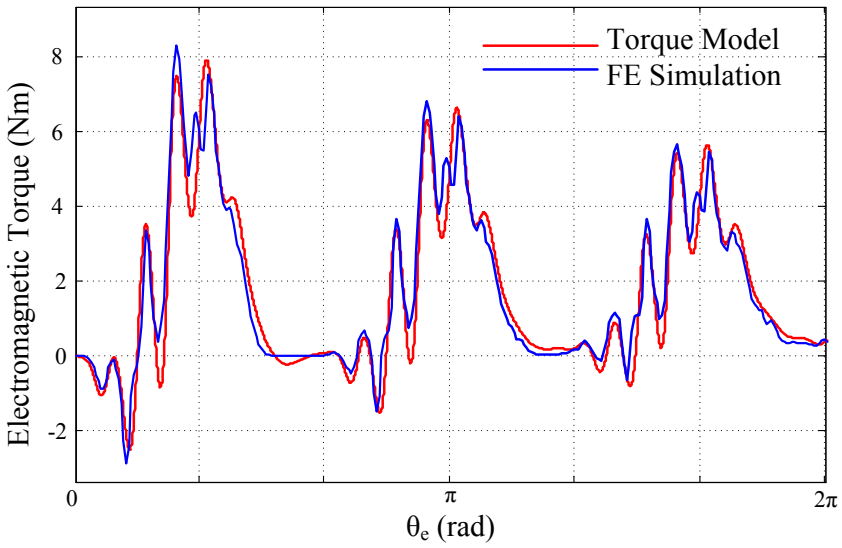

Fig. 4.2 Comparison of the torque response due to a sinusoidal voltage excitation.

4.2 Torque Production due to Current Harmonics

The average electromagnetic torque is derived from the instantaneous torque using the following equation:

$$T_{avg} = \frac{1}{2\pi}\int_0^{2\pi}\frac{1}{2}pI_s^t\frac{\partial L_{ss}}{\partial\theta_e}I_s d\theta_e \tag{4.15}$$

In addition, the torque ripple is defined as the following:

$$T_{ripple} = \frac{max(T_{em}) - min(T_{em})}{T_{avg}} = \frac{\Delta T}{T_{avg}} \tag{4.16}$$

In order to study the effect of the current harmonics injection, the inductances should be written under their general form with their spatial harmonic content.

4.2.1 Inductance Matrix Including the n^{th} Harmonic

The inductances in a machine are bi-periodic over an electric period. Figure 4.3 shows the self-inductance of a phase in a TLA SynRM. Equations (4.17) and (4.18) show the Fourier series decomposition under its general form of the inductance matrice of an m-phase SynRM. Matrix L^0 include the average value of the inductances, whereas matrices L^{2nC} and L^{2nS} describe the spatial harmonics components of the inductances.

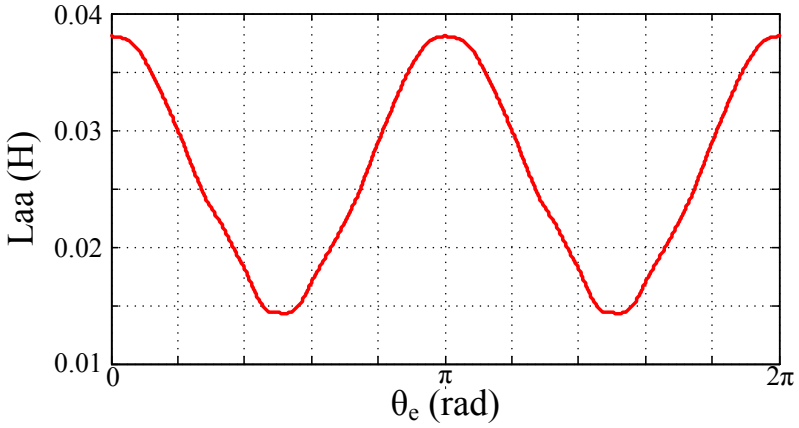

Fig. 4.3 Phase self-inductance of a Transversally Laminated Anisotropic (TLA) SynRM.

$$L_{ss} = L^0 + \sum_{n=1}^{\infty}[L^{2nC}]cos2n\theta_e + \sum_{n=1}^{\infty}[L^{2nS}]sin2n\theta_e \tag{4.17}$$

where

$$
\begin{aligned}
L^0 &= \begin{bmatrix} L^0_{aa} & L^0_{ab} & \dots & L^0_{am} \\ L^0_{ab} & L^0_{bb} & \dots & L^0_{bm} \\ \vdots & \vdots & \ddots & \vdots \\ L^0_{am} & L^0_{bm} & \dots & L^0_{mm} \end{bmatrix} \\
L^{2nC} &= \begin{bmatrix} L^{2nC}_{aa} & L^{2nC}_{ab} & \dots & L^{2nC}_{am} \\ L^{2nC}_{ab} & L^{2nC}_{bb} & \dots & L^{2nC}_{bm} \\ \vdots & \vdots & \ddots & \vdots \\ L^{2nC}_{am} & L^{2nC}_{bm} & \dots & L^{2nC}_{mm} \end{bmatrix} \\
L^{2nS} &= \begin{bmatrix} L^{2nS}_{aa} & L^{2nS}_{ab} & \dots & L^{2nS}_{am} \\ L^{2nS}_{ab} & L^{2nS}_{bb} & \dots & L^{2nS}_{bm} \\ \vdots & \vdots & \ddots & \vdots \\ L^{2nS}_{am} & L^{2nS}_{bm} & \dots & L^{2nS}_{mm} \end{bmatrix}
\end{aligned}
\tag{4.18}
$$

$L_{ij} = L_{ji}$ due to machine symmetries.

4.2.2 Phase Currents Including the $(2N-1)^{th}$ Harmonic

The m stator currents can be written under their general form as in (4.19). Even current harmonics do not generate torque, therefore only odd harmonics are introduced. Moreover, the order of harmonics is limited to $2N-1$ where $N \in \mathbb{N}^*$. The current amplitude of a given harmonic (H) is defined by I_H, and its phase with respect to the rotor d-axis is represented by ϕ_H.

$$
\begin{aligned}
I_a &= \sum_{k=1}^{N} I_{(2k-1)} cos((2k-1)\omega t + \phi_{(2k-1)}) \\
I_b &= \sum_{k=1}^{N} I_{(2k-1)} cos((2k-1)(\omega t - \frac{2\pi}{m}) + \phi_{(2k-1)}) \\
&\vdots \\
I_m &= \sum_{k=1}^{N} I_{(2k-1)} cos((2k-1)(\omega t - \frac{2(m-1)\pi}{m}) + \phi_{(2k-1)})
\end{aligned}
\tag{4.19}
$$

Furthermore, the SynRM is a synchronous machine where the rotor mechanical rotation is linked directly to the current frequency by the equation (4.20). If this equation were not satisfied, the output torque would have a zero average value.

$$\omega t = \theta_e = p\theta_{mec} \tag{4.20}$$

4.2.3 Resultant Average Torque for an m-Phase Machine

The resultant average torque, replacing (4.17) and (4.19) in (4.15) and applying the synchronous condition ($\omega t = \theta_e = p\theta_{mec}$), is:

$$\begin{aligned}
T_{avg} = \frac{mp}{2}[&I_1^2 \sum_{\substack{i=1\ldots m\\ j=1\ldots m}} k_{ij}^1 L_{ij}^2 sin(2\phi_1) \\
&+I_3^2 \sum_{\substack{i=1\ldots m\\ j=1\ldots m}} k_{ij}^3 L_{ij}^6 sin(2\phi_3) \\
&+I_5^2 \sum_{\substack{i=1\ldots m\\ j=1\ldots m}} k_{ij}^5 L_{ij}^{10} sin(2\phi_5) \\
&\vdots \\
&+I_{2N-1}^2 \sum_{\substack{i=1\ldots m\\ j=1\ldots m}} k_{ij}^{2N-1} L_{ij}^{2(2N-1)} sin(2\phi_{2N-1}) \\
&+I_1 I_3 \sum_{\substack{i=1\ldots m\\ j=1\ldots m}} l_{ij}^{13} L_{ij}^2 sin(\phi_1 - \phi_3) \\
&+I_1 I_3 \sum_{\substack{i=1\ldots m\\ j=1\ldots m}} m_{ij}^{13} L_{ij}^4 sin(\phi_1 + \phi_3) \\
&+I_1 I_5 \sum_{\substack{i=1\ldots m\\ j=1\ldots m}} l_{ij}^{15} L_{ij}^4 sin(\phi_1 - \phi_5) \\
&+I_1 I_5 \sum_{\substack{i=1\ldots m\\ j=1\ldots m}} m_{ij}^{15} L_{ij}^6 sin(\phi_1 + \phi_5) \\
&+I_3 I_5 \sum_{\substack{i=1\ldots m\\ j=1\ldots m}} l_{ij}^{35} L_{ij}^2 sin(\phi_3 - \phi_5) \\
&+I_3 I_5 \sum_{\substack{i=1\ldots m\\ j=1\ldots m}} m_{ij}^{35} L_{ij}^8 sin(\phi_3 + \phi_5) \\
&+\ldots]
\end{aligned} \tag{4.21}$$

k_{ij}, l_{ij} and m_{ij} are constants that depend on the machine phase number.

Two non-zero average torque generating mechanisms can be noted from equation (4.21):

1. The u^{th} current harmonic generates a torque with a non-zero average value when it interacts with the inductance's $2u^{th}$ spatial harmonic. The torque can be written under the form:

$$T_{avg}(u) = \frac{1}{2} mpI_u^2 \sum_{\substack{i=1...m \\ j=1...m}} k_{ij}^u L_{ij}^{2u} sin(2\phi_u)$$

2. The x^{th} current harmonic interacts with the y^{th} harmonic via the two inductance space harmonics $x - y$ and $x + y$ and the average torque delivered by this interaction is:

$$T_{avg}(xy) = \frac{1}{2} mpI_x I_y \sum_{\substack{i=1...m \\ j=1...m}} [m_{ij}^{xy} L_{ij}^{x+y} sin(\phi_x + \phi_y) + l_{ij}^{xy} L_{ij}^{|x-y|} sin(\phi_x - \phi_y)]$$

In this section, the general torque equations with harmonic injection for an m-phase machine are shown. It is proven from the developed model that the harmonics interact with the machine inductances spatial spectrum in order to obtain a torque with a non-zero average value. However, this torque depends highly on the amplitudes of the inductances' spectrum. Therefore, if theses amplitudes are negligible the harmonic injection would not have a reasonable advantage.

4.3 Case Study: 2 Phase Machine

The model developed is applied to a 2-phase machine since there are two advantages in using a 2-phase machine for harmonic injection:

1. All odd current harmonics can be injected in contrast with the 5-phase machine where the 5^{th} harmonic cannot be injected.

2. The number of required inverter legs is 4 in comparison with 5 legs for a 5-phase machine.

In this section, the average torque in the presence of current harmonics in a 2-phase machine will be presented. The machine design presented in chapter 2 will be used

in order to investigate the developed model after discussing the model in a general 2-phase machine configuration.

4.3.1 General Case

The semi-circuit representation of a 2-phase machine is shown on figure 4.4(a) and the machine cross section in figure 4.4(b). Moreover, the self and mutual inductances obtained from a Maxwell 2D FE simulation are shown in figure 4.5. It can be observed that the self inductances L_{aa} and L_{bb} are pair as a function of the electric angular displacement θ_e, whereas the mutual inductance L_{bb} is an odd function. Therefore, the self inductance (L_{aa}) can be written in its general form as in (4.22). Phase b is in quadrature with respect to phase a. Therefore, self inductance L_{bb} is linked to L_{aa} by (4.23). Moreover, L_{ab} is written in its general form as well in (4.24). The general equation of the matrix L_{ss} is shown in (4.25). The developed expression of the inductance harmonic component is limited to the 10^{th} harmonic.

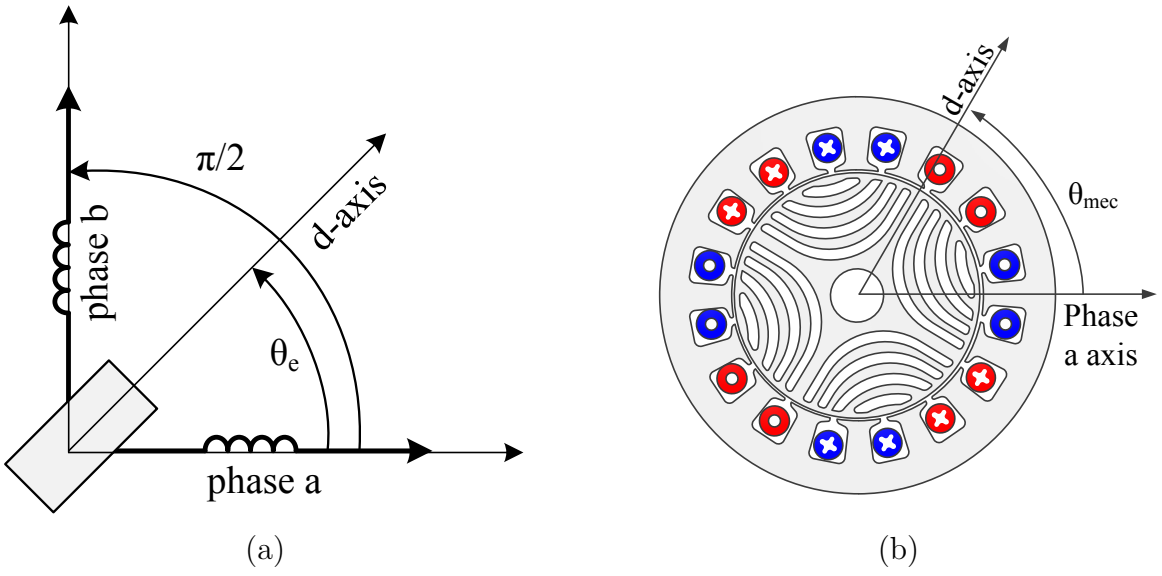

(a) (b)

Fig. 4.4 2-phase SynRM: (a) semi-circuit representation, and (b) cross section of a 4-pole TLA SynRM with 2 slots/phase/pole and a full-pitch winding.

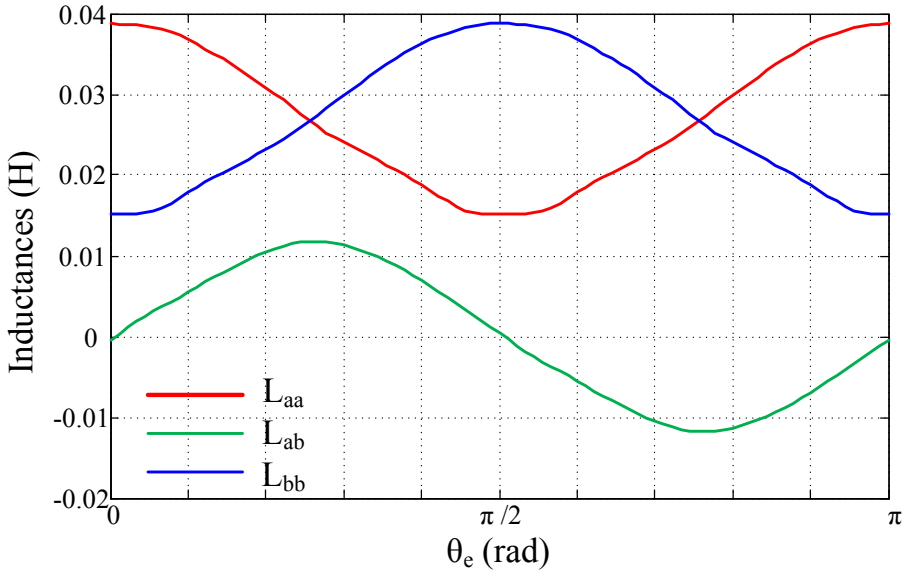

Fig. 4.5 Phase self and mutual inductances in a 2-phase SynRM.

$$Laa = \mathcal{L}_0 + \mathcal{L}_2 cos(2\theta_e) + \mathcal{L}_4 cos(4\theta_e) + \mathcal{L}_6 cos(6\theta_e) + \mathcal{L}_8 cos(8\theta_e) + \dots \tag{4.22}$$

$$Lbb = Laa(\theta_e - \frac{\pi}{2}) \tag{4.23}$$

$$Lab = \mathcal{M}_2 sin(2\theta_e) + \mathcal{M}_4 sin(4\theta_e) + \mathcal{M}_6 sin(6\theta_e) + \mathcal{M}_8 sin(8\theta_e) + \dots \tag{4.24}$$

$$\begin{aligned} L_{ss} = \begin{bmatrix} L_{aa} & L_{ab} \\ L_{ab} & L_{bb} \end{bmatrix} &= \begin{bmatrix} \mathcal{L}_0 & 0 \\ 0 & \mathcal{L}_0 \end{bmatrix} + \begin{bmatrix} \mathcal{L}_2 & 0 \\ 0 & -\mathcal{L}_2 \end{bmatrix} cos(2\theta_e) + \begin{bmatrix} 0 & \mathcal{M}_2 \\ \mathcal{M}_2 & 0 \end{bmatrix} sin(2\theta_e) \\ &+ \begin{bmatrix} \mathcal{L}_4 & 0 \\ 0 & \mathcal{L}_4 \end{bmatrix} cos(4\theta_e) + \begin{bmatrix} 0 & \mathcal{M}_4 \\ \mathcal{M}_4 & 0 \end{bmatrix} sin(4\theta_e) + \begin{bmatrix} \mathcal{L}_6 & 0 \\ 0 & -\mathcal{L}_6 \end{bmatrix} cos(6\theta_e) \\ &+ \begin{bmatrix} 0 & \mathcal{M}_6 \\ \mathcal{M}_6 & 0 \end{bmatrix} sin(6\theta_e) + \begin{bmatrix} \mathcal{L}_8 & 0 \\ 0 & \mathcal{L}_8 \end{bmatrix} cos(8\theta_e) + \begin{bmatrix} 0 & \mathcal{M}_8 \\ \mathcal{M}_8 & 0 \end{bmatrix} sin(8\theta_e) \\ &+ \begin{bmatrix} \mathcal{L}_{10} & 0 \\ 0 & -\mathcal{L}_{10} \end{bmatrix} cos(10\theta_e) + \begin{bmatrix} 0 & \mathcal{M}_{10} \\ \mathcal{M}_{10} & 0 \end{bmatrix} sin(10\theta_e) \end{aligned} \tag{4.25}$$

On the other hand, the phase currents are also limited to their 5^{th} harmonic (equation (4.26)). Hence, the developed average torque is shown in equation (4.27).

$$\begin{aligned} I_a &= I_1 cos(\omega t + \phi_1) + I_3 cos(3\omega t + \phi_3) + I_5 cos(5\omega t + \phi_5) \\ I_b &= I_1 cos((\omega t - \frac{\pi}{2}) + \phi_1) + I_3 cos(3(\omega t - \frac{\pi}{2}) + \phi_3) + I_5 cos(5(\omega t - \frac{\pi}{2}) + \phi_5) \end{aligned} \tag{4.26}$$

$$\begin{aligned} T_{avg} = \frac{p}{2}[&{I_1}^2(\mathcal{L}_2 + \mathcal{M}_2)sin(2\phi_1) + 3I_3^2(\mathcal{L}_6 + \mathcal{M}_6)sin(2\phi_3) + 5I_5^2(\mathcal{L}_{10} + \mathcal{M}_{10})sin(2\phi_5) \\ &+2I_1I_3(-\mathcal{L}_2 + \mathcal{M}_2)sin(\phi_1 - \phi_3) + 4I_1I_5(-\mathcal{L}_4)sin(\phi_1 - \phi_5) \\ &+ 2I_3I_5(-\mathcal{L}_2 - \mathcal{M}_2)sin(\phi_3 - \phi_5) + 4I_1I_3(\mathcal{L}_4)sin(\phi_1 + \phi_3) \\ &+ 8I_3I_5(\mathcal{L}_8)sin(\phi_3 + \phi_5) + 6I_1I_5(\mathcal{L}_6 + \mathcal{M}_6)sin(\phi_1 + \phi_5)] \end{aligned} \tag{4.27}$$

The average torque shows the respective contributions of the current fundamental and harmonics, and the interactions between the various harmonics as in the case of an m-phase machine. The complexity of this analytical model lies in the high interdependence of the harmonics. In other terms, the variation of one parameter (I_H or ϕ_H) influences many terms of the equation, and the contribution of a current harmonic depends on the other harmonics injected in the system. In order to evaluate the model and the harmonic injection concept, the next paragraph studies the machine design based on the analytical procedure developed in Chapter 2.

4.3.2 Harmonics Injection in a Specific SynRM Design

The first step to evaluate the harmonic injection concept is to determine the inductances spectrum of the machine. Many attempts were made in literature to find their expression analytically in the case of simple saliency, TLA or ALA rotors. The most common approach used is the winding theory [96–103] to determine the stator inductances. In some cases, the slotting effects are taken into account [104, 105]. Furthermore, in other cases, a reluctance network is identified in order to evaluated the airgap field [59]. The airgap field can then be used to find the stator inductances. However, it is a complex task to determine the stator inductances analytically taking into account the exhaustive non-linearities in the machine. A complete analytical method determining the inductances considering the saturation, the cross coupling, the slotting effect and the leakage inductance is currently non-existent. Therefore, in this work, FE simulations are used in order to determine the machine inductances.

The numerical values determined by an FE simulation for the machine developed in chapter 2 are shown in table 4.1.

$\mathcal{L}_0 = 2.63 \times 10^{-2} H$	
$\mathcal{L}_2 = 1.15 \times 10^{-2} H$	$\mathcal{M}_2 = 1.12 \times 10^{-2} H$
$\mathcal{L}_4 = 1.41 \times 10^{-4} H$	$\mathcal{M}_4 = -1.42 \times 10^{-4} H$
$\mathcal{L}_6 = 4.15 \times 10^{-4} H$	$\mathcal{M}_6 = -3.47 \times 10^{-4} H$
$\mathcal{L}_8 = -3.34 \times 10^{-4} H$	$\mathcal{M}_8 = -1.91 \times 10^{-4} H$
$\mathcal{L}_{10} = 6.18 \times 10^{-5} H$	$\mathcal{M}_{10} = -9.75 \times 10^{-5} H$

Table 4.1 Inductance numerical values found by FE simulations for the studied SynRM.

The inductances' component higher than the fundamental component are relatively low in this geometry unlike the simple saliency geometry [89]. Therefore, the proper effect of the current harmonic is negligible with respect to the fundamental. However, as seen in (4.27), the 3^{rd} harmonic interacts with the 5^{th} harmonic on the fundamental spatial harmonic of the inductances as shown in the following equation drawn from (4.27):

$$2I_3 I_5(-\mathcal{L}_2 - \mathcal{M}_2)sin(\phi_3 - \phi_5) \tag{4.28}$$

This shows that for the TLA geometry, the mere injection of the 3^{rd} harmonic does not significantly contribute to the machine's performance at a constant RMS current. However, the injection of two consecutive current harmonics could be beneficial. Consequently, the current harmonics considered are the 3^{rd} and the 5^{th} harmonics. Six parameters that define the phase current shape have to be considered: (I_1, ϕ_1), (I_3, ϕ_3) and (I_5, ϕ_5). Finding the optimal values from the analytical equation of these parameters in (4.27) is not a straightforward task. Nevertheless, by simplifying (4.27), an estimate on the optimal parameters' values can be obtained.

Using the numerical values of the inductance harmonics in table 4.1, the terms $\mathcal{L}_6 + \mathcal{M}_6$, $\mathcal{L}_{10} + \mathcal{M}_{10}$, $-\mathcal{L}_2 + \mathcal{M}_2$, $\mathcal{L}_4$, $\mathcal{L}_8$ are negligible in comparison with $\mathcal{L}_2 + \mathcal{M}_2$ and $-\mathcal{L}_6 - \mathcal{M}_6$. Therefore, equation (4.27) can be simplified and can be written as:

$$T_{avg} = \frac{p}{2}[I_1^2(\mathcal{L}_2 + \mathcal{M}_2)sin(2\phi_1) + 2I_3 I_5(-\mathcal{L}_2 - \mathcal{M}_2)sin(\phi_3 - \phi_5)] \tag{4.29}$$

In the ideal case, the phase angle ϕ_1 should be 45° and $\phi_3 - \phi_5$ should be $-90°$ to achieve the maximal torque per ampere. If these values are considered, the simplified model will give the following:

$$\frac{T_{avg}}{\frac{p}{2}(\mathcal{L}_2 + \mathcal{M}_2)} = I_1^2 + 2I_3I_5 \tag{4.30}$$

The machine performance should be evaluated at constant RMS current in order to objectively evaluate harmonic injection compared to conventional fundamental excitation only. In consequence, the following constraint should be respected:

$$I_{rms}^2 = \left(\frac{I_1}{\sqrt{2}}\right)^2 + \left(\frac{I_3}{\sqrt{2}}\right)^2 + \left(\frac{I_5}{\sqrt{2}}\right)^2 = \left(\frac{I_{1max}}{\sqrt{2}}\right)^2 \tag{4.31}$$

In terms of current amplitude, the relation can be written as:

$$I_1^2 + I_3^2 + I_5^2 = I_{1max}^2 \tag{4.32}$$

Solving (4.30) and (4.32), the maximal torque is obtained when $I_3 = I_5$. A constant torque is obtained when this condition is respected. Therefore, when injecting harmonics in the SynRM, the same torque as in the case of the conventional sinusoidal currents can be obtained but not more. The locus of the current fundamental and harmonics required to achieve a maximal torque per ampere is shown on figure 4.6.

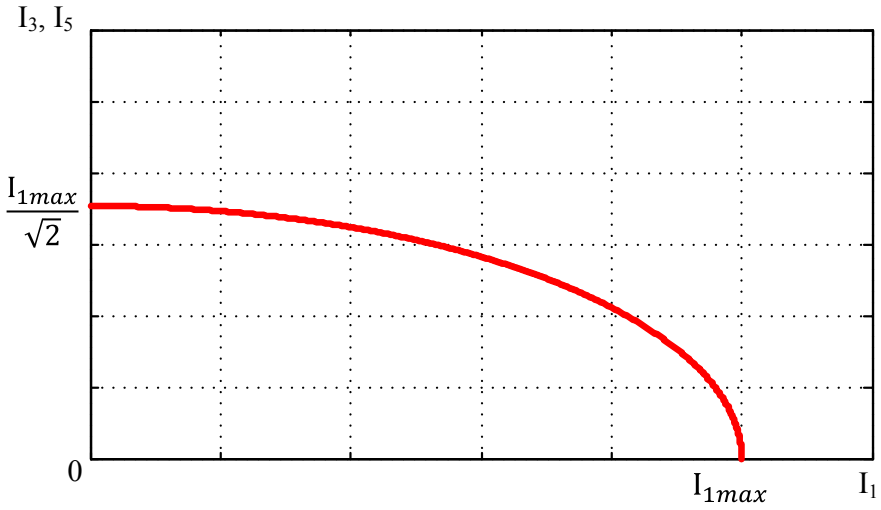

Fig. 4.6 Locus of the maximum torque obtained from the simplified model.

Nonetheless, in order to get a broader perspective of the machine performance under harmonics injection, the whole electromagnetic model (including a rich inductance spectrum) should be taken into account. Since the 3^{rd} and the 5^{th} current harmonics are considered, the inductance spectrum is limited to its 10^{th} component as in (4.25) in the optimization study presented next, and the model used corresponds to equation (4.10).

The optimization algorithm uses the model to help determine the six parameters that define harmonic injection. Two criteria are used to determine the impact of harmonics injection on the machine performance: T_{avg} and T_{ripple}.

The mathematical optimization problem is formulated as:

$$\begin{aligned} &\underset{I_1,I_3,I_5,\phi_1,\phi_3,\phi_5}{max} \quad T_{avg} \\ &C_1 : T_{ripple} < max(T_{ripple}) \\ &C_2 : \sqrt{I_1^2 + I_3^2 + I_5^2} < I_{1max} = 10A \end{aligned} \tag{4.33}$$

The optimization procedure is presented on figure 4.7. The optimization algorithm used is the Nelder-Mead Simplex algorithm ($Fminsearch$ in Matlab).

Figure 4.8 shows the maximal T_{avg} obtained by varying the acceptable T_{ripple} from its lowest value (10%) to its highest acceptable value (35%). At constant I_{rms}, even by injecting harmonics, T_{avg} doesn't surpass T_{avg} achieved without harmonic injection. Nevertheless, for the same T_{avg}, T_{ripple} is reduced from 25% to approximately 15% (-40%). The values of I_1, I_3 and I_5 that give the same T_{avg} and reduce T_{ripple} are roughly the values found from the locus shown on figure 4.6. This proves that the inductance spectrum components higher than $\mathcal{L}_2$ and $\mathcal{M}_2$ do not significantly intervene in the T_{avg} generation.

As a conclusion, although currents harmonics injection does not contribute to the increase of the torque per ampere of the 2-phase TLA SynRM at a constant RMS current, it has the potential to reduce the machine torque ripple at a constant torque. This will be tested on the developed test bench in the next chapter. However, before implementation on the test bench, the control laws for harmonics injection should be established which will be the subject of the next part of this chapter.

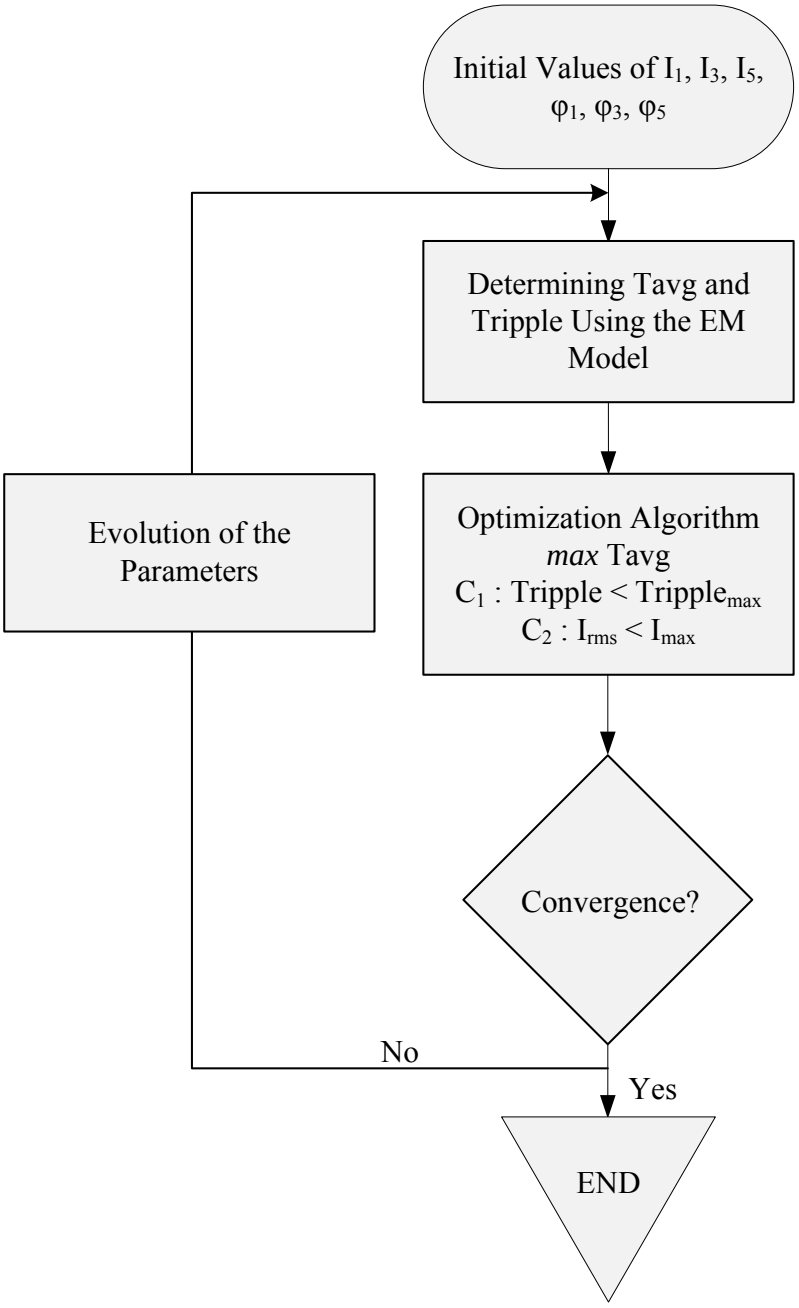

Fig. 4.7 Optimization algorithm to determine the current harmonics parameters.

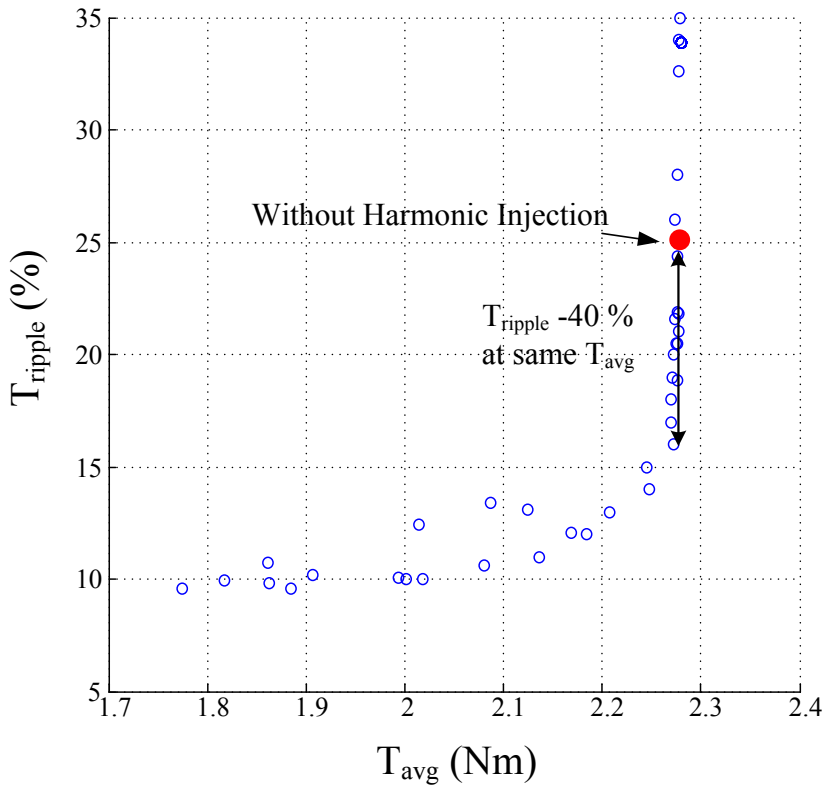

Fig. 4.8 Pareto Front of the T_{ripple} in Function of T_{avg} for the Harmonic Injection Optimization Algorithm.

4.4 Phase Current Control

Now that the harmonics injection has been presented from an electromagnetic point of view, this section will discuss the current control in order to inject current harmonics. The current control should be dynamic in order to control up to the 5^{th} harmonic, yet should eliminate the system noise.

4.4.1 Control Reference

The control reference is the first step in developing the controller study of a system. Conventionally, the *dq* park reference [106, 107] is used for the control of machines. The advantage of the park method is that when controlling the direct and quadrature currents (I_d and I_q), the variables are constant in the sinusoidal steady state state.

However, the direct phase current control (ab control) leads to a control of sinusoidal variables.

In the studied case, the phase currents are non-sinusoidal so a re-evaluation for the dq reference is a must. In [89], the 3^{rd} harmonic was injected in a 5-phase machine, and a (d_1, q_1, d_3, q_3, n) reference was used. The fundamental and the third harmonic in the 5-machine are constant. However, this is not the general case. The next part of this paragraph will introduce a general approach in determining the (dq) for a m-phase system with an n^{th} harmonic injection.

The m-phase currents with the injection of harmonic $n = 2k + 1$ with $k \in \mathbb{N}^*$ are written as the following:

$$\begin{aligned}
I_a &= I_1 cos(\theta_e + \phi_1) + I_{2k+1} cos((2k+1)\theta_e + \phi_{2k+1}) \\
&\vdots \\
I_i &= I_1 cos(\theta_e - 2\left(\frac{i-1}{m}\right)\pi + \phi_1) + I_{2k+1} cos((2k+1)(\theta_e - 2\left(\frac{i-1}{m}\right)\pi) + \phi_{2k+1}) \\
&\vdots \\
I_m &= I_1 cos(\theta_e - 2\left(\frac{m-1}{m}\right)\pi + \phi_1) + I_{2k+1} cos((2k+1)(\theta_e - 2\left(\frac{m-1}{m}\right)\pi) + \phi_{2k+1})
\end{aligned} \tag{4.34}$$

The park transform for the direct current (I_d) and the quadrature current (I_q) is written as the following:

$$\begin{bmatrix} I_d \\ I_q \end{bmatrix} = \begin{bmatrix} cos(\theta_e) & cos(\theta_e - \frac{2\pi}{m}) & \dots & cos(\theta_e - \frac{2\pi(m-1)}{m}) \\ -sin(\theta_e) & -sin(\theta_e - \frac{2\pi}{m}) & \dots & -sin(\theta_e - \frac{2\pi(m-1)}{m}) \end{bmatrix} \begin{bmatrix} I_a \\ I_b \\ \vdots \\ I_m \end{bmatrix} \tag{4.35}$$

The direct current when the current fundamental and the current harmonic are considered is written as the following:

$$I_d = \sqrt{\frac{2}{m}} I_1 \overbrace{\sum_{i=1}^{m} \left[cos((\theta_e - 2\left(\frac{i-1}{m}\right)\pi) cos((\theta_e - 2\left(\frac{i-1}{m}\right)\pi + \phi_1) \right]}^{\text{Main Term}} + I_{2k+1} \overbrace{\sum_{i=1}^{m} \left[cos(\theta_e - 2\left(\frac{i-1}{m}\right)\pi) cos((2k+1)(\theta_e - 2\left(\frac{i-1}{m}\right)\pi) + \phi_{2k+1}) \right]}^{\text{Residual Term}} \tag{4.36}$$

The main term in equation 4.36 gives $\sqrt{\frac{m}{2}} cos(\phi_1)$ for a balanced system. On the other hand, the residual term is zero when $2k \neq mz$ and $2k+2 \neq mz$ where $z \in \mathbb{N}^*$. However, in the case of a two phase system ($m = 2$) and a 3^{rd} harmonic injection ($k = 1$) or a 5^{th} harmonic injection ($k = 2$), the residual term is not zero. Therefore, in the studies case, the dq transform does not give constant values for the harmonic injection. This transform does not have benefits in this case and an (ab) direct current control will be used.

4.4.2 Model of the 2-Phase Machine

This part will deal with the model of a 2-phase machine like what was dealt with in section 4.1 for an m-phase machine. The model will be implemented on Matlab/Simulink in order to test the phase current controllers later.

The stator voltages can be written under their matrix form:

$$V_s = R_s I_s + \frac{d\lambda_s}{dt} \tag{4.37}$$

where V_s, R_s, I_s, λ_s are written for a 2-phase machine as the following:

$$V_s = \begin{bmatrix} V_a & V_b \end{bmatrix}^t, I_s = \begin{bmatrix} I_a & I_b \end{bmatrix}^t, \lambda_s = \begin{bmatrix} \lambda_a & \lambda_b \end{bmatrix}^t \tag{4.38}$$

$$R_s = \begin{bmatrix} r_s & 0 \\ 0 & r_s \end{bmatrix} \tag{4.39}$$

where r_s is the resistance of each coil as it is considered that the coils are identical.

The flux of the winding , λ_s, can be expressed as a function of the stator currents by using the 2-phase inductance matrix as in (4.40) and (4.41).

$$\lambda_s = L_{ss} I_s \tag{4.40}$$

$$L_{ss} = \begin{bmatrix} L_{aa}(\theta_{mec}) & L_{ab}(\theta_{mec}) \\ L_{ab}(\theta_{mec}) & L_{bb}(\theta_{mec}) \end{bmatrix} \tag{4.41}$$

The electric model block diagram is represented on figure 4.9.

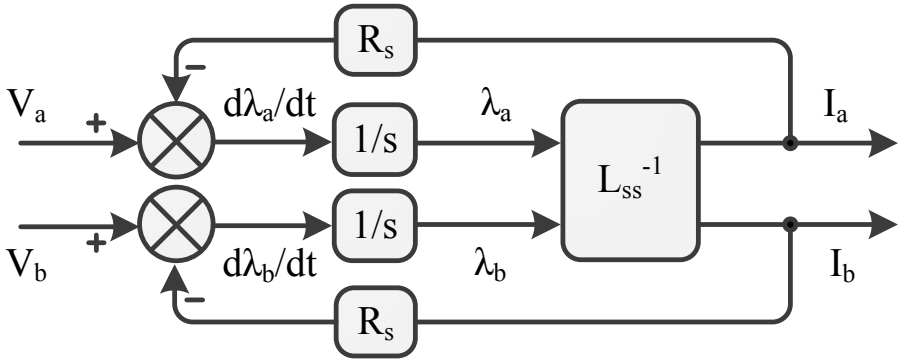

Fig. 4.9 Electric model block diagram.

Furthermore, the electromagnetic torque is written as:

$$T_{em} = \frac{1}{2} p I_s^t \frac{\partial L_{ss}}{\partial \theta_e} I_s = \frac{1}{2} p \begin{bmatrix} I_a & I_b \end{bmatrix} \begin{bmatrix} \partial L_{aa}/\partial\theta_e & \partial L_{ab}/\partial\theta_e \\ \partial L_{ab}/\partial\theta_e & \partial L_{bb}/\partial\theta_e \end{bmatrix} \begin{bmatrix} I_a \\ I_b \end{bmatrix} \tag{4.42}$$

The mechanical model's equations does not change from an m-phase to a 2-phase machine and the equation is rewritten as:

$$T_{em} - T_{load} = J.\frac{d\Omega_{mec}}{dt} + f_v \Omega_{mec} \tag{4.43}$$

Now that the diverse equations that describe the machine behaviour are shown, the system block diagram can be represented as in figure 4.10. Consequently, the power electronics that feed the machine have to be introduced to the model to fully simulate the controlled machine performance. The next paragraph will detail the power electronics model.

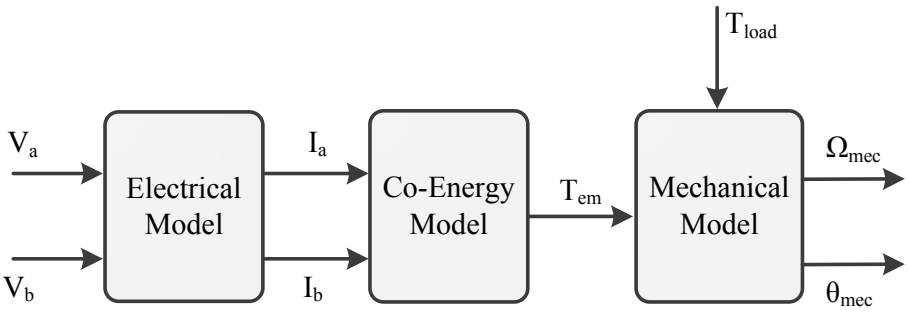

Fig. 4.10 Machine model block diagram.

4.4.3 Power Electronics

The power electronics module converts the input DC voltage into an AC voltage in order to feed the machine. The power electronics - machine connection is shown in figure 4.11 for a 2-phase machine. Two H-Bridge converters are connected to the machine, each feeding one phase. Moreover, the controller imposes complementary states on the two legs of one H-bridge. In other terms, when the upper switch of the first leg is in the ON state the upper switch of the second leg is in the OFF state. For the complete model, the lag time on the switching of the power electronics is neglected. Consequently, the voltage equations in function of the switch states are written as the following:

$$\begin{aligned} V_a &= (2u_a - 1).V_{DC} \\ V_b &= (2u_b - 1).V_{DC} \end{aligned} \tag{4.44}$$

where V_{DC} is the DC input voltage and u_a and u_b are the state of the first switch of the first leg of each H-bridge. Furhthermore, $\{u_a, u_b\} \in \{0, 1\}^2$ where 0 represents the OFF state and 1 represents the ON state of the switches.

4.4.4 Implementation of the Model on Matlab/Simulink

The model developed previously is implemented on Matlab/Simulink to test the current control loop afterwards. The complete model's implementation on Simulink is shown on figure 4.12. The model is made up of the reference generator that generates the signals of the two phase currents with the fundamental and their harmonics. The controller block is to introduce the phase current control loop for the current in the SynRM to follow the reference current. The PWM block takes the controller outputs

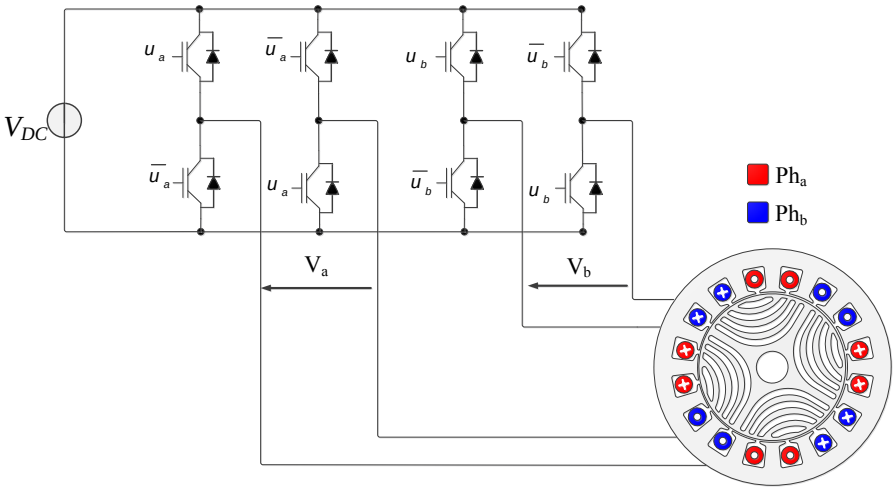

Fig. 4.11 Interconnection between the power electronics and the machine.

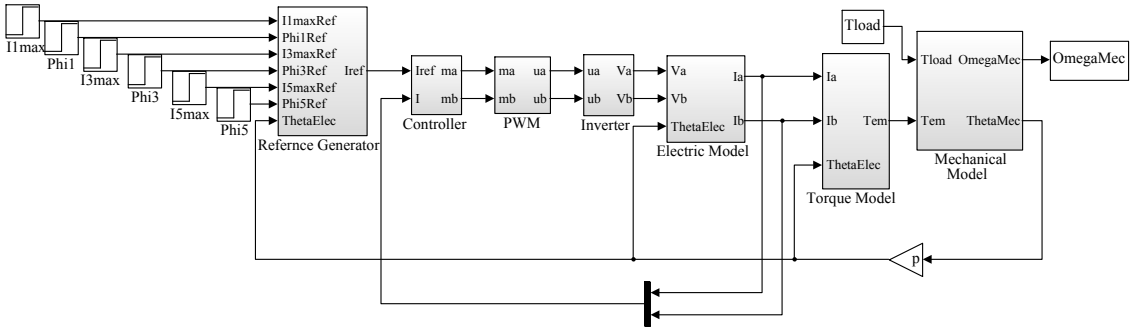

Fig. 4.12 Model of the SynRM and the controller implemented on Matlab/Simulink.

(m_a and m_b) as an input and, with the use of the PWM carrier signal it generates the power electronics switch states (u_a, u_b). The inverter transforms the switch states into voltages across the machine windings. The electric model represents the machine windings and describe the current evolution of the machine with respect to the input voltages (refer to figure 4.9). This model requires the form and values of the inductances and their variation with the machine angular position. The torque model describes the generated torque of the SynRM for the given two phase currents as an input, and the mechanical model describes the angular speed and position of the machine. The angular position (ThetaMec on figure 4.12) is used by the reference generator to generate the reference currents since the required current values depend on the rotor position. The angular position is also used by the electric model and the torque model since the inductance values depend on this position.

Concerning the inductance matrices that are used by both the electric and the torque models, the values are determined by FE simulations. In other terms, an FE simulation is performed on the nominal operation point, and the inductance forms are retrieved. A Fourier series is performed on the self and the mutual inductances, and the values are grouped by 2×2 matrices (A_{2n}) and B_{2n} as the following:

$$\begin{aligned} L_{ss} &= \begin{bmatrix} L_{aa} & L_{ab} \\ L_{ab} & L_{bb} \end{bmatrix} \\ &= A_0 + A_2 cos(2\theta_e) + B_2 sin(2\theta_e) + A_4 cos(4\theta_e) + B_4 sin(4\theta_e) \\ &\quad + A_6 cos(6\theta_e) + B_6 sin(6\theta_e) + A_8 cos(8\theta_e) + B_8 sin(8\theta_e) \\ &\quad + A_{10} cos(10\theta_e) + B_{10} sin(10\theta_e) \end{aligned} \tag{4.45}$$

For the electric model, the inverse of the inductance matrix (L_{ss}^{-1}) is needed (refer to figure 4.9). Therefore, at each iteration a numerical matrix inversion is performed when L_{ss} is determined after acquiring the electrical displacement (θ_e) value. On the other hand, the torque model needs the derivative of the inductances with respect to θ_e (refer to equation (4.42)). Therefore, the following equation is used in the torque model:

$$\begin{aligned} \frac{\partial L_{ss}}{\partial \theta_e} &= -2A_2 sin(2\theta_e) + 2B_2 cos(2\theta_e) - 4A_4 sin(4\theta_e) + 4B_4 cos(4\theta_e) \\ &\quad - 6A_6 sin(6\theta_e) + 6B_6 cos(6\theta_e) - 8A_8 sin(8\theta_e) + 8B_8 cos(8\theta_e) \\ &\quad - 10A_{10} sin(10\theta_e) + 10B_{10} cos(10\theta_e) \end{aligned} \tag{4.46}$$

4.4.5 Controller Synthesis

The block diagram of the SynRM electric model, the inverter model, the modulator model with the controller is shown in figure 4.13. The used controller is a discrete RS controller with one integral action in the denominator and is written as follows:

$$\frac{R(z^{-1})}{S(z^{-1})} = \frac{r_0 + r_1 z^{-1} + r_2 z^{-2}}{(1 + s_1 z^{-1})(1 - z^{-1})} \tag{4.47}$$

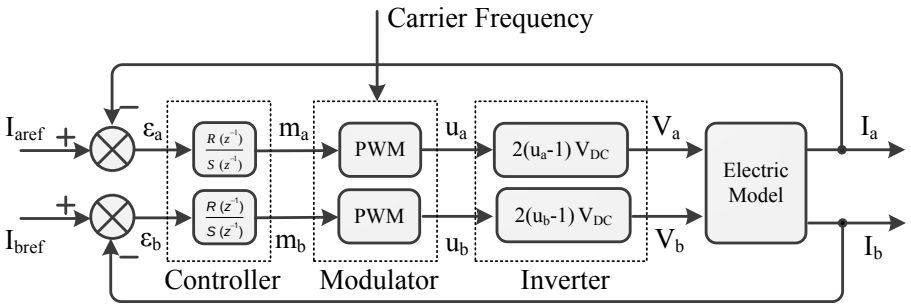

Fig. 4.13 Block diagram of the current controlled machine.

The current controller will be synthesized and tested for the fundamental frequency and for the 3^{rd} and 5^{th} harmonics. Therefore, the reference currents in the (ab) reference are written as follows:

$$\begin{aligned} I_{aref} &= I_1 cos(\omega_e t + \phi_1) + I_3 cos(3\omega_e t + \phi_3) + I_5 cos(5\omega_e t + \phi_5) \\ I_{bref} &= I_1 cos(\omega_e t + \phi_1 - \pi/2) + I_3 cos(3(\omega_e t - \pi/2) + \phi_3) + I_5 cos(5(\omega_e t - \pi/2) + \phi_5) \end{aligned} \tag{4.48}$$

4.4.5.1 Simplified Model for the Controller Coefficient Definition

This part will deal with phase a. However, the same equations are applicable to phase b. The equation that describes the electrical voltage in phase a can be derived from equations (4.37 - 4.41) and can be written as the following:

$$V_a = r_s I_a + L_{aa}\frac{dI_a}{dt} + \omega_e \frac{dL_{aa}}{d\theta_e} I_a + L_{ab}\frac{dI_b}{dt} + \omega_e \frac{dL_{ab}}{d\theta_e} I_b \tag{4.49}$$

As can be seen from equation 4.49, the studied system is a non-linear system from a control theory point of view. In addition, the coefficients of the controller in equation (4.47) are non-adaptive and therefore constant. In this regard, the model has to be linearised around an inductance value and some values have to be neglected. The system will be linearised around an inductance L_0, and is written as follows:

$$V_a = \overbrace{r_s I_a + L_0 \frac{dI_a}{dt}}^{\text{Simplified Model}} + \overbrace{(L_{aa} - L_0)\frac{dI_a}{dt} + \omega_e \frac{dL_{aa}}{d\theta_e} I_a + L_{ab}\frac{dI_b}{dt} + \omega_e \frac{dL_{ab}}{d\theta_e} I_b}^{\text{Non-Linear Terms}} \tag{4.50}$$

The simplified model will be used to determine the controller coefficients. However, the impact of the non-linear terms cannot be considered as negligible since $\frac{dI_a}{dt}$, $\frac{dI_b}{dt}$ and I_b have the same order of magnitude as I_a. Therefore, a model observer will be introduced and studied to estimate these terms later in the chapter. First, the simplified model will be expressed in the discrete domain to be able to determine the controller coefficients.

Taking into account the mean value of the PWM only, the overall simplified system is considered as:

$$m_a V_{DC} =< V_a >= r_s I_a + L_0 \frac{dI_a}{dt} \tag{4.51}$$

where $m_a \in [-1, 1]$, is the controller output and can be represented as the following:

$$m_a =< 2u_a - 1 > \tag{4.52}$$

The simplified model with a time delay of the numerical system is represented in the discrete domain in equation (4.53) with the polynomial representation. A delay is introduced in the model since when the controller calculation is done, the controller output is sent in the next sampling period.

$$\begin{aligned} \frac{I_a(z^{-1})}{m_a(z^{-1})} = T(z^{-1}) = \frac{B(z^{-1})}{A(z^{-1})} = z^{-1}\frac{b_1 z^{-1}}{1 + a_1 z^{-1}} \\ a_1 = -e^{-\frac{T_s r_s}{L_0}} \\ b_1 = \frac{V_{DC}}{r_s}(1 - e^{-\frac{T_s r_s}{L_0}}) \end{aligned} \tag{4.53}$$

where T_s is the sampling period for the controller.

4.4.5.2 Definition of a 4^{th} Order RS Controller

In [108], it has been shown that for direct current current control the 4^{th} order RS controller gives better results in comparison to the 2^{nd} order RS controller. The RS controller has been chosen since it is one of the simplest to implement in the discrete domain.

The controller form is shown in equation (4.47) where $R(z^{-1})$ and $S(z^{-1})$ are the controller numerator and denominator respectively. In order to impose a system

dynamic in the case of an RS controller, the procedure followed is to solve the following equation:

$$A(z^{-1})S(z^{-1}) + B(z^{-1})R(z^{-1}) = P(z^{-1}) \tag{4.54}$$

where $B(z^{-1})$ and $A(z^{-1})$ are the system model's numerator and denominator respectively in the discrete domain. $P(z^{-1})$ is the dynamics equation of the system and can be written as follows since a 4^{th} order system is desired:

$$P(z^{-1}) = (1 - e^{-2\pi F_{bw} T_s} z^{-1})^4 = (1 + p_1 z^{-1})^4 \tag{4.55}$$

where F_{bw} is the bandwidth frequency of the system in closed loop.

Resolving equations 4.54 and 4.55, the expression of the controller coefficients are obtained as in the following equations:

$$\begin{aligned} s_1 &= 4p_1 - a_1 + 1 \\ r_0 &= \frac{6p_1^2 + s_1(1 - a_1) + a_1}{b_1} \\ r_1 &= \frac{-4p_1^2 + s_1 a_1}{b_1} \\ r_2 &= \frac{p_1^4}{b_1} \end{aligned} \tag{4.56}$$

4.4.5.3 Closed Loop Bandwidth Frequency F_{bw}

In order to define the controller coefficients s_1, r_0, r_1 and r_2, the closed loop bandwidth frequency (F_{bw}) should be first determined. F_{bw} should be respect two constraints in system control theory for an acceptable control performance:

- F_{bw} should be greater than 1/2 decade ($\times$ 3.16) with respect to the maximal controlled electric frequency in the system.
- The PWM carrier frequency (F_{car}) should be greater than 1/2 decade with respect to F_{bw}.

Figure 4.14 shows the difference system frequencies, the desired system performance in closed loop, and the frequency limitations. F_{emax} and F_s are the phase current maximal fundamental frequency and the sampling frequency respectively. In the studied case, the PWM carrier frequency is the same as the sampling frequency ($F_{car} = F_s$).

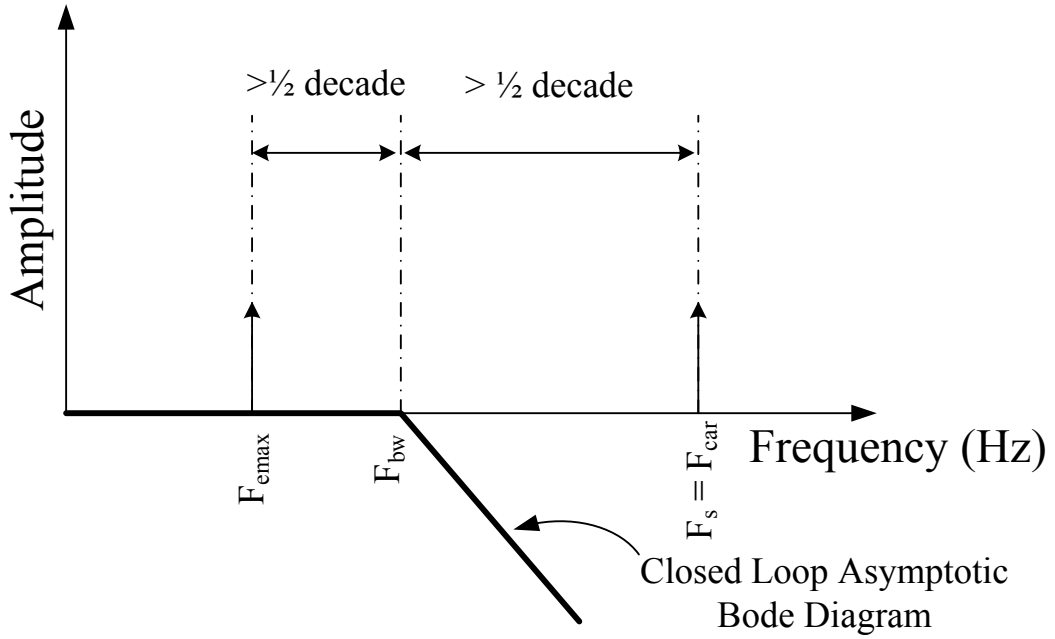

Fig. 4.14 Asymptotic bode diagram with the different system frequencies and conditions.

In other terms, the controller calculates its output at every PWM period. The carrier frequency is fixed at $10kHz$ in the studied case.

In this part, the only current component is the current fundamental frequency, knowing that when the harmonics are introduced, either F_{bw} should be increased or the maximal machine speed should be reduced to be able to control the current harmonics. The currents harmonics control will be later presented in this chapter.

The maximal rotation speed of the machine is of 7000 rpm (refer to figure 2.19) which corresponds to $p.7000/60 = 233Hz$ of current fundamental frequency. F_{bw} will be chosen at $2000Hz$, a frequency that respect both constraints shown on figure 4.14.

4.4.5.4 Model Observer for the Non-Linear Terms

The non-linear terms in equation (4.50) are not used for the controller definition. However, it is not yet proven that they are negligible in the control system performance. Figure 4.15 shows a case where the phase current is controlled (complete model current) and compared it to the simplified model current. Both currents have the same fundamental frequency but different amplitudes. The difference as seen in the figure is not negligible and is comparable to the complete model current in amplitude.

A model observer is studied in order to estimate the Non-Linear Terms (NT). The structure of the observer is shown on figure 4.16. The model observer estimates the

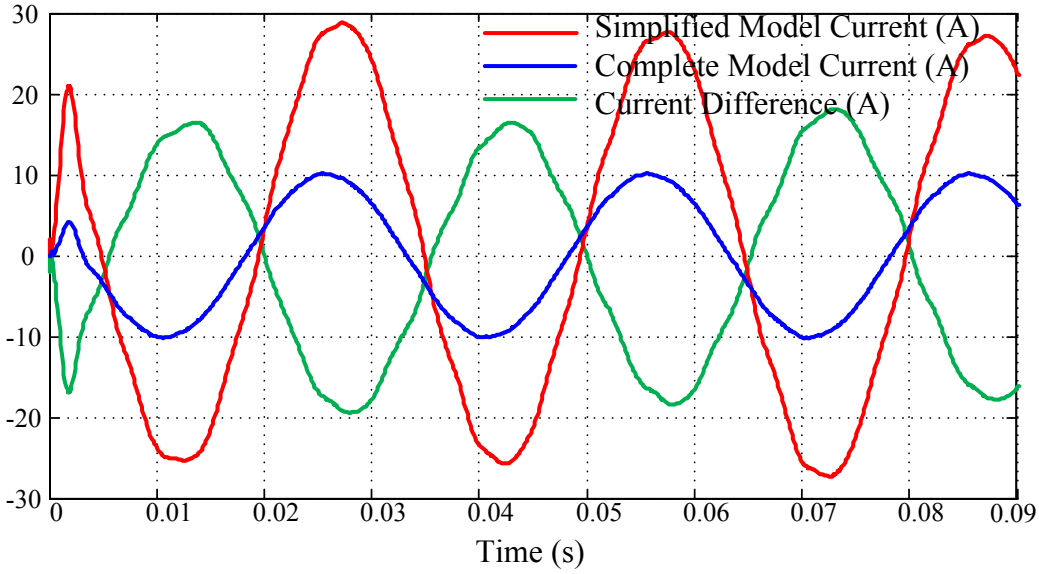

Fig. 4.15 Currents from the complete model, the simplified model and their difference in a current controlled case with $I_{ref} = 10A$.

control variation (Δm) that is required to compensate for the model simplification. I_{amod} is acquired by using the simplified model and m_a, and is compared to the complete model current (I_a). An R_oS_o observer is introduced afterwards in order to estimate $\frac{NT}{V_{DC}}$ (the control image of the non-linear voltage terms). A filter is introduced in order to control which frequencies to introduce to the control system. A dynamic observer is used with a bandwidth frequency (F_{obs}) of 4000 Hz. This allows to have an observation error (ϵ_{mod}) as low as possible (nearly zero). The bandwidth is limited by the PWM frequency since the observer should eliminate the frequencies introduced by the PWM carrier or else the observer will become unstable. The observer contains one integral function, and its equation is the following:

$$\frac{R_o(z^{-1})}{S_o(z^{-1})} = \frac{ro_0 + ro_1 z^{-1} + ro_2 z^{-2}}{(1 + so_1 z^{-1})(1 - z^{-1})} \tag{4.57}$$

Figure 4.17 shows a comparison between the current difference of the complete and simplified models and the current image of Δm. The current image of Δm is obtained by multiplying Δm by the simplified model ($T(z^{-1})$). The comparison shows that the estimation is satisfactory and the current control is tested next with and without the model observer.

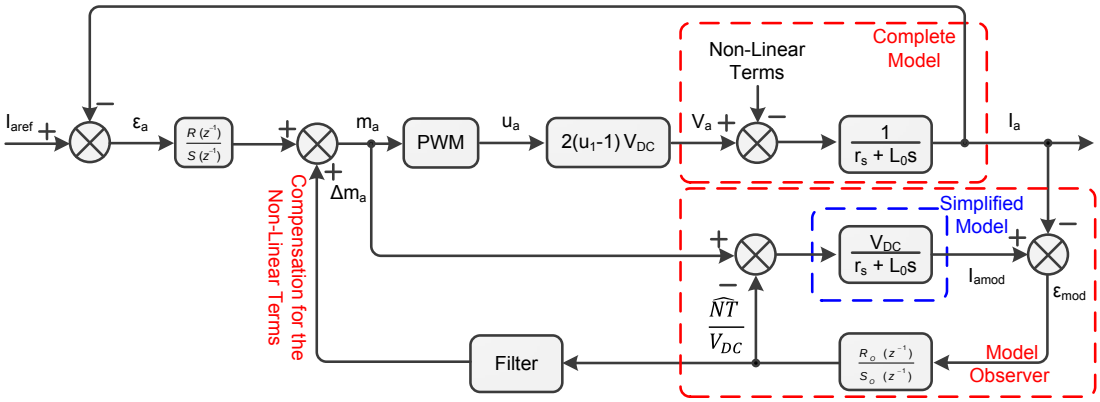

Fig. 4.16 SynRM current control system for phase a with the model observer of the Non-Linear Terms (NT).

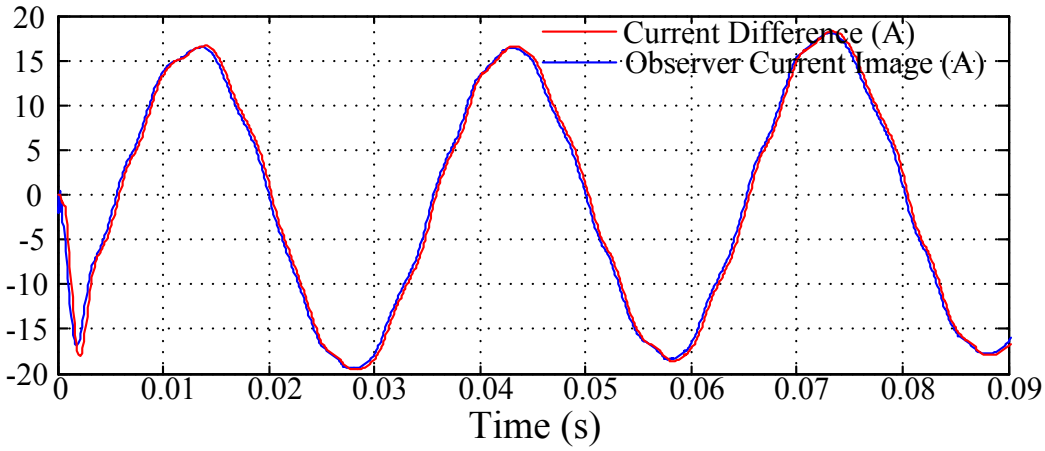

Fig. 4.17 Current difference of the complete and simplified models and the current image of the observed NT for $I_{ref} = 10A$ and $\Omega_{mec} = 1000rpm$.

The control system parameters used for the current control are shown in table 4.2. L_0 is chosen to be 30 mH for the comparison. This value does not affect greatly the control performance (refer to the next subsection 4.4.5.5). In order to evaluate the observer and the controller performance, the maximum error between the current reference and the current (er_{max}) is used. Moreover, 4 operation points are tested:

1. low speed - low load operation point ($\Omega_{mec} = 1000rpm - I_1 = 5A$),
2. low speed - high load operation point ($\Omega_{mec} = 1000rpm - I_1 = 10A$),
3. nominal speed - low load operation point ($\Omega_{mec} = 3500rpm - I_1 = 5A$),
4. nominal speed - high load operation point ($\Omega_{mec} = 3500rpm - I_1 = 10A$).

Parameter	Symbol	Value	Unit
Pole Pairs Number	p	2	–
Nominal Mechanical Speed	Ω_{nom}	3500	rpm
Maximal Mechanical Speed	Ω_{max}	7000	rpm
Phase Resistance	r_s	0.49	Ω
Model Inductance	L_0	30	mH
DC Voltage	V_{DC}	200	V
Closed Loop Bandwidth Freq	F_{BW}	2000	Hz
Sampling Time	T_s	0.0001	s
Controller Coefficient 1	r_0	1.81	–
Controller Coefficient 2	r_1	−1.43	–
Controller Coefficient 3	r_2	0.01	–
Controller Coefficient 4	s_1	0.86	–

Table 4.2 Control system parameters.

Simulation results are shown for these 4 operation points on figure 4.18 using the the 4^{th} order RS controller without the NT observer, and on figure 4.19 with the NT observer. The simulation results show a very good control of the current at 100 rpm for both load points for both cases. The case of 3000 rpm shows a slight current overshoot on the current maximal value that remains acceptable (1.3 A for the case without the observer and 1 A for the case with the observer).

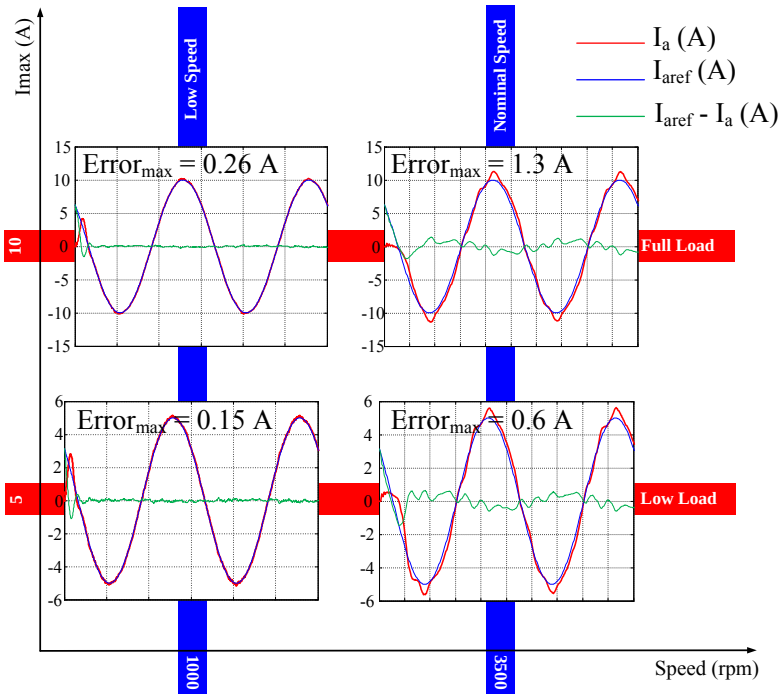

Fig. 4.18 Simulation results using Matlab/Simulink for the 4^{th} order RS controller without model observer for four operating points.

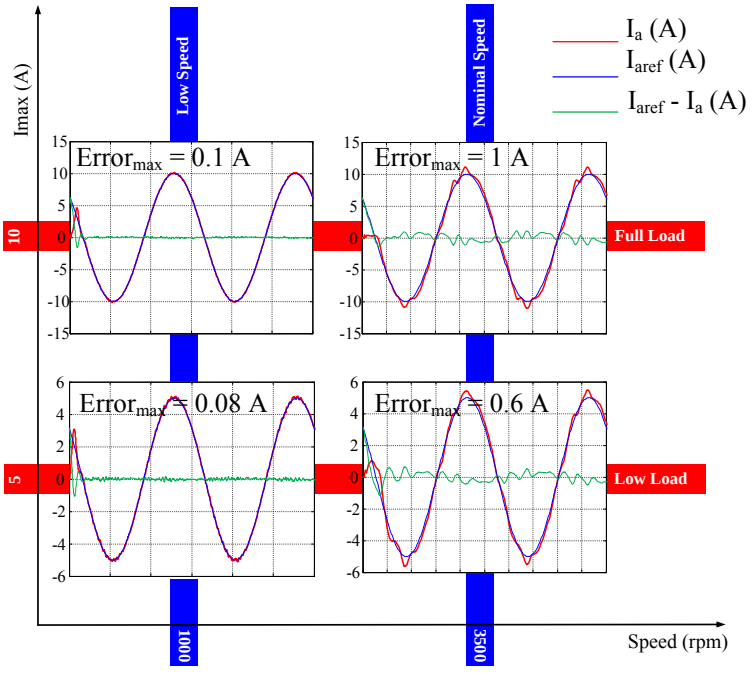

Fig. 4.19 Simulation results using Matlab/Simulink for the 4^{th} order RS controller including the model observer for four operating points.

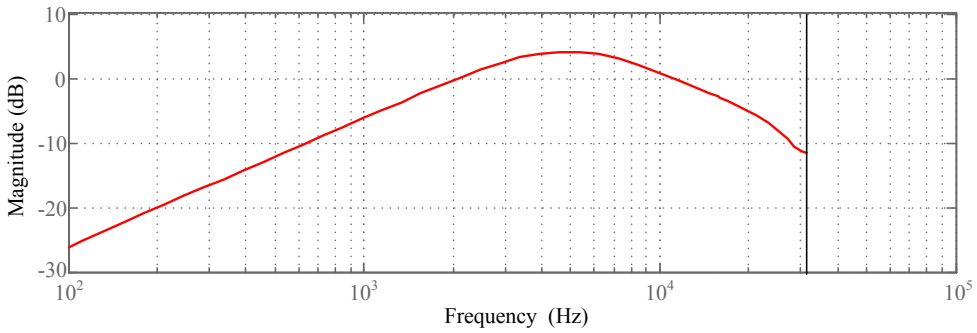

Fig. 4.20 Bode diagram of the transfer function between the non-linear terms and the output current with the presence of the current controller in a closed loop.

The introduction of the observer does not show a significant improvement for the reason that the control is already satisfactory. Figure 4.20 shows the bode diagram of the transfer function $\frac{I_a(z^{-1})}{NI(z^{-1})}$ when the controller is present and the system is closed loop. Equation (4.50) that the maximal fundamental frequency of NT is of $3\omega_e$ since L_{ij} have a fundamental frequency of $2\omega_e$ and the phase currents of ω_e. Therefore, the maximal frequency is for $\Omega_{max} = 7000rpm$, and the corresponding $3\omega_e$ is 700 Hz. The magnitude of the bode function on this frequency is $-10dB$ which reduces this maximal frequency perturbation by 66 %.

4.4.5.5 Choice of L_0

L_0 is the linearisation inductance value to simplify the model for the controller determination. In order to evaluate the impact of its value on regulation the Total Harmonic Distortion (THD) will be used. The THD shows the ratio of the harmonic content of the signal with respect to its fundamental value ans is expressed as the following:

$$THD = \frac{\sum I^2_{harmonics}}{I^2_{fundamental}} \tag{4.58}$$

Figure 4.21 shows the variation of the THD versus the value of L_0. For L_0 values between $10mH$ and $43mH$, the THD is below 0.05%. These limit values correspond to approximately the $max(L_{aa})$ and $min(L_{aa})$ values of the machine. Therefore, values in $[in(L_{aa})\ max(L_{aa})]$ deliver acceptable control performance. This is the case on the whole speed range.

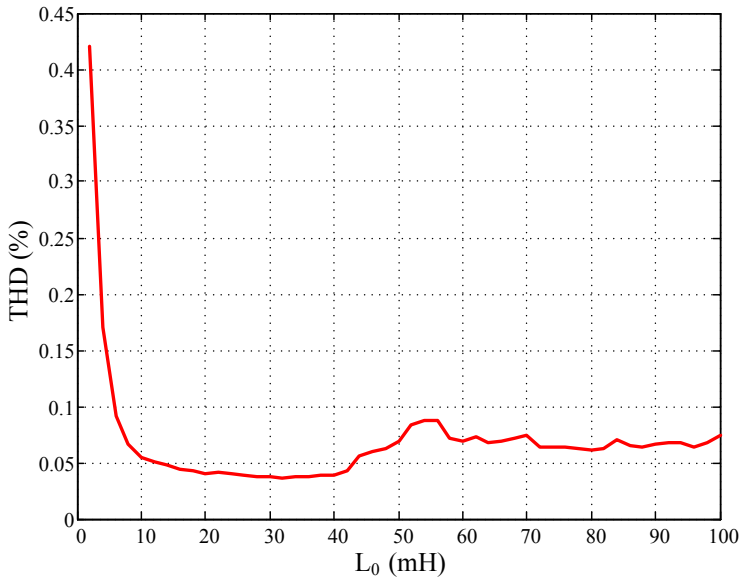

Fig. 4.21 THD vs model inductance (L_0) for low speed full load operation point ($\Omega_{mec} = 1200rpm - I_1 = 10A - \phi_1 = 51°$) from Matlab/Simulink simulations.

4.4.5.6 Controller for Harmonics Injection

The injection of current harmonics adds an extra constraint on the closed loop bandwidth. The system in closed loop with the controller should be able to inject the current harmonics in the system. However, the maximum injected frequency is limited by the PWM carrier frequency (F_{car}). Figure 4.22 shows the different system frequencies, the desired system performance in closed loop, and the frequency limitations in the case of harmonics injection. In the studied case, the PWM carrier frequency is the same as the sampling frequency ($F_{car} = F_s$). In other terms, the controller calculates its output at every PWM period. F_{bw} should respect a 1/2 decade limitation with respect to F_{car} or else the carrier frequency will affect the system regulation in closed loop. In addition, the maximum controller frequency ($5F_e$ for 5^{th} harmonic injection) should be at least 1/2 decade less than the F_{bw}. Hence, since the carrier frequency is fixed at $10kHz$, the maximal current fundamental frequency is $60Hz$ which corresponds to a machine speed of $1800rpm$. A margin will be kept and the maximal operating speed (Ω_{max}) will be chosen at $1500rpm$.

This is chosen mainly to be able to evaluate the current harmonics injection in the three operating zones of the SynRM (refer to 1.2.4). However, in an industrial system where the maximum speed cannot be reduced the harmonics injection can be limited to speeds below the nominal speed. Another solution is to increase the PWM carrier

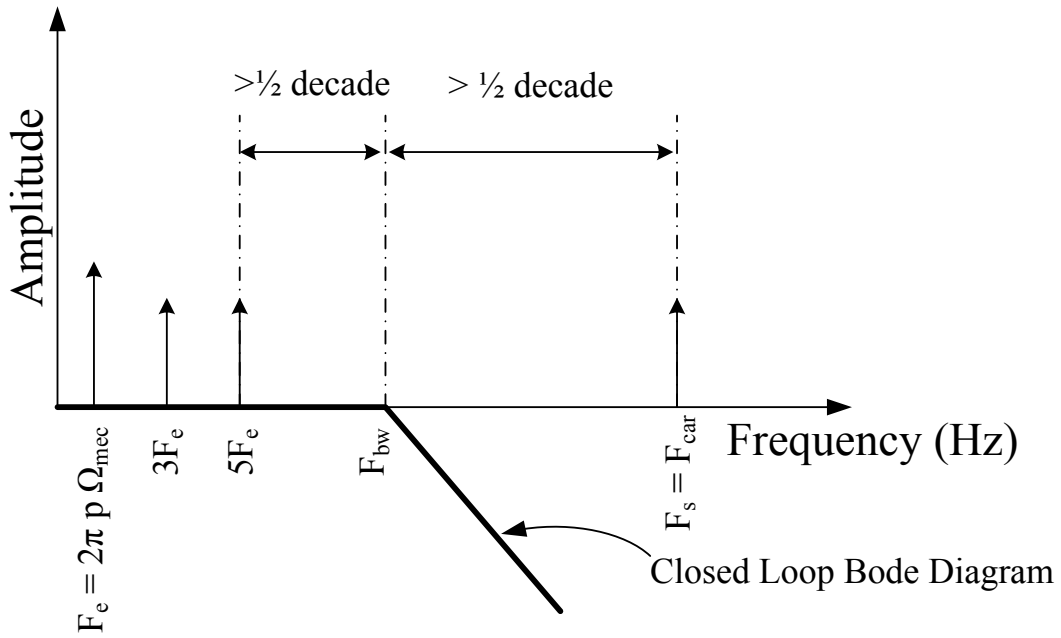

Fig. 4.22 Asymptotic bode diagram with the different system frequencies and conditions for 3^{rd} and 5^{th} harmonics injection.

frequency. However, higher PWM frequencies leads to the increase of the commutation losses in the conventional power electronics.

In order to be able to operate in the three operation zones, the DC voltage should be limited. For $V_{DC} = 30V$ the performance envelope on figure 4.23 is obtained with the corresponding fundamental current amplitude and phase angle up to $1500rpm$.

From a control point of view, two limits exist in the system: the voltage limit and the bandwidth limit. The voltage limit is introduced by a saturation on the control output variables m_a and m_b. This limit defines the torque limits in operation zones 2 and 3 (refer to section 1.2.4). Therefore, in these two zones, the variation of m_a and m_b is approximately between -1 and 1. This can be seen in figure 4.24 for the maximal speed operation point.

On the other hand, the bandwidth limit determines the maximal frequency after which the controller cannot follow the reference imposed. This limit determines whether a current harmonic can be injected or not in the system. In the studied case, the 5^{th} harmonic is the greatest harmonic injected in the system. In this regard, at the maximal speed of $1500rpm$ the fundamental is at $50Hz$ since $p = 2$ and the 5^{th} harmonic is at $250Hz$. The bandwidth of the system in closed loop is $1500Hz$ and is 6 times greater (0.778 decade) than the maximal 5^{th} harmonic frequency. It is known in control theory

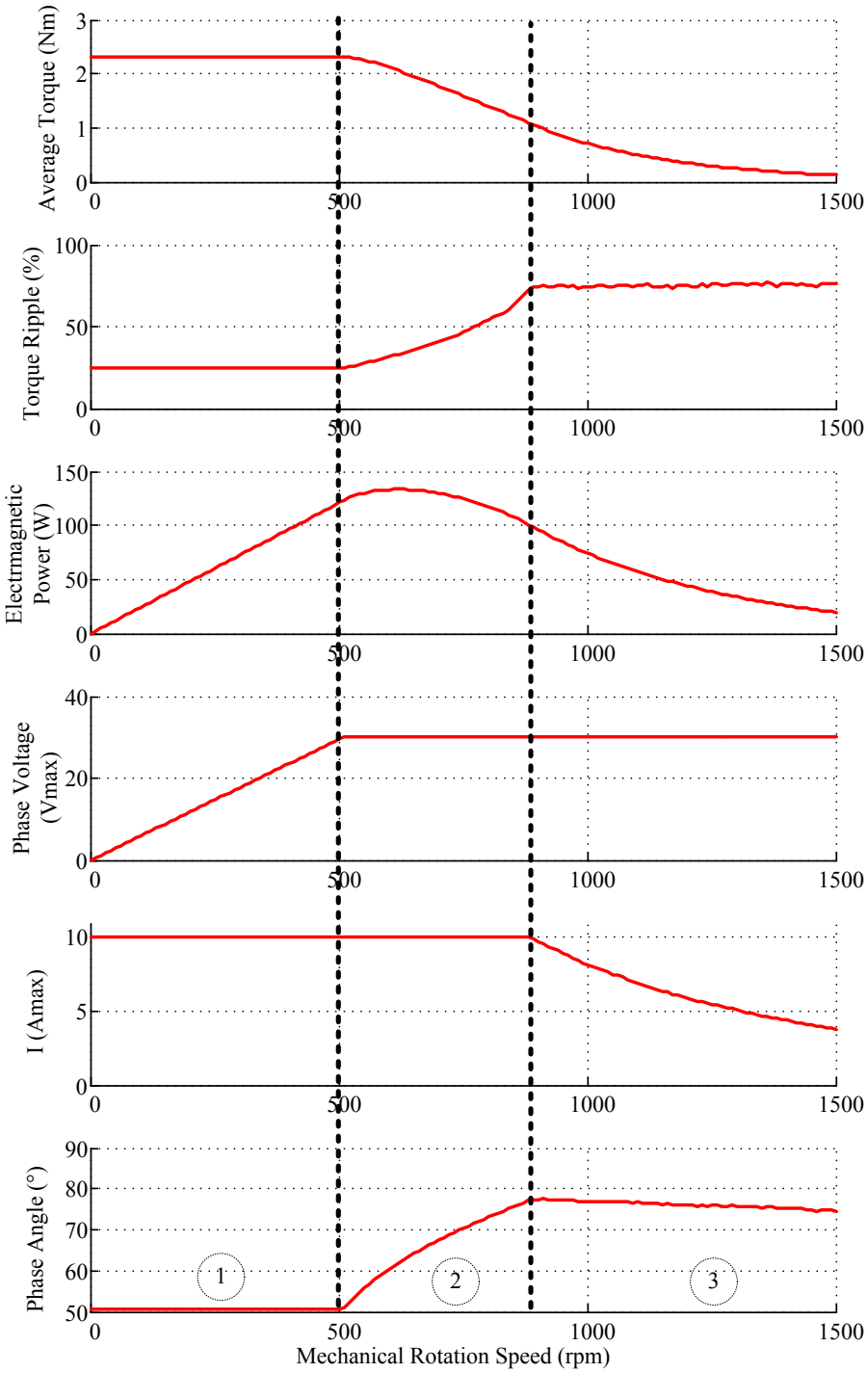

Fig. 4.23 Performance envelope with the corresponding current and phase angle for $V_{DC} = 30V$ up till $1500rpm$ using FE simulations.

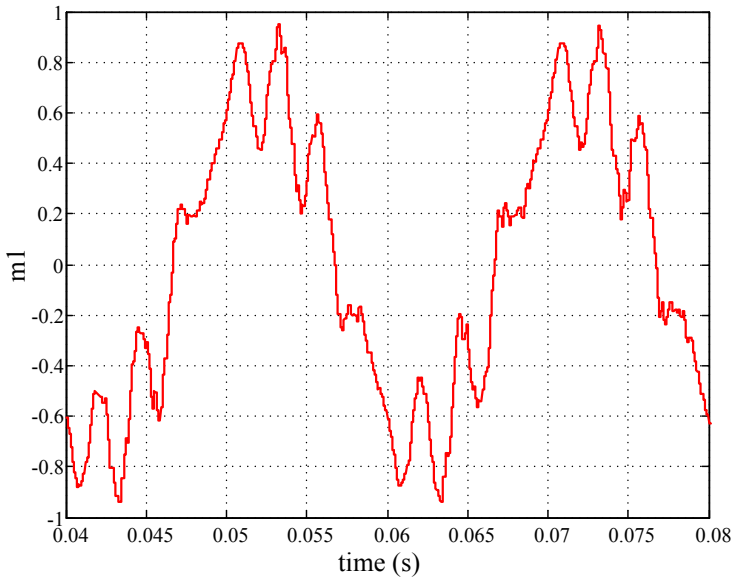

Fig. 4.24 Control output m_1 for maximal speed operation point($\Omega_{mec} = 1500rpm - I_1 = 3.75A - \phi_1 = 75°$) from Matlab/Simulink simulations.

that a bandwidth of more than 0.5 decade greater than the maximal injected frequency is acceptable. Figure 4.25 shows the current control for the maximal operation speed and harmonic injection with $I_3 = I_5 = 10\%I_1$. A good control is observed and figure 4.26 shows that there is no saturation in the control. This proves that the chosen bandwidth is adapted for the application. However, there is always a voltage limitation that limit the quantity of the harmonic injection that should be observed on the test bench.

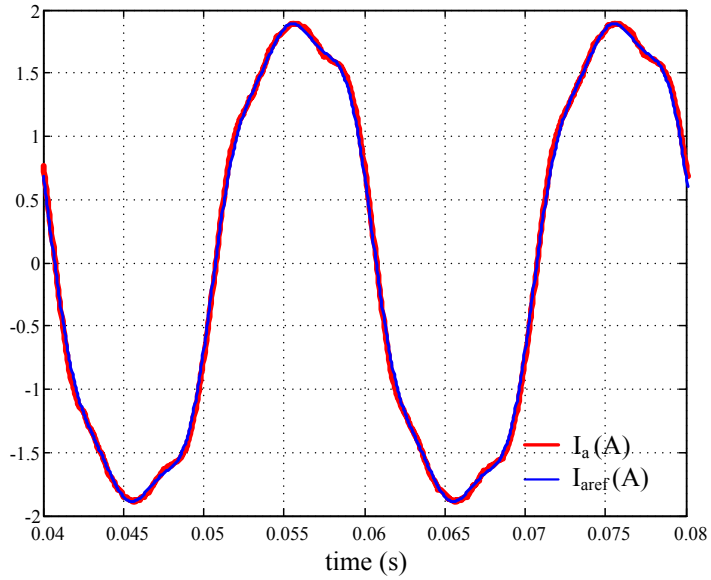

Fig. 4.25 Phase a current control with the 4^{th} order RS Controller for $\Omega_{mec} = 1500rpm - I_1 = 2A - \phi_1 = 51° - I_3 = 0.2A - \phi_3 = 0° - I_5 = 0.2A - \phi_5 = 90°$ from Matlab/Simulink simulations.

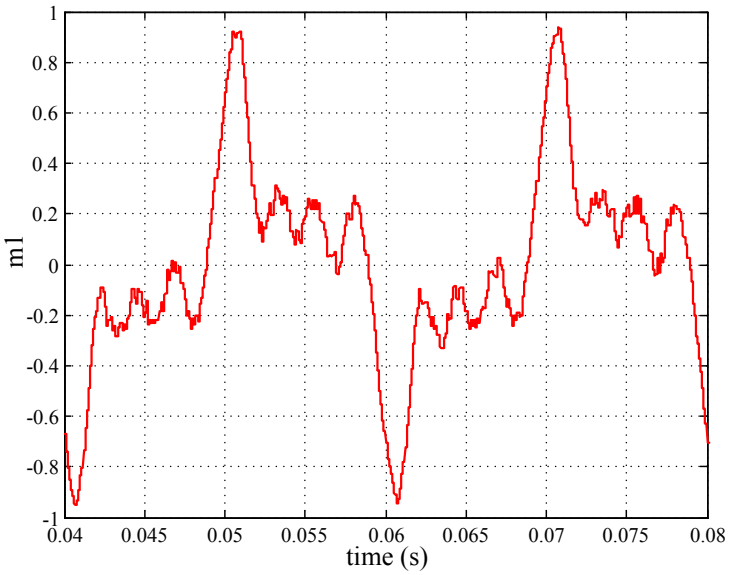

Fig. 4.26 Controller output m_1 for $\Omega_{mec} = 1500rpm - I_1 = 2A - \phi_1 = 51° - I_3 = 0.2A - \phi_3 = 0° - I_5 = 0.2A - \phi_5 = 90°$ from Matlab/Simulink simulations.

Chapter Conclusion

This chapter presents the phase current harmonics injection and its impact on the SynRM performance. First, the electromagnetic model of a m-phase SynRM is developed and the interaction between the current time harmonics and the inductance space harmonics is formalized. It has been shown that there exists two non-zero average torque generating mechanisms: the proper influence of each current harmonic and the interaction between the different current harmonics. Later, current harmonics injection was formulated for a general 2-phase SynRM and was applied to the machine design developed in Chapter 2. It has been observed that at a constant rms current value, the average torque does not increase even with current harmonics injection. However, there exists a locus where the 3^{rd} and the 5^{th} harmonics should be injected simultaneously and where $I_3 = I_5$ that does not theoretically decrease the torque. It has been found out with the help of an optimization algorithm that on this locus the torque ripple decreases significantly.

The second part of this chapter discusses the phase current control of the SynRM. Firstly, the control reference is chosen to be the (ab) reference since park's (dq) reference is not beneficial in this case. Secondly, the models of the 2-phase SynRM and the power electronics are established to be able to synthesize the controller. A first controller is proposed for the case to reach 7000 rpm with the current fundamental only. An 4^{th} order RS controller is used, and the controller coefficients are calculated based on a simplified linearised model. An observer is set up and tested to estimate the non-linear terms of the model. This observer gave slightly better results in control. However, it is moderately beneficial since the introduced controller rejects signal variations in the frequency domain of the non-linear terms. The inductance around which the model is linearised is then studied and the case of one operation point is discussed later in this chapter. A second control study is carried out for current harmonics control. Since the PWM carrier frequency is fixed, the speed of the machine should be limited to be able to inject harmonics on the whole speed zone. Therefore, the machine speed is limited to $1500rpm$ and V_{DC} to $30V$ to be able to inject the 3^{rd} and the 5^{th} current harmonics on the whole speed range. Finally, the second controller is tested and the case of the maximal rotation speed with harmonics injection is shown.

Chapter 5

Experimental Validation

Contents

This chapter validates experimentally the analytical design procedure developed in chapter 2, the design optimization study presented in chapter 3 and the current harmonics injection developed in chapter 4.

5.1 SynRM Prototype and Test Bench

5.1.1 Test Bench Description

The different components of the test bench are presented on figures 5.1, 5.2 and 5.3. The controller is implemented on a DSpace module where two cards are used: the DS2004 and the DS5101. The DS2004 is used to acquire the data, and the DS5101 is used to generate the PWM. In order to set the system speed, a speed controlled MAGTROL hysteresis brake (Model HD-710) is used. The MAGTROL provides the instantaneous torque as an analogue output received by DS2004 to visualize the torque and to be able to calculate T_{avg} and T_{ripple}.

Two types of sensors are used on the test bench: the angular position sensor and the phase current sensors. The angular position sensor is a synchro-resolver (LTN model RE-15-1-B24). The sensor output is read by DS2004 and converted to acquire the machine angular position. On the other hand, the current sensors are hall effect sensors (LEM LTS 6NP) that send a voltage image of the currents to the DS2004 as well.

The DC voltage is supplied by a 3-phase Graetz bridge rectifier (Model: LANGLOIS Compak40) that can deliver up to $4kW$. The output DC voltage is regulated by an autotransformer and a capacitor ($3300\mu F - 350V$) is put in parallel to insure the current reversibility of the test bench (for motor and brake operations).

For the power electronics, 2 H-bridge modules are used to feed the 2 SynRM phases. The H-bridges use IGBT transistors supplied by Fuji Electric (Model 2MBI 100N-60), and the drivers are supplied by ARCEL (Model ARCAL 2106). The ON/OFF state of the power electronics modules is controlled by the DS5101 of DSpace.

The power of the two phases as well as the power delivered by the DC source are measured by a 4-channel power meter supplied by ZES Zimmer Electronic Systems (Model LMG450).

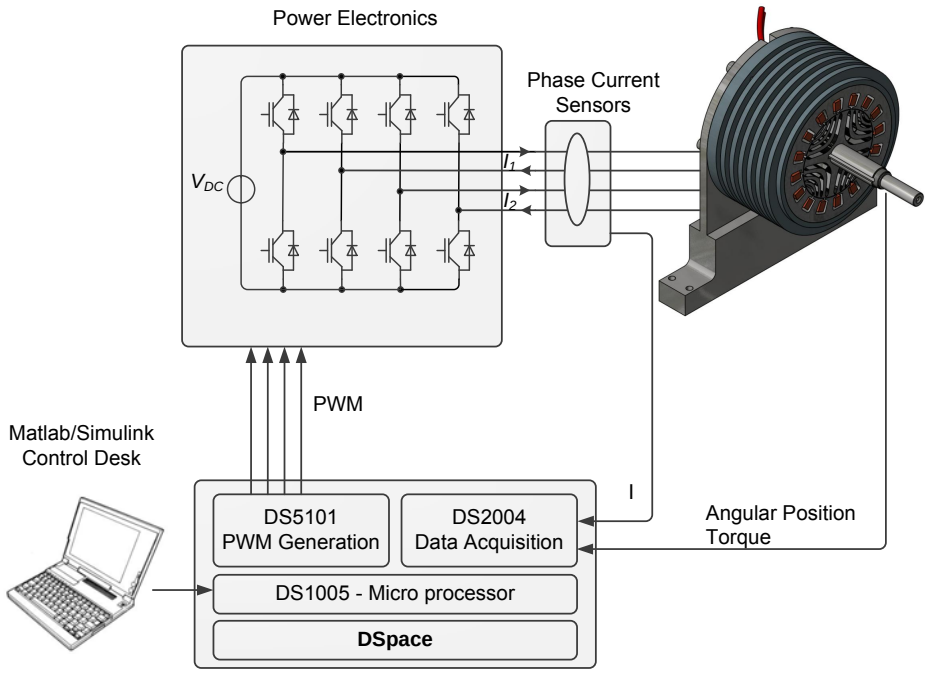

Fig. 5.1 Components of the developed test bench; DSpace is used for the implementing current controller, reading the mechanical and electrical variables an generating the PWM signals; 2 H-bridge converters are used for the power electronics.

Fig. 5.2 Laminations and the different constituents of the initial SynRM design prototype, M330-35A laminations are used for the prototype.

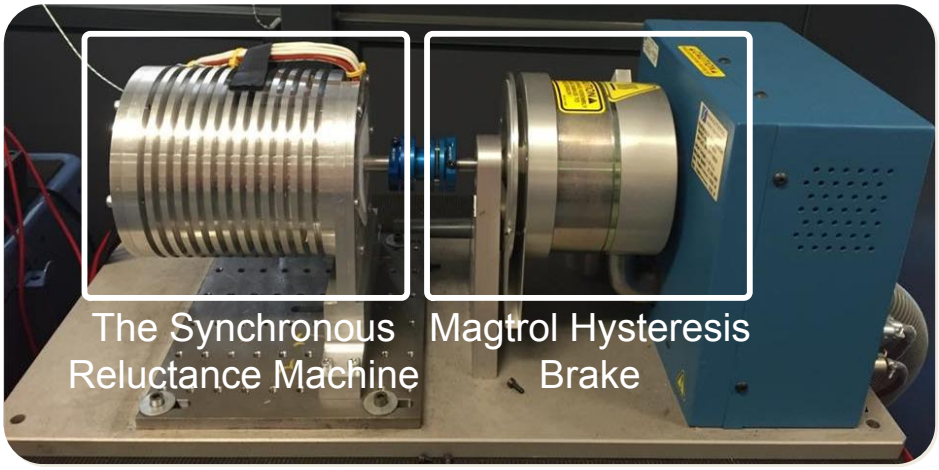

Fig. 5.3 Machine Prototype and the Hysteresis Brake.

5.1.2 Conductors per Slot Number

The number of conductors per slot (N_c) comes at the end of the design process when the machine cross section is obtained. The main issue in the choice of N_c is to be able to respect the nominal voltage at nominal speed and nominal torque. The maximum speed point should be investigated from a general point of view. However, since there is no torque constraint in this part at maximum speed, only the performance at nominal point will be evaluated.

FE simulations show that the required torque of $2.2Nm$ is achieved when $A.N_c = 300Atr$ where A is the current's amplitude. At nominal speed of $3500rpm$, the nominal voltage should be around $125Vrms$. Varying the number of conductors, a $N_c = 30$ is found to respect the voltage limit with a 10% margin (Phase Induced Voltage = 112 Vrms). The corresponding current amplitude will be $I_{ph} = 10A$ and the phase total resistance is estimated at 0.5Ω. Therefore, a superior limit of the phase voltage can be calculated as the following:

$$V_{limit} = V_{induced} + RI_{rms} = 115.5V_{rms} \tag{5.1}$$

Therefore, a $N_c = 30$ is chosen for the design. In addition, the maximal current density is obtained at maximal torque. The current density at nominal torque can be calculated as the following:

$$J_s = \frac{I_{rms} * N_c}{S_{slot}} = \frac{300}{\sqrt{2}.140} = 1.515A/mm^2 \tag{5.2}$$

The current density of $1.1515A/mm^2$ is lower than the maximal $5A/mm^2$ imposed, and the current can be increased to obtain more machine torque.

5.2 Characterization of the Initial SynRM Design

5.2.1 Static Characterization

The developed machine is first tested statically to verify its ability to provide the required torque. A DC current is introduced into two machine phases in order to simulate a static operation point of the SynRM. An external machine is used to rotate the SynRM's rotor and a force sensor attached to the SynRM's stator is used to deduce the torque delivered by the machine. Figures 5.4 and 5.5 show the obtained static torque at $I_{DC} = 7A$ and $I_{DC} = 10A$ respectively in comparison with the FE simulation torque.

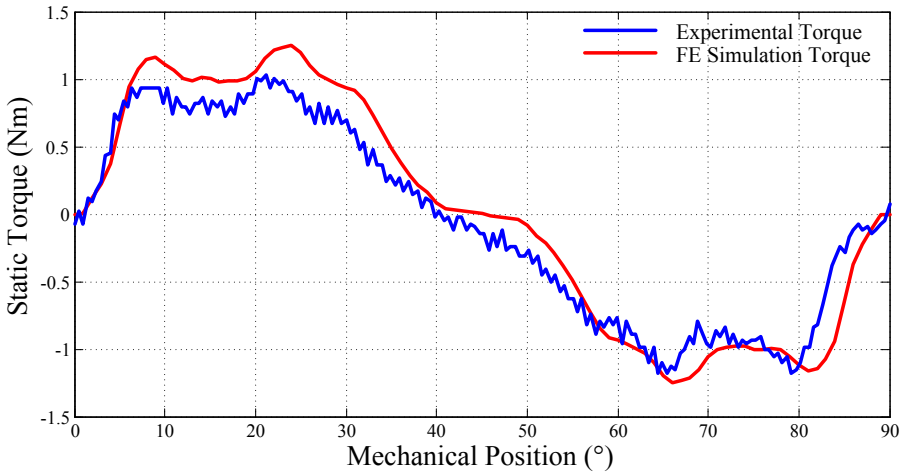

Fig. 5.4 SynRM static torque at $I_{DC} = 7A$.

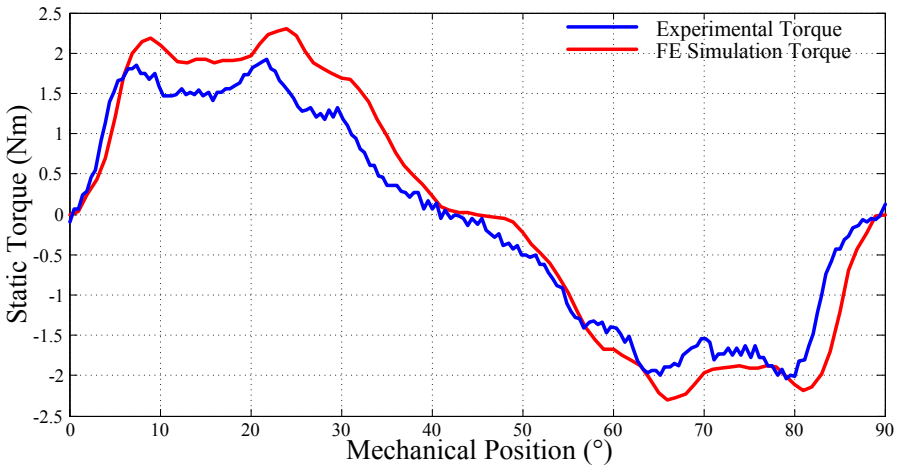

Fig. 5.5 SynRM static torque at $I_{DC} = 10A$.

The direct inductance (L_d) and the quadrature inductance (L_q) are measured by means of imposing an AC current in a phase while fixing the position of the rotor in the direct or the quadrature position with respect to the powered phase. The direct and quadrature inductances are measured as follows:

$$L_{d,q} = \frac{m}{2} \frac{Q}{2\pi f_e I_{rms}^2} \tag{5.3}$$

where m is the phase number = 2, Q is the reactive power in VAR, f_e is the current frequency and I_{rms} is the RMS value of the current.

The obtained values of the inductances are shown on figure 5.6. A saturation is observed on both the direct and the quadrature inductances. The saturation of the quadrature inductance is observed at low currents which corresponds primarily to the saturation of the ribs and the bridges. The direct inductance undergoes the saturation effect staring from $I_{rms} \approx 4A$. The full load operation point is at $I_{rms} = 7.07A$ and the corresponding values of the inductances are $L_d = 30mH$ and $L_q = 13mH$. Therefore, the saliency ratio is $\xi = 2.3$.

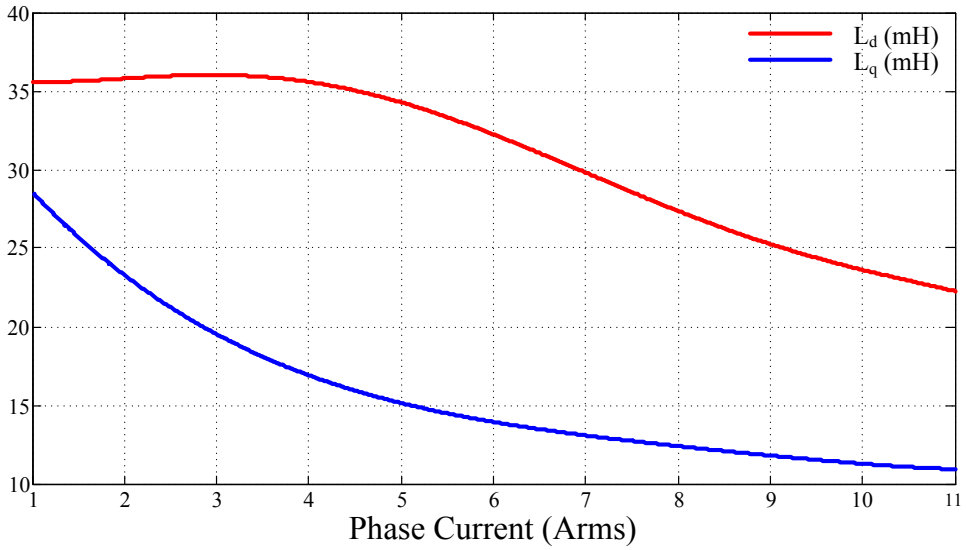

Fig. 5.6 Ld and Lq in function of Irms.

5.2.2 Torque Characterization

The current controller studied in section 4.4 is put in place. The verification of the control is shown in the next section. In this part, the current imposed in the 2 phases are purely sinusoidal and are expressed as the following:

$$\begin{aligned} I_a(t) &= I_1 cos(\omega_e t + \phi_1) \\ I_b(t) &= I_1 cos(\omega_e t + \phi_1 - \pi/2) \end{aligned} \tag{5.4}$$

The average torque in the steady state as a function of the current amplitude for different values of ϕ_1 is shown on figure 5.7, whereas the average torque as a function of ϕ_1 for different values of I_1 is shown on figure 5.8. The figures show that the MTPA phase angle tends to be bigger when the current increases. In other terms, more the machine is saturated more q-current (I_q) with respect to the d-current (I_d) is needed to ensure maximum torque at the same current magnitude.

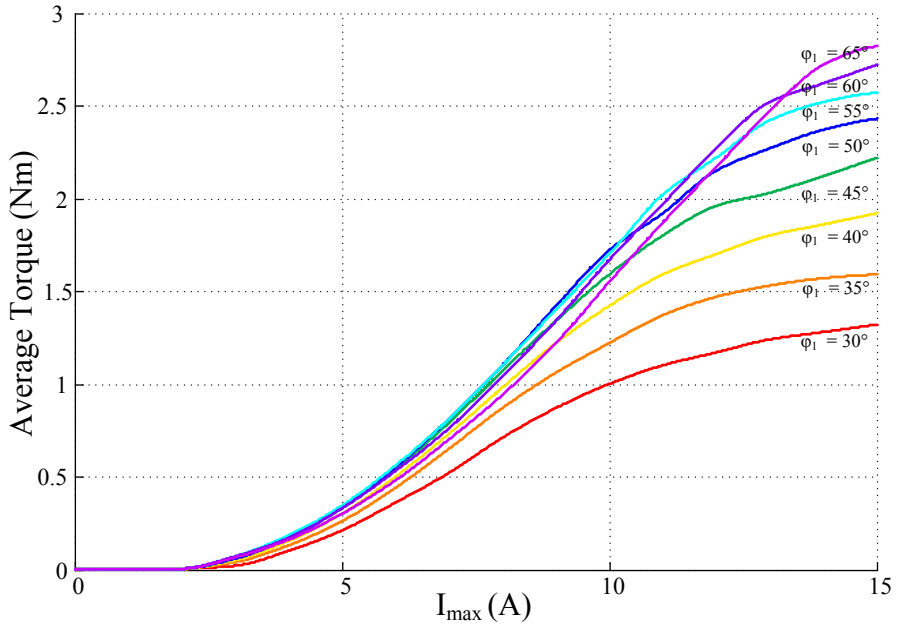

Fig. 5.7 Average torque as a function of the current amplitude for several values of ϕ_1.

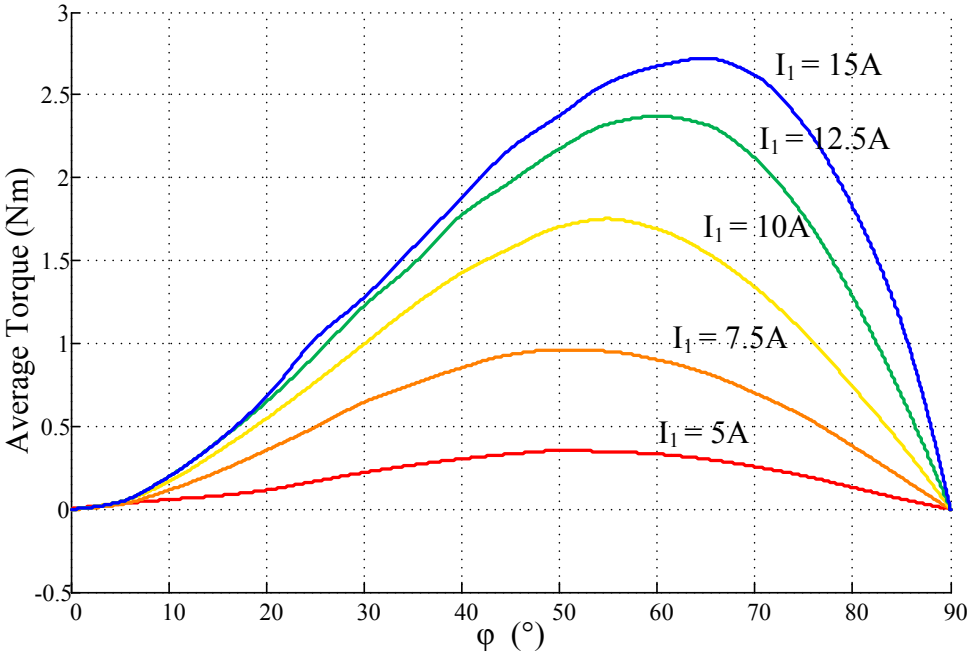

Fig. 5.8 Average torque as a function of ϕ_1 for several values of I_1.

5.3 Current Control Validation

Two RS controllers where studied in section 4.4. The first controller was synthesized for the case where the maximum speed is $\Omega_{max} = 7000rpm$, and only the fundamental current frequency is considered. The corresponding DC voltage (V_{DC}) is 200 V. The second controller is determined for harmonics injection in the phase currents. The current harmonics add a complementary constraint on the system frequencies, and the speed should be reduced in order to keep the PWM carrier frequency at $10kHz$. The maximum considered speed is $\Omega_{max} = 1500rpm$ in this case to be able to inject the 3^{rd} and 5^{th} current harmonics on the whole speed range. The corresponding DC voltage (V_{DC}) is 30 V in this case to be able to evaluate the field-weakening zone. This section will examine experimentally the two developed current control loops.

5.3.1 Current Control Validation for V_{DC} = 200V

The controller studied in this case is a 4^{th} order RS controller with a bandwidth frequency (F_{bw}) of 2000 Hz. The parameters of the controller and the system can be found in table 4.2. In order to evaluate the control performance, 4 operations points below or at the nominal speed are tested first:

- low-load low-speed operation point ($I_1 = 5A$ and $\Omega_{mec} = 1000rpm$)
- low-load nominal-speed operation point ($I_1 = 5A$ and $\Omega_{mec} = 3500rpm$)
- high-load low-speed operation point ($I_1 = 10A$ and $\Omega_{mec} = 1000rpm$)
- high-load nominal-speed operation point ($I_1 = 10A$ and $\Omega_{mec} = 3500rpm$)

The controller output m_a is plotted on figure 5.9 as well as the reference and actual phase currents. The current control shows acceptable performance for all 4 cases. At nominal speed, the current shows oscillations at its minimum and maximum values. This is primarily due to the impact of the saturation on the integral function in the controller even if the controller contains an anti-windup function. In order to limit this oscillation, a solution consists of disabling the integral function from the controller when saturation occurs. However, the current control is considered as acceptable in the presented case.

Figures 5.10(a,b) show the current control performance in zone 2 for $\Omega_{mec} = 5000rpm$ at low-load ($I_{amax} = 5A$, $\phi_1 = 68°$) and at maximal load ($I_{amax} = 10A$, $\phi_1 = 68°$). Similar oscillations to the case of the control at nominal speed are observed due to controller saturation as well. Furthermore, figure 5.10(c) shows the current control at the maximum speed operation point on the envelope in zone 3. At this speed, the current is not able to follow the current reference due to the lack of voltage input. Although the controller output m_a is at its maximal value of 1, the voltage is not sufficient for the current control. Therefore, a bang bang phenomenon where the controller output changes values from maximum to minimum value is seen. From the power of electronics point of view, the phenomenon is called over modulation. To resolve this issue, V_{DC} should be increased or the current should be decreased.

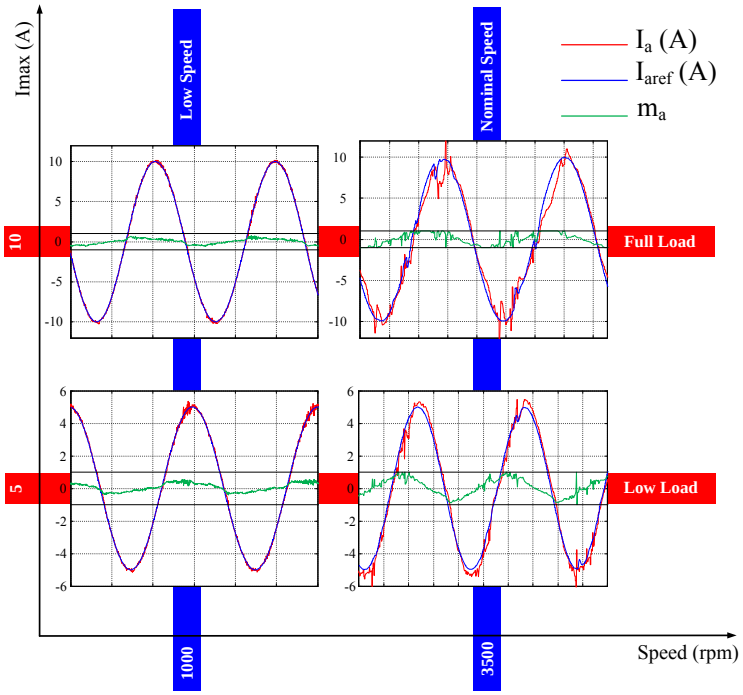

Fig. 5.9 Performance of the current controller for the four sample operation points in zone 1.

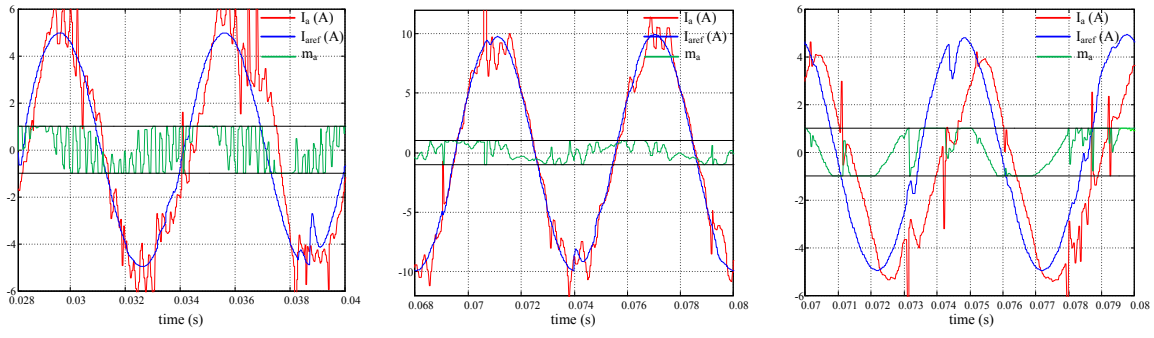

(a) (b) (c)

Fig. 5.10 Performance of the current controller for the two sample operation points in zone 2 $\Omega_{mec} = 5000rpm$: (a) low-load operation point ($I_1 = 5A$, $\phi_1 = 68°$), (b) full-load operation point ($I_1 = 10A$, $\phi_1 = 68°$), and (c) for the maximal speed operation point in zone 3: $\Omega_{mec} = 7000rpm$ where $I_1 = 5A$, $\phi_1 = 76°$).

5.3.2 Current Control Validation for $V_{DC} = 30V$

The DC voltage used in the case of harmonics injection is $V_{DC} = 30V$ in order to limit the machine speed and have the 3 operation zones as shown in section 4.4.5.6. The controller studied is a 4^{th} order RS controller with a bandwidth frequency (F_{bw}) of 1500 Hz. The current injected in the machine contains the 3^{rd} and the 5^{th} harmonics, and the current references for phase a and b are written as the following:

$$\begin{aligned} I_{aref} &= I_1 cos(\omega t + \phi_1) + I_3 cos(3\omega t + \phi_3) + I_5 cos(5\omega t + \phi_5) \\ I_{bref} &= I_1 cos(\omega t + \phi_1 - \pi/2) + I_3 cos(3(\omega t - \pi/2) + \phi_3) + I_5 cos(5(\omega t - \pi/2) + \phi_5) \end{aligned} \tag{5.5}$$

In order to evaluate the control performance, 4 operations points are tested:

- low-load low-speed operation point ($I_1 = 5A$ and $\Omega_{mec} = 300rpm$)
- low-load nominal-speed operation point ($I_1 = 5A$ and $\Omega_{mec} = 500rpm$)
- high-load low-speed operation point ($I_1 = 10A$ and $\Omega_{mec} = 300rpm$)
- high-load nominal-speed operation point ($I_1 = 10A$ and $\Omega_{mec} = 500rpm$)

For these 4 operation points, the phase angle is 53° which corresponds to the MTPA angle found experimentally for $I_1 = 10A$ (refer to figure 5.8). Furthermore, the current harmonics amplitude are $I_3 = I_5 = 1A$ for all the operation points.

The controller output m_a is plotted on figure 5.11 as well as the reference and actual phase currents. At full load, the controller output m_a saturates (gives values = 1). Nevertheless, an acceptable current control is observed on these limit points.

Figures 5.12(a,b) show the current control performance in zone 2 for $\Omega_{mec} = 700rpm$ at low-load ($I_1 = 5A$, $\phi_1 = 68°$) and at maximal load ($I_1 = 10A$, $\phi_1 = 68°$). Furthermore, figure 5.12(c) shows the current control at the maximum speed operation point on the envelope in zone 3. These figures show better current control than that in case of $V_{DC} = 200V$ even though a saturation of the control output (m_a) is observed on the performance envelope.

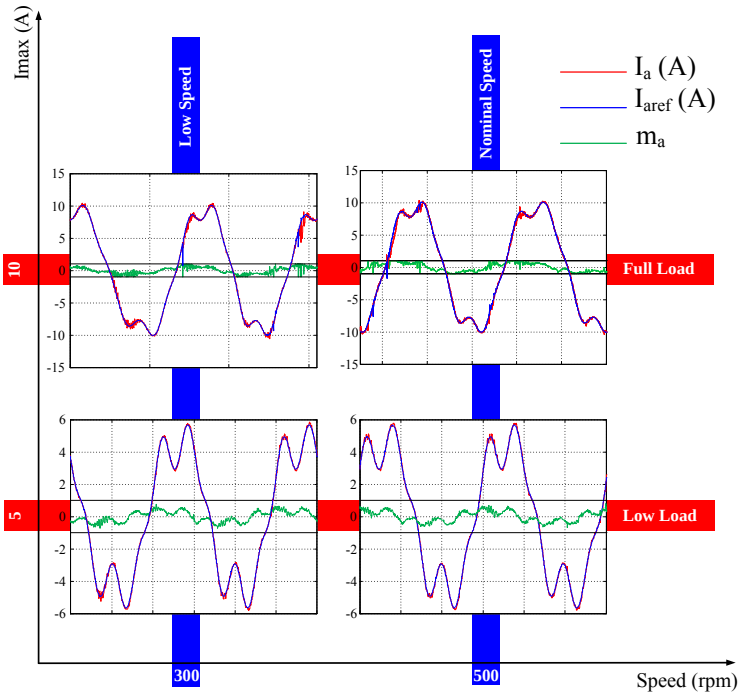

Fig. 5.11 Performance of the current controller for the four sample operation points with harmonics injection in zone 1.

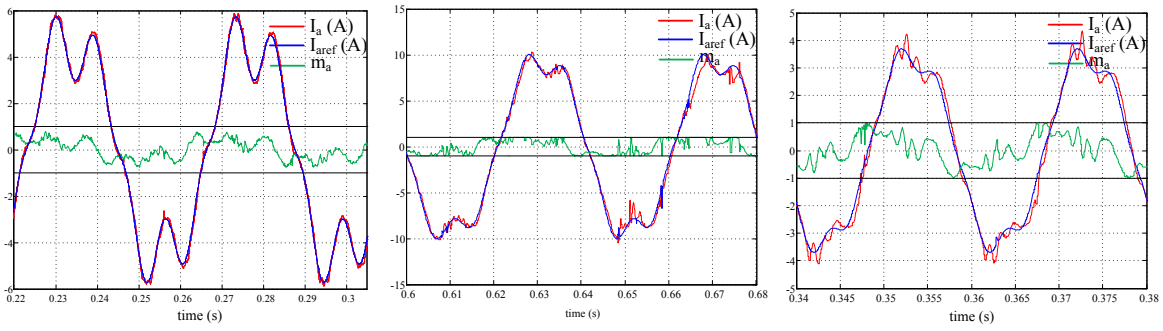

(a) (b) (c)

Fig. 5.12 Performance of the current controller for the two sample operation points in zone 2 $\Omega_{mec} = 700rpm$: (a) low-load operation point ($I_1 = 5A$, $\phi_1 = 68°$), (b) full-load operation point ($I_1 = 10A$, $\phi_1 = 68°$) and (c) for the maximal speed operation point in zone 3 ($\Omega_{mec} = 1500rpm$ where $I_1 = 3.75A$, $\phi_1 = 75°$). Harmonic amplitudes $I_3 = I_5 = 1A$ are defined to test the controller performance.

5.4 Efficiency Map of the Initial Design

The efficiency map of the initial design of the SynRM is shown on figure 5.13. To measure the machine input power a ZES Zimmer power meter model LMG450 is used to measure the voltages, the currents and the power consumed by the two phases of the machine. The output torque, speed and mechanical power is measured by the Magtrol hysteresis break (refer to section 5.1.1 for the test bench details).

Since a current amplitude of 10 A is not sufficient to deliver the needed 2 Nm, an amplitude of 11 A is permitted for the measure of the efficiency map. This will raise the current density to 1.65 A/mm^2 which stays acceptable for cooling by natural convection. For the efficiency map, the phase angle of each point is determined to have the maximal torque per ampere. The measurements are done in intervals of 500 rpm and 1 A. Later, a linear interpolation is used to draw the efficiency map. The efficiency for the operation point below 0.4 Nm are not represented due to the lack of precision of the torque sensor.

The efficiency map shows that the machine delivers its highest efficiency of 92 % around the nominal speed at full load. It is indicated by the graph that the highest efficiency point of the machine is outside the torque-speed envelope. This point will not be tested since the power is limited by the Magtrol brake.

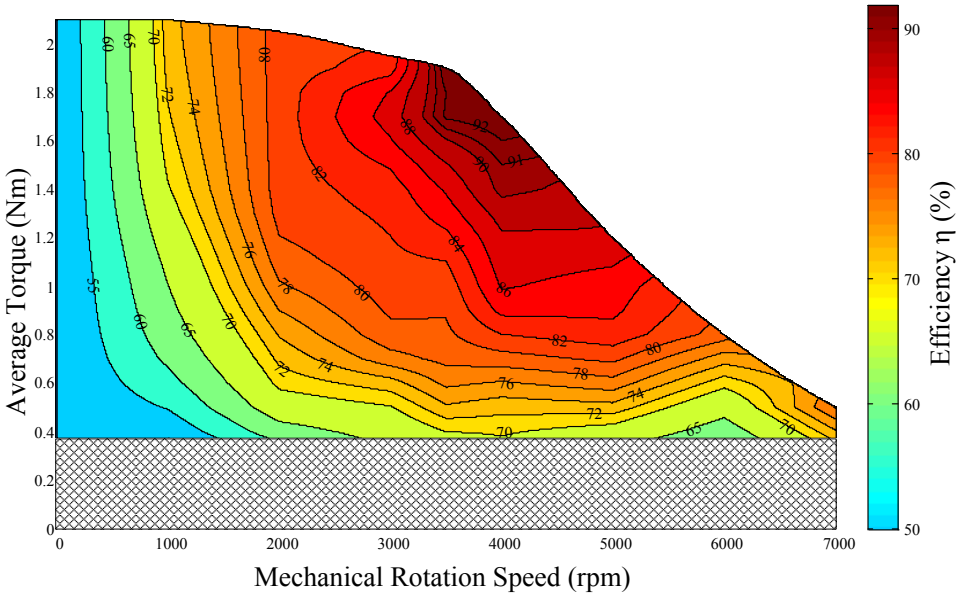

Fig. 5.13 Efficiency map of the SynRM using the initial rotor design.

5.5 Initial Design and Optimal Design Performance Comparison

The design optimization presented in chapter 3 was aimed to reduce the torque ripple (T_{ripple}). An optimal rotor design (OD) was obtained that has roughly the same performance as the initial rotor design (ID), that is obtained from the analytical design procedure presented in chapter 2, except for T_ripple. FE simulations show that the T_{ripple} of the OD is half (around 13 %) in comparison to the ID (28%) at the maximum torque operation points. The ID and the OD are shown on figure 5.14.

Fig. 5.14 Initial rotor design (right side) and optimized rotor design (left side).

The performance between the ID and the OD is compared for 4 operation points:

- OP1: low-load low-speed operation point ($I_1 = 5A$ and $\Omega_{mec} = 1000rpm$)
- OP2: high-load low-speed operation point ($I_1 = 10A$ and $\Omega_{mec} = 1000rpm$)
- OP3: low-load nominal-speed operation point ($I_1 = 5A$ and $\Omega_{mec} = 3500rpm$)
- OP4: high-load nominal-speed operation point ($I_1 = 10A$ and $\Omega_{mec} = 3500rpm$)

These operation points are either on the nominal speed (3500 rpm) or on a speed less than the nominal speed (1000 rpm). The field-weakening zones will be treated later in section 5.7. The results are shown in table 5.1. These experimental results prove what was concluded by the FE simulations that the two designs give similar

results except for the torque ripple. The OD shows a significant reduction of the torque ripple at the two operating points of 1000 *rpm*. However, this reduction becomes less apparent for 3000 *rpm*. This is due to phase current control that introduces current harmonics. As seen in figure 5.9, the current at nominal speed does not follow perfectly the fundamental current reference. This introduces current harmonics that reduce the torque ripple of the machine as will be seen in the next section.

	OP1		OP2		OP3		OP4	
	ID	OD	ID	OD	ID	OD	ID	OD
I_1 (A)	5	5	10	10	5	5	10	10
Φ_1 $(°)$	50	51	53	54	50	51	53	54
(Ω_{rpm})	1000	1000	1000	1000	3500	3500	3500	3500
Phase Voltage (V_{rms})	20	22.8	36	39	70	69	112	115
T_{avg} (Nm)	0.325	0.315	1.8	1.83	0.32	0.31	1.55	1.62
T_{ripple} $(\%)$	25	13	22	11	7	5	11	7
Power Factor $(-)$	0.39	0.36	0.51	0.51	0.32	0.31	0.46	0.45
Efficiency η $(\%)$	64	62	76	79	77	74	88	91

Table 5.1 Experimental performance comparison between the design based on the analytical approach (ID) and the optimized machine design (ID) for 4 operation points.

5.6 Experimental Validation of Harmonics Injection

For harmonics injection, the third and the fifth current harmonics are considered and the currents are expressed as the following:

$$\begin{aligned} I_a(t) &= I_1 cos(\omega t + \phi_1) + I_3 cos(3\omega t + \phi_3) + I_5 cos(5\omega t + \phi_5) \\ I_b(t) &= I_1 cos(\omega t + \phi_1 - \pi/2) + I_3 cos(3(\omega t - \pi/2) + \phi_3) + I_5 cos(5(\omega t - \pi/2) + \phi_5) \end{aligned} \tag{5.6}$$

As shown in chapter 4, the harmonics injection in the phase currents can lead to a reduction of the torque ripple (T_{ripple}) of the machine. Moreover, when the 3^{rd} and

the 5^{th} harmonic are injected simultaneously with the same amplitudes ($I_3 = I_5$), the torque theoretically does not decrease in comparison with the case of a pure sinusoidal current. The model that was used to establish this hypothesis does not take into account the supplementary core losses due to current harmonics. Therefore, the current harmonic concept will be put to test experimentally in this section. The initial design of the SynRM rotor is used for the demonstration.

First, current harmonics are injected for an operation point at MTPA. For the MTPA operation point, the RMS current is $I_{rms} = 7.07A$ and the phase angle of the fundamental current is $\phi_1 = 53°$. When harmonics are injected, the RMS current should be kept constant and the following equation should be respected:

$$I_{1rms}^2 + I_{3rms}^2 + I_{5rms}^2 = max(I_{rms})^2 \tag{5.7}$$

In terms of current amplitude, the relation can be written as:

$$I_1^2 + I_3^2 + I_5^2 = max(I_1)^2 \tag{5.8}$$

Harmonic injection is performed on the test bench, and a comparison between the case without harmonic injection and the case with harmonic injection ($I_{1rms} = 6.93A$, $I_{3rms} = I_{5rms} = 1A$) is shown on figure 5.15. The graph shows a slight decrease of the average torque (from $1.77Nm$ without harmonic injection to $1.75Nm$ with harmonic injection). This is mainly due to the increase in core losses in the machine structure when injecting harmonics. Nevertheless, this decrease is negligible ($\sim 1\%$). On the other hand, T_{ripple} decreases from 20% to 4% with harmonics injection.

As seen in chapter 4, the individual values of ϕ_3 and ϕ_5 are not important in contrast to the value of their difference $\phi_3 - \phi_5$. This is proven experimentally by changing the values of the ϕ_3 and ϕ_5 while keeping their difference constant. The impact of thies variation on T_{avg} and on T_{ripple} is negligible. Furthermore, the optimal $\phi_3 - \phi_5$ value is experimentally found at $-135°$. On the other hand, figure 5.16 shows the T_{avg}, T_{ripple} and ΔT (see equation (4.16)) as a function of $I_{3rms} = I_{5rms}$ for the locus shown on figure 4.6. The reason for taking directly the locus values (from the simplified model) and not the optimization values (from the pareto front on figure 4.8) is that they do not need an optimization procedure to be evaluated. Thus they could be generalized to any other 2-phase SynRM. The minimal torque ripple obtained is about 3%. A constant torque is not obtained on the locus of figure 4.6 since the core losses increase in the machine due to harmonics injection. Figure 5.16 shows also that without fundamental current ($I_{1rms} = 0$ and $I_{3rms} = I_{5rms} = 5A$), T_{avg} is about 44% of

the value with the fundamental current only. However, competitive operating points, where the T_{avg} decreases slightly and the T_{ripple} is around 3.5% from an initial value of 20%, are documented.

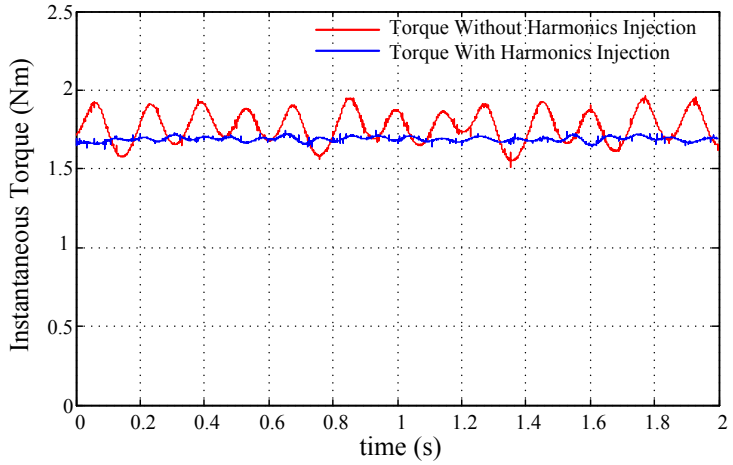

Fig. 5.15 Torque comparison between the case without harmonics injection ($I_{1rms} = 7.07A$, $I_{3rms} = I_{5rms} = 0A$) and the case with harmonic injection ($I_{1rms} = 6.93A$, $I_{3rms} = I_{5rms} = 1A$).

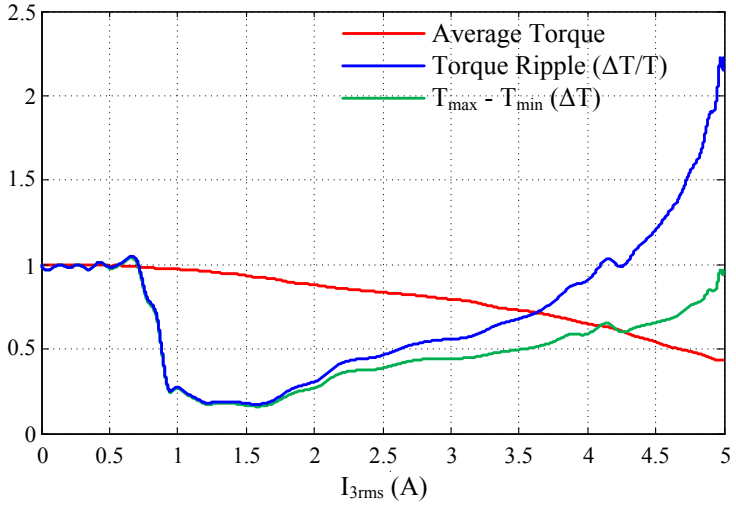

Fig. 5.16 Measured T_{ripple}, ΔT and T_{avg} of the SynRM in per unit with respect to the case without harmonics injection in function of I_{3rms} ($I_{3rms} = I_{5rms}$).

5.7 Experimental Comparison of Torque Ripple Reduction Techniques

This part deals with the experimental comparison of torque ripple reduction between design optimization and harmonics injection on the whole torque-speed envelope. V_{DC} is fixed at 30 V. I_1 and ϕ_1 evolve according to figure 4.23. The speed is limited to 1200 rpm, and the nominal speed is 400 rpm (refer to figure 4.23). The speed is limited due to harmonics control issues as seen in section 4.4.5.6.

The average torque and the torque ripple on the torque-speed envelope are shown on figures 5.17 and 5.18. Concerning the optimized design, the machine shows an improvement on the whole speed range with respect to the initial design (refer to figure 5.18). This proves what was found by simulation in section 3.7. The optimized machine shows a slightly lower torque as was found also by simulation in section 3.7 especially in the field weakening zone.

Even though the harmonics injection where studied in chapter 4 for speeds below nominal speed, the experimental results show harmonics injection on the whole speed range to study their effect. The case of the harmonics injection for the initial design shows a significant reduction of torque ripple on the whole speed range. The torque ripple with harmonics injection is lower than the optimized design's torque ripple at speeds lower than the nominal speed. Furthermore, the average torque in the case of harmonics injection is roughly the same as the case without harmonics injection below the nominal speed. However, in the third zone (field weakening zone where the current amplitude decreases as shown in figure 4.23), the harmonics amplitude that can be injected satisfying equation (5.8) is higher. In this zone, the torque is shown to increase with harmonics injection. This is a result of the generation of torque due to current harmonics that can be added to the fundamental torque generation.

In the case of harmonics injection for the optimized design, it has been found that more current harmonics are needed in order to decrease the torque ripple significantly. This leads to a decrease in torque due to excess losses and the reduction of the fundamental current even if the same locus as shown on figure 4.6. Harmonics injection leads to a reduction in torque ripple to around 3 % for speeds below the nominal speed and a maximal torque ripple of 8 % on the whole speed range.

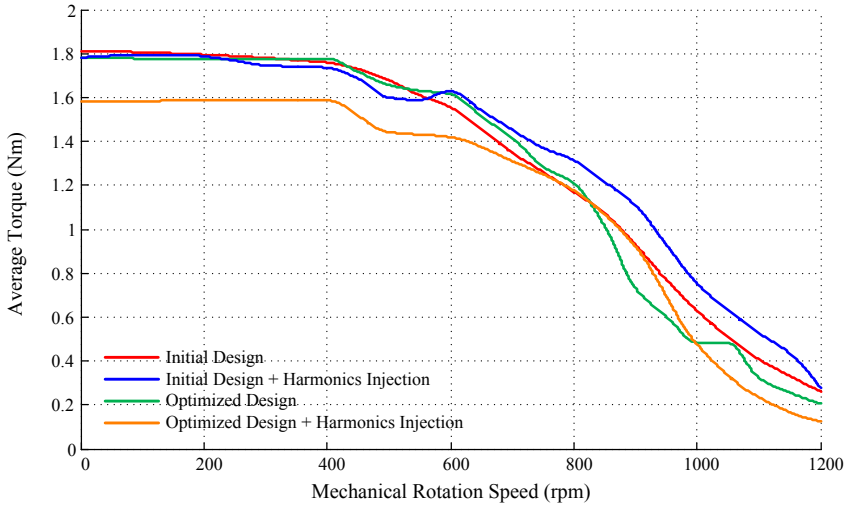

Fig. 5.17 Torque-speed envelope of the initial design and the optimal design with and without harmonics injection.

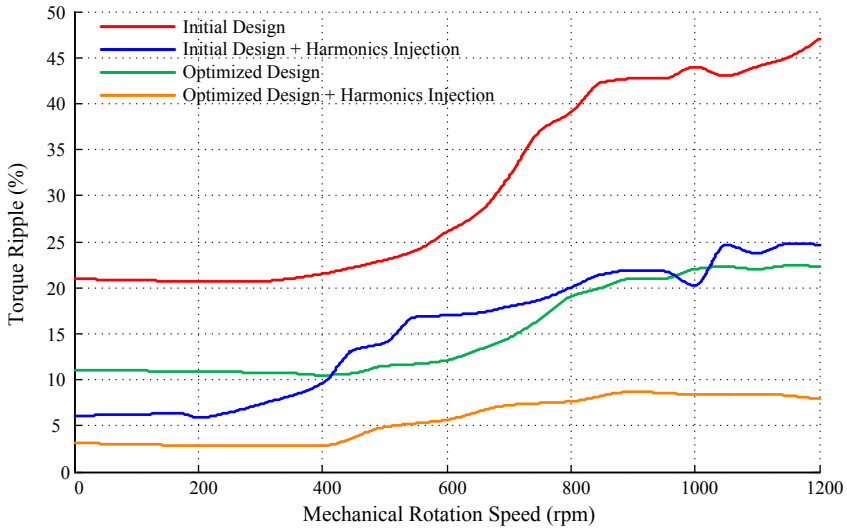

Fig. 5.18 Torque ripple on the torque-speed envelope of the initial design and the optimal design with and without harmonics injection.

Chapter Conclusion

This chapter handles the experimental validation of the theoretical and simulation aspects of the thesis. First, the machine prototype and the test bench are presented with the different equipment used. Then, the initial SynRM design that is based on the analytical procedure presented in chapter 2 is characterized. The characterization shows that a current amplitude of 11 A is needed in order to obtain the desired 2 Nm. In addition, it has been shown the evolution of the MTPA angle with the current amplitude. Afterwards, the current control loop is tested experimentally and validated for 2 cases: $V_{DC} = 200V$ and $V_{DC} = 30V$. The first voltage is used to obtain a speed of 7000 rpm and the second to be able to inject current harmonics on the whole speed range. The efficiency map obtained experimentally of the initial design is shown as well in this chapter. Then, the initial design and the optimal design performances are compared for 4 operation points below nominal speed. Moreover, the torque ripple reduction ability of the harmonics injection was proven experimentally and shown in this chapter. The last part of the chapter compares the torque ripple reduction of the optimal design and compared it to the torque reduction by harmonics injection. Both show a significant reduction. The harmonics injection concept reduces the torque ripple more than the optimization by design but is limited to low speeds since the controller has a limited bandwidth to control the current harmonics. Torque ripple minimisation by design shows a better performance on the whole speed range and when associated with harmonics injection, it gives the best torque reduction capabilities.

Chapter 6

Design of a SynRM for a Traction Application

Contents

The aim of this chapter is to propose a SynRM design that meets the requirements set for a mid-power traction application. The design procedure uses computer aided optimization design acting on the SynRM rotor and stator.

6.1 Machine Electromagnetic Specifications

The specifications of a machine in a general VSD application are defined in several domains: the mechanical domain where the machine should be mechanically strong and should withstand the maximal angular speed, the acoustic design where the machine should not exceed a certain acoustic threshold, the thermal domain where the limit temperatures of the machine components should be respected, and finally the electromagnetic domain. The electromagnetic domain determines the output electromagnetic torque and power capability with the voltage and the current limitations. Figure 6.1 shows the transient and the continuous torque envelopes. The most demanding from an electromagnetic perspective is the transient mode and the machine should be sized accordingly.

The main limits for the machine operation in an EV are the DC voltage (battery voltage) limit and the current density limit that is determined by the cooling system. The maximal voltage and the RMS current are also limited by the power electronics module. In the presented case, a V_{DC} of $300V$ is used to represent the battery voltage. Neither the maximal current RMS value nor the current density are limited. They will be later analysed when the machine cross section is obtained.

There are two volume constraints for this application:

- maximum stator outer diameter (D_{stat}) = $210mm$.
- maximum machine active length (L_a) = $228mm$.

6.2 SynRM Design

6.2.1 Design Approach

The design procedure will rely on an optimization study to define the SynRM cross-section. The fixed parameters for the optimization are shown in table 6.1. The current excitation in purely sinusoidal and the winding is a full-pole pitch winding. D_{stat} and L_a are chosen to be the maximal accepted values. When the machine cross-section is defined, L_a, the number of conductors per pole per phase (N_c), and the current

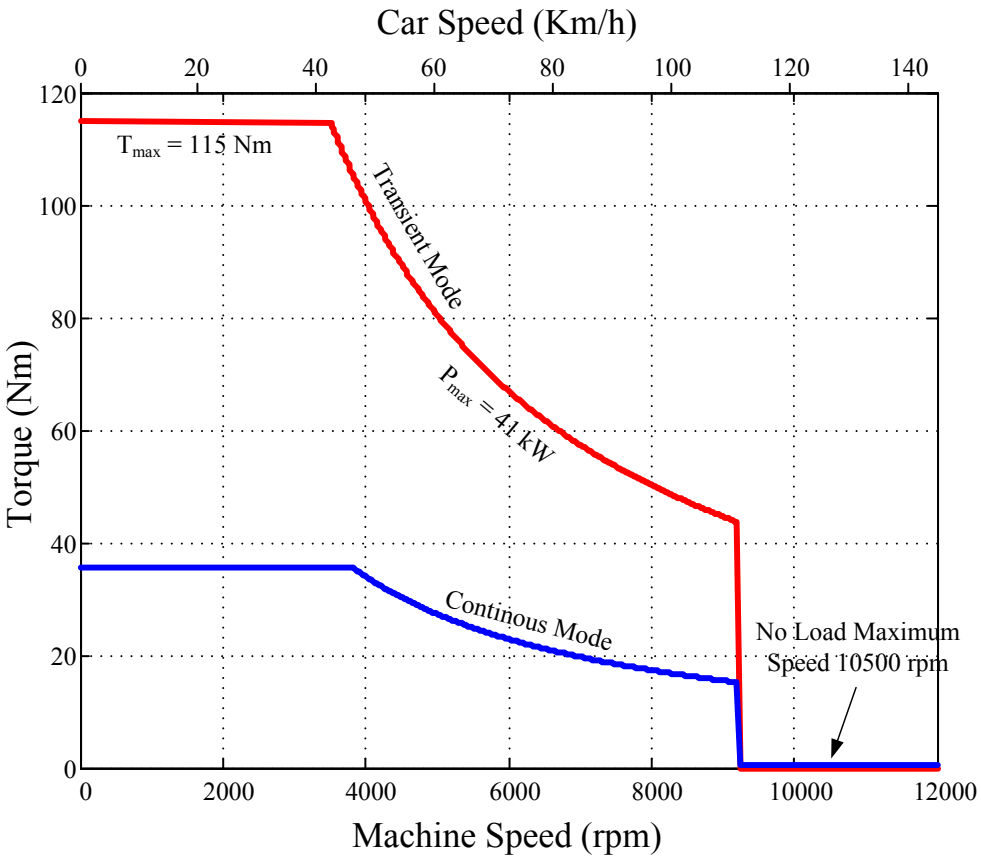

Fig. 6.1 Torque specifications for the transient and the continuous modes for a traction application.

amplitude will be chosen for that the machine can meet the required torque-speed specifications.

The variables of the SynRM to be optimized are the following (refer to figure 6.2 for the stator variables):

- Stator yoke height (Y_s)
- airgap diameter (stator inner diameter) (D_g)
- slot width (w_s)
- slot opening (O_s)
- slot opening height (h_s)
- rotor q-axis insulation ratio (K_{wq})

Parameter	Symbol	Value	Unit
Slot Number	N_s	32	–
Current Density	J_s	10	A/mm^2
Stator Outer Diameter	D_{stat}	210	mm
Active Length	L_a	228	mm
Stator Slot Filling Ratio	R_f	50	%
Airgap Width	g	0.5	mm
Shaft Diameter	D_{shaft}	30	mm
Phase Number	m	2	–
Pole Pair Number	p	2	–

Table 6.1 Fixed parameters for the SynRM design optimization.

- current phase angle with respect to the d-axis (ϕ_1)

The optimization variables that define the rotor design are D_g and K_{wq}. When D_{airgap} is defined from the optimization iteration the rotor outer diameter (D_{rotor}) is calculated as the following:

$$D_{rotor} = D_g - 2g \tag{6.1}$$

In addition, the procedure based on the flux lines in a solid rotor and the uniformity of the magnetic flux is used to draw the rotor (see section 2.3). This procedure requires the value of the rotor q-axis insulation ratio K_{wq} which is defined as an optimization variable.

Furthermore, the stator design is defined by Y_s, D_g, w_s, O_s and h_s (refer to figure 6.2). ϕ_1 is the current phase angle with respect to the d-axis. The current equation of phase a is written as:

$$I_a(t) = I_1 cos(\omega_e t + \phi_1) \tag{6.2}$$

where ω_e is the electric frequency (rd/s) of the current. The value of ϕ_1 varies from one design to another since it is affected by several non-linearities like the saturation and the axes cross-coupling.

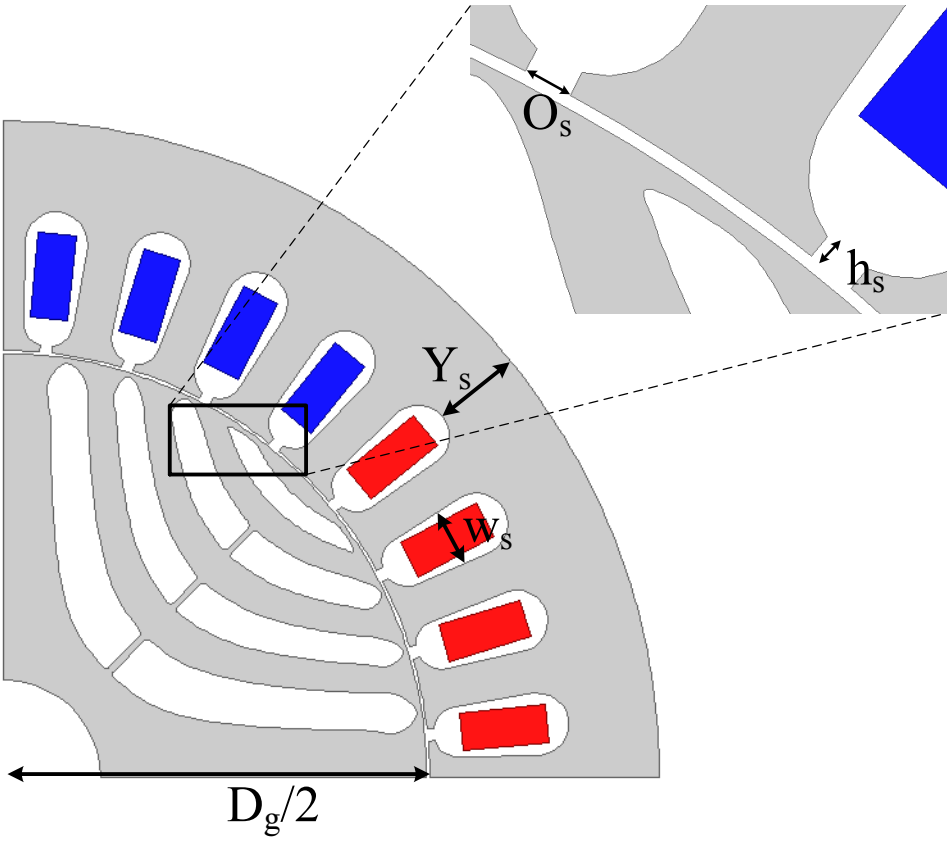

Fig. 6.2 Variables defining the stator geometry in the optimization procedure.

6.2.2 Parametric Optimization and Resultant Design

Concerning the optimization objectives, many criteria can be taken into account. For instance, in [109], six optimization criterion are taken into account for a single SynRM operation point: maximum torque per current density, maximum torque per Joules losses, maximum efficiency, maximum torque per kVA for a specified current density or maximum torque per kVA for with a minimal accepted torque limit. These 6 optimization criteria give different designs each.

Furthermore, in a complete optimization study for a traction application, several operation points should be taken into account that represent a standard drive cycle like the NEDC cycle (see chapter 1).

However, this study is merely a preliminary investigation and will optimize on the basis of the maximal torque per current density on the maximal load operation point at a speed below nominal speed. The integration of a several operating points

optimization, and the introduction of a multi-objective optimization can be later studied in a future work. The optimization algorithm used in the studied case is shown on figure 6.3 and the optimization problem is defined as the following:

$$\begin{aligned} &\max_{Y_s, D_g, w_s, O_s, h_s, K_{wq}, \phi_1} T_{avg} \\ &C : J_s = 10 A/mm^2 \end{aligned} \tag{6.3}$$

The optimization algorithm used is the Nelder-Mead simplex algorithm. The values of the initial values are calculated by the homothety of the design found in chapter 2. These values and the values of the variables after optimization are shown in table 6.2 and the evolution of T_{avg} in function of the optimization iteration number is shown on figure 6.4. The obtained design is shown on figure 6.5. At the same current density, the optimized SynRM design has gained 47% more torque.

The optimization procedure has the following characteristics:

- Number of function evaluations: 212
- Time of optimization: around 13 hours
- 47% more torque than the initial design

Parameter	Initial Value	Value after Optimization
Y_s	$14mm$	$18.5mm$
D_g	$136.5mm$	$108mm$
w_s	$9mm$	$7.4mm$
O_s	$2mm$	$2.7mm$
h_s	$1mm$	$0.77mm$
K_{wq}	0.5	0.48
ϕ_1	$51°$	$61°$

Table 6.2 Initial and final variable values after optimization for $J_s = 10A/mm^2$.

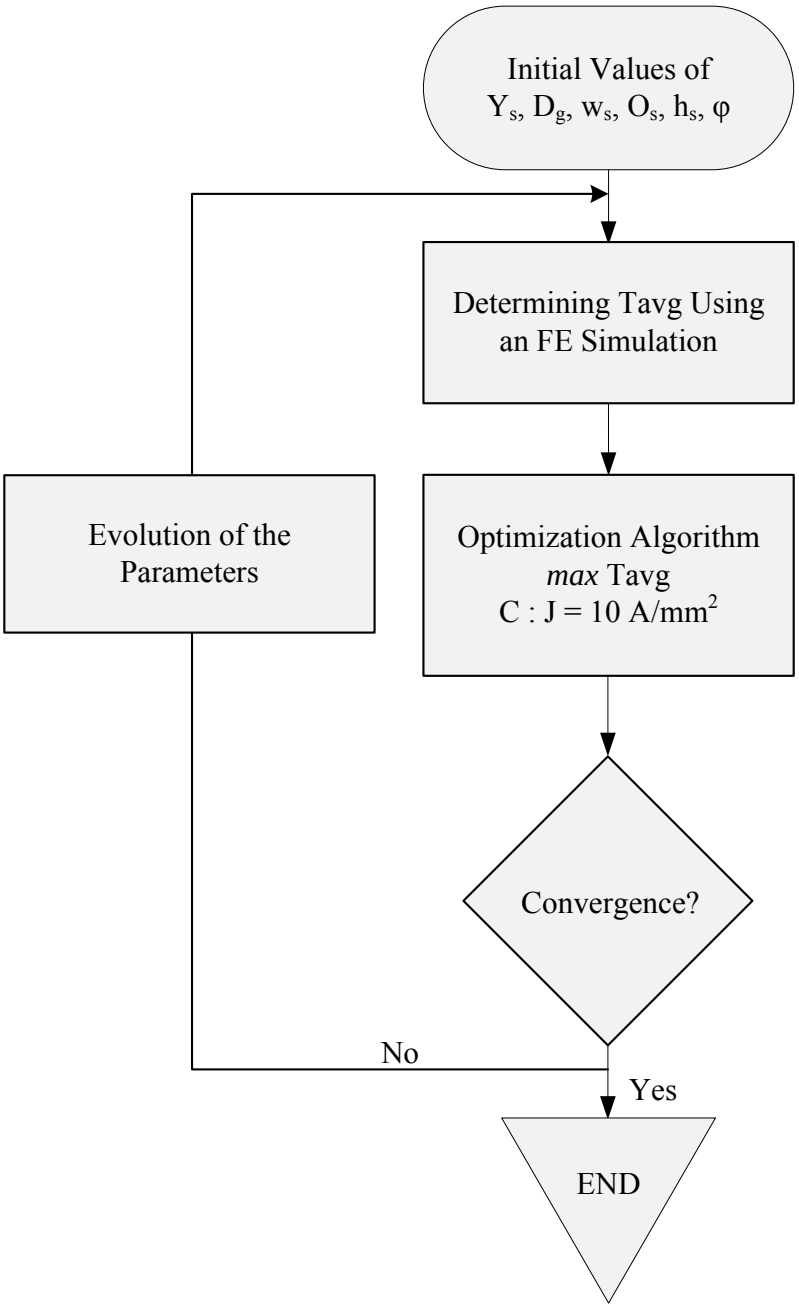

Fig. 6.3 Optimization algorithm used to determine the design geometrical parameters.

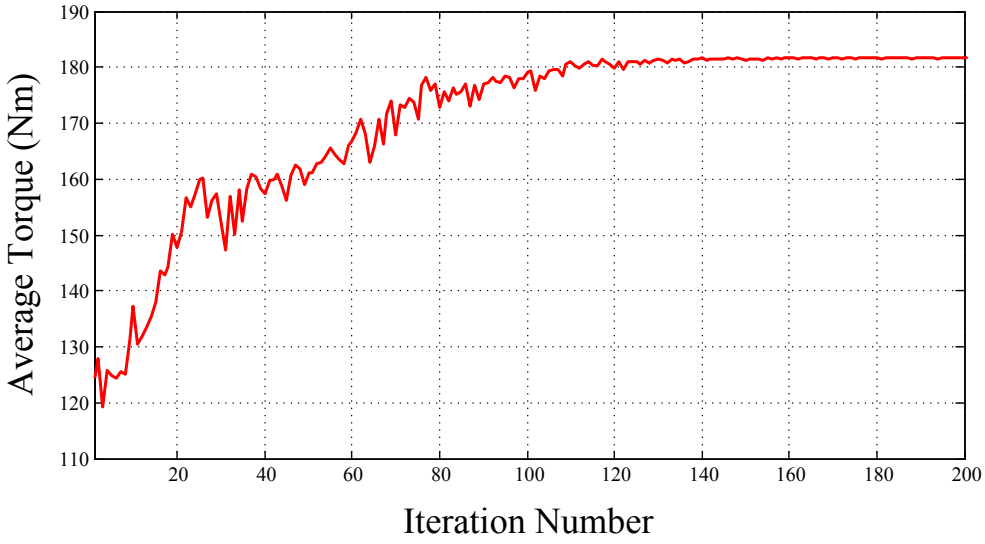

Fig. 6.4 Average torque vs iteration number for the optimization with $J_s = 10A/mm^2$.

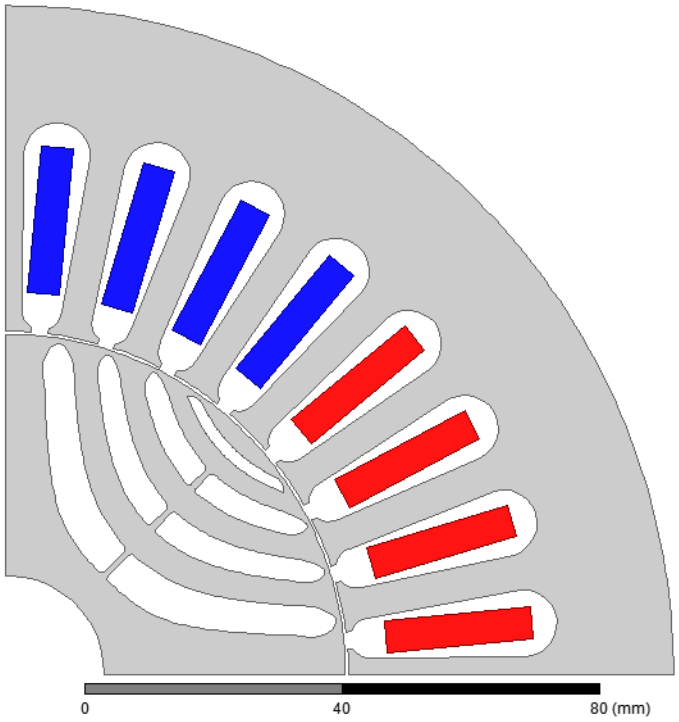

Fig. 6.5 Final design after the optimization.

6.2.3 Mechanical Validation

The Von Mises stress test is shown on figure 6.6. The steel used for the design is $M400 - 35A$ the same as the one used for the prototype. The maximal reported stress at 10500 rpm is around 210 MPa (a safety margin of 45 % for an elastic limit of 385 MPa) and is considered safe at the maximal speed. Moreover, the maximal deformation of the rotor for the 10500 rpm is 21.65 μm or 4 % of the airgap length.

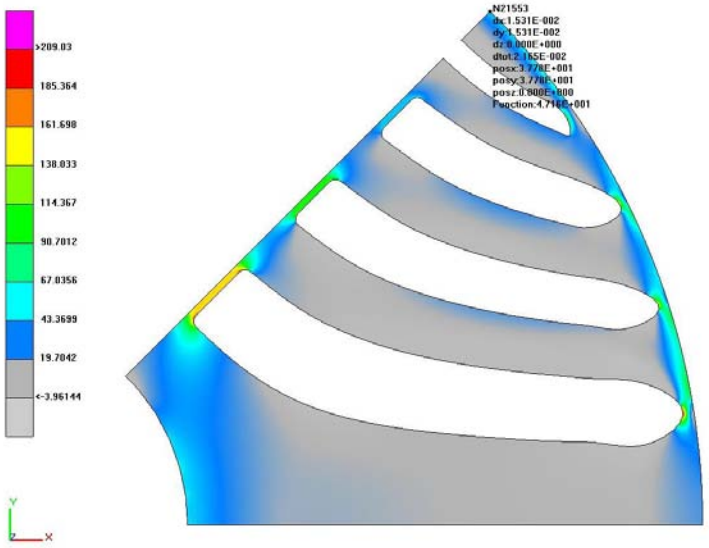

Fig. 6.6 Rotor stress (Von Mises element stress) and mechanical deformation for the proposed design at 10500 rpm.

6.3 Design Variation and Specification Comparison

Now that the machine's cross-section is obtained, the SynRM active length (L_a), the number of conductors per slot (N_c) and the current density can be chosen. In a general case, the torque of the machine is proportional to L_a and in the case of the SynRM, the torque is proportional to the square of the current density:

$$\begin{aligned} T_{SynRM} &\propto L_a J_s^2 \\ &\propto L_a (I_{rms} N_c)^2 \end{aligned} \tag{6.4}$$

where

$$I_{rms} = \frac{J_s R_f S_{slot}}{N_c} \tag{6.5}$$

R_f represents the stator slot fill ratio and S_{slot} the slot area.

In the case of a sinusoidal steady state, the phase induced voltage ($V_{induced}$) is proportional to the phase flux linkage. In addition, the flux linkage is proportional to L_a and the following equation can be written for the sinusoidal steady state:

$$V_{induced} = N_c \Phi_{elem} L_a \tag{6.6}$$

where Φ_{elem} is the flux linkage per length unit per elementary coil.

The machine is limited by the current density on the torque-speed envelope below nominal speed and by the voltage above it. Increasing the number of conductors (N_c) leads to the increase of the phase induced voltage and leads to the penalization of the field-weakening zone. However, increasing N_c leads to the decrease of the current rating which is beneficial for the power electronics. Similarly, the increase of L_a leads to the increase of the $V_{induced}$ and the decrease of the current rating for a rated torque. The idea is to chose a combination of these two variables in order to respect the most demanding machine electromagnetic specifications imposed by the red curve on figure 6.1. The current density will be changed according to the values of L_a and N_c. However, the machine design is optimized for a value of $J_s = 10A/mm^2$. It will be assumed that the optimized cross-section is the optimal for different values of J_s. This is true when the machine does not greatly saturate for high J_s. In addition, when the choice of a given design is made, a supplementary optimization run can be done with the value of the corresponding J_s and a more adapted machine design can be obtained.

Three considerations have to be accounted for when choosing these two variables:

- The maximum current density (J_s) should be limited to limit the cost and the complexity of the cooling system associated with the machine.
- L_a should be as small as possible to reduce the volume of the machine and its raw material cost.
- The maximal RMS current should be limited because the inverter's cost increases with the rated current.

Figures 6.7, 6.8 and 6.9 shows 3 configurations of the SynRM with different values of L_a, N_c and J_s that meet the electromagnetic specifications of the transient mode. These three configurations have the following characteristics:

- Configuration 1: High L_a (170 mm) - Low J_s (8.5 A/mm^2) - $N_c = 3$.
- Configuration 2: Medium L_a (142 mm)- Medium J_s (10 A/mm^2) - $N_c = 3$.
- Configuration 3: Low L_a (100 mm)- High J_s (16 A/mm^2) - $N_c = 4$.

The SynRm delivers a peak power higher than the necessary power in the three configurations. This is necessary to be able to maintain the power needed at maximum speed which is the most demanding operation point in the field weakening zone.

Table 6.3 compares the 3 configurations' volume, weight, specific power, rated current and current density. The calculated weight includes the steel and the total copper weight (active copper + end windings). The machine housing and the shaft are not considered. Configuration 1 needs the least current density and the rated current, but has a low specific power. In contrast, configuration 3 delivers the highest specific power but needs more current and current density. Therefore, a bigger inverter is needed as well as a better heat management system. Configuration 2 delivers an intermediary solution on the mentioned 3 performance indicators.

Configurations 1 and 2 have a $N_c = 3$. While, due to the small value L_a in configuration 3, N_c could be chosen at 4 keeping the same voltage limit (refer to eauation (6.6)). Increasing N_c leads to the decrease of I_{rms} (refer to equation (6.5)). However, in configuration 3 the current density is high and could not lead to a smaller current rating in comparison to configuration 2.

	Volume (m^3)	Weight (kg)	Specific Power (kW/kg)	Rated Current (A_{rms})	Current Density (A/mm^2)
Configuration 1	58.8×10^{-4}	47.2	0.87	244	8.5
Configuration 2	49.2×10^{-4}	41.3	0.99	287	10
Configuration 3	34.6×10^{-4}	32.4	1.27	346	16

Table 6.3 Performance comparison of the different configurations.

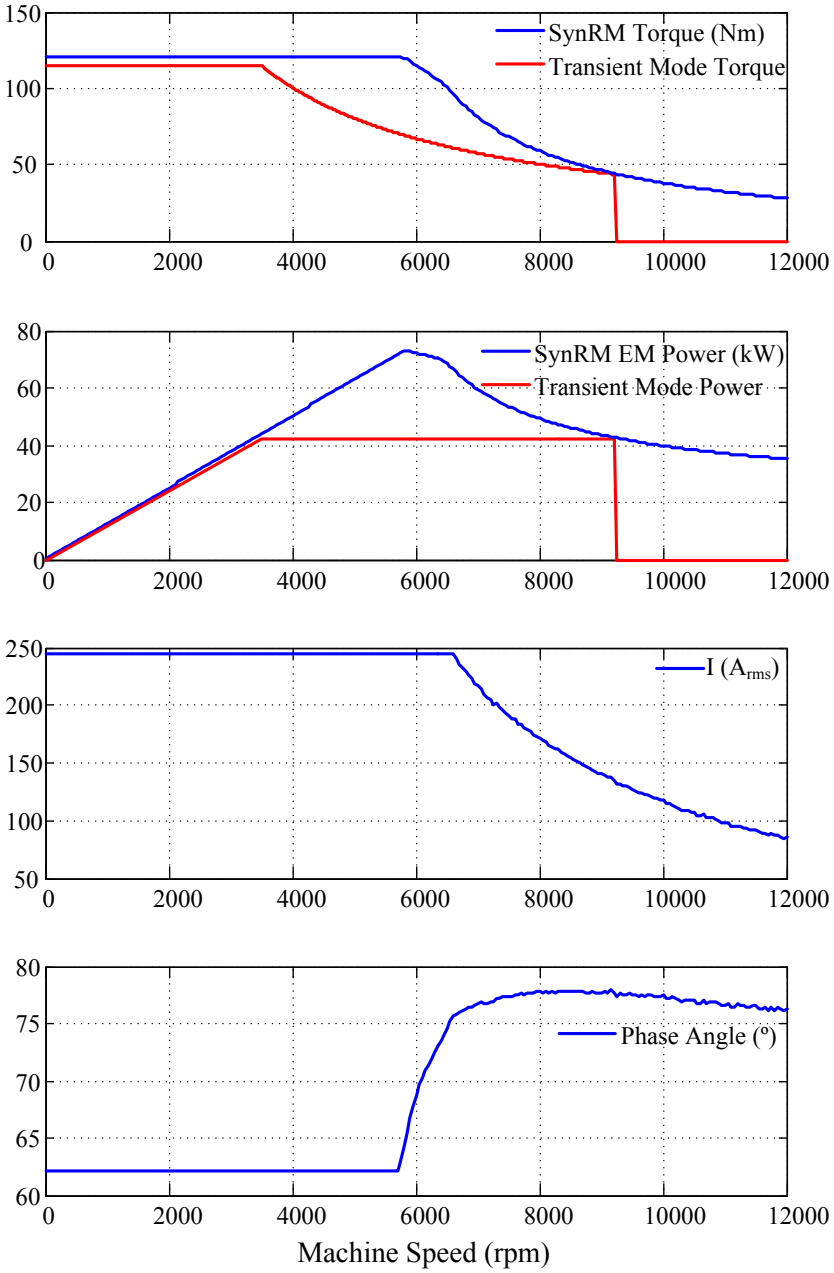

Fig. 6.7 FE simulation performance of SynRM configuration 1: $L_a = 170mm$, $N_c = 3$ and $J_s = 8.5A/mm^2$.

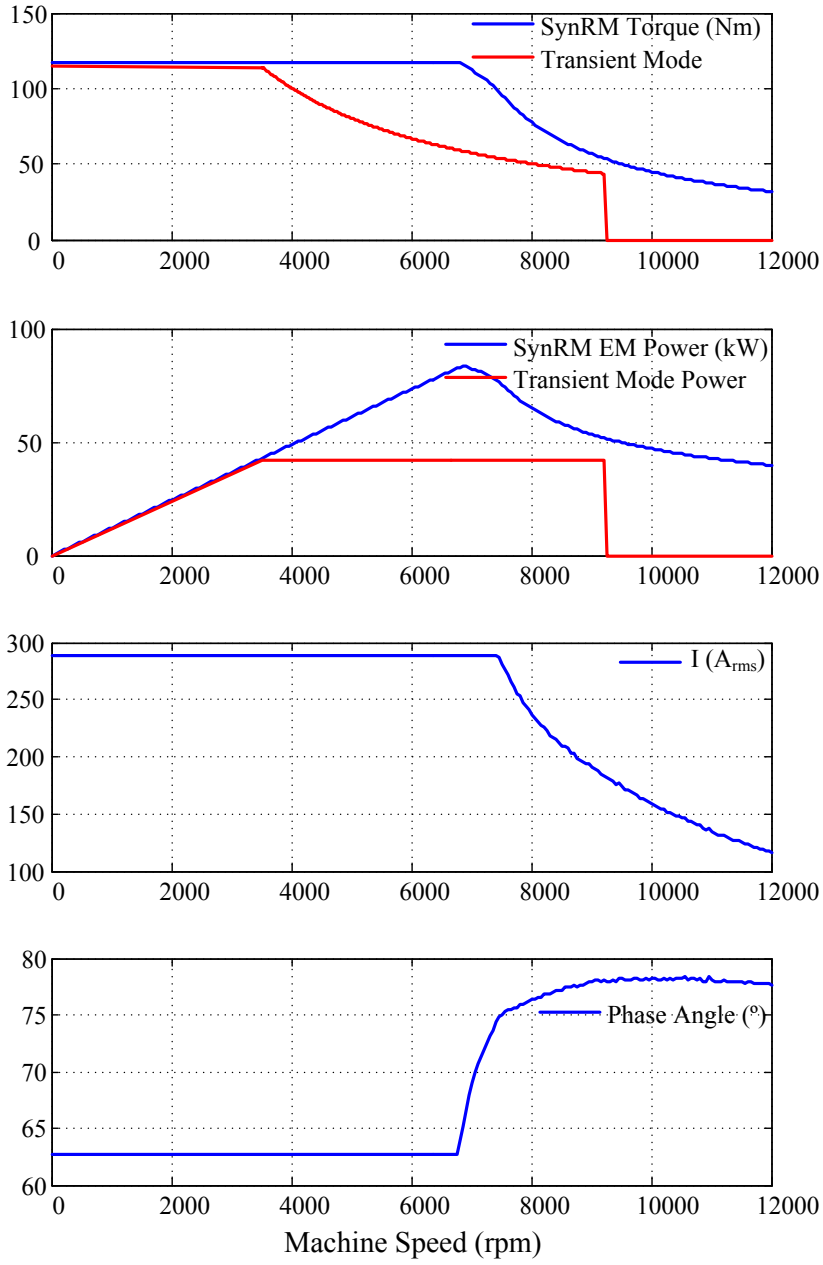

Fig. 6.8 FE simulation performance of SynRM configuration 2: $L_a = 142mm$, $N_c = 3$ and $J_s = 10A/mm^2$.

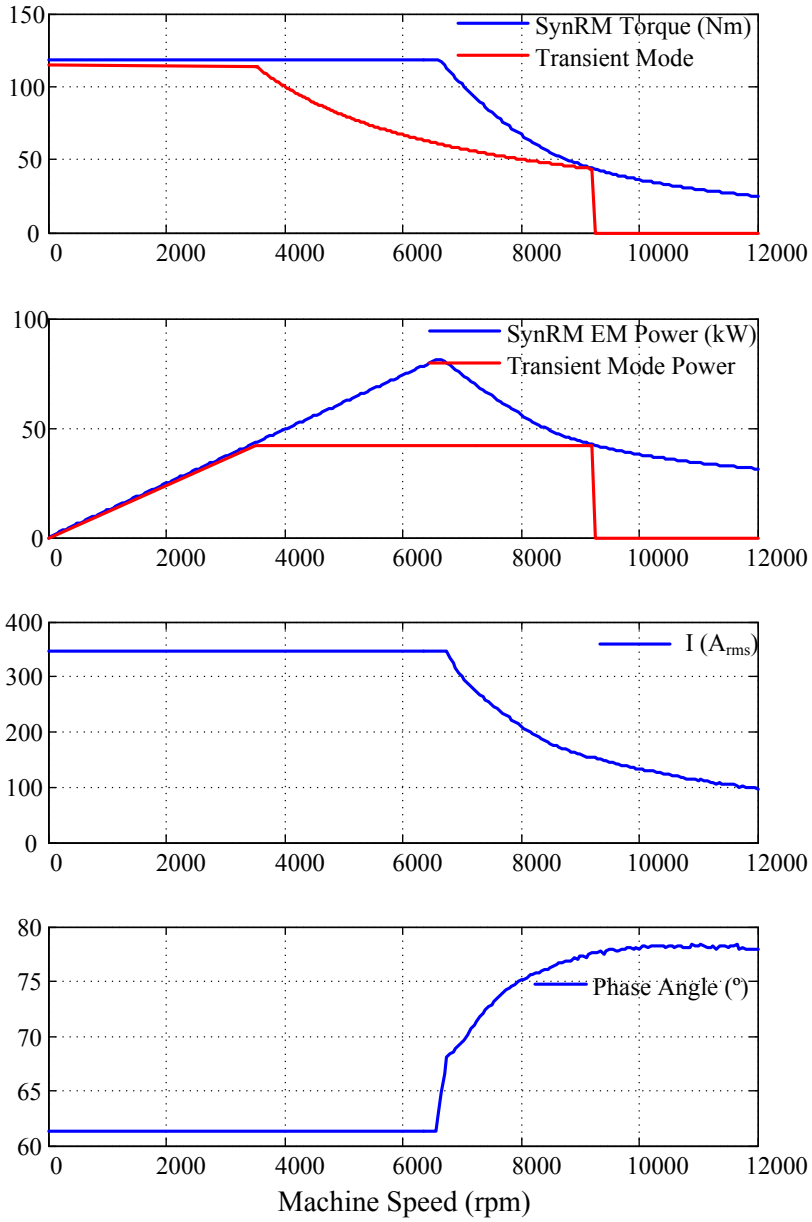

Fig. 6.9 FE simulation performance of SynRM configuration 3: $L_a = 100mm$, $N_c = 4$ and $J_s = 16A/mm^2$.

6.4 Performance of the SynRM Configuration 2 Design

The performance of the SynRM configuration 2 ($L_a = 142mm$, $N_c = 3$ and $J_s = 10A/mm^2$) is studied in this section. Table 6.4 shows the performance of the machine at nominal speed and full torque operation point obtained from FE simulations. The power factor (0.76) is significantly higher than the case of the machine prototype developed in chapter 2. However, this value remains low in comparison with other machine technologies like the induction machine. A solution for increasing the power factor relies in introducing ferrite permanent magnets. The torque ripple shown from the FE simulation (15 %) is relatively high for such application. Nevertheless, a supplementary optimization procedure to the rotor design can be added to reduce the torque ripple without impacting the torque capability of the machine like done in chapter 3. The efficiency of the machine at the nominal point is of 97.5 %. This value is highly desirable and is comparable with PMSM [9].

Figure 6.10 shows the efficiency map of the 2^{nd} configuration of the SynRM in the whole torque-speed range of the application specifications obtained from FE simulations. The core loss model used is Bertotti's model [82] for the M330-A35 magnetic steel. The efficiency map shows that the SynRM is highly efficient at high speeds and has a large zone where the efficiency is more than 98 %.

Chapter Conclusion

This chapter proposes a SynRM design for a traction application that respects the application's electromagnetic specifications. The design is based on a combination of the analytical rotor design presented in chapter 2 and a parametric optimization study for the SynRM's rotor and stator to optimize the torque per current density of the machine. Three configurations of the SynRM design are later presented that have diverse performances from the maximal rated current, the specific power and the current density point of view. The performance of one of these configurations on the nominal operation point is shown. Furthermore, the efficiency map of the machine show that the machine design is highly efficient, primarily, due to the absence of magnet losses and rotor Joules losses like in the case of the PMSM and the IM respectively.

	Symbol	Value	Unit
Current RMS value	I_{rms}	287	A
Current Angle	ϕ_1	61	$^\circ$
Rotation Speed	Ω_{mec}	3500	rpm
Induced Voltage	IV	102	V_{rms}
Average Torque	T_{avg}	117	Nm
Torque Ripple	T_{ripple}	15%	–
Power Factor	PF	0.76	–
Efficiency	η	97.5	%
Joules Losses	P_{Joules}	1390	W
Core Losses	P_{Core}	250	W

Table 6.4 Performance of the SynRM design under configuration 2 at nominal operation point obtained from FE simulations.

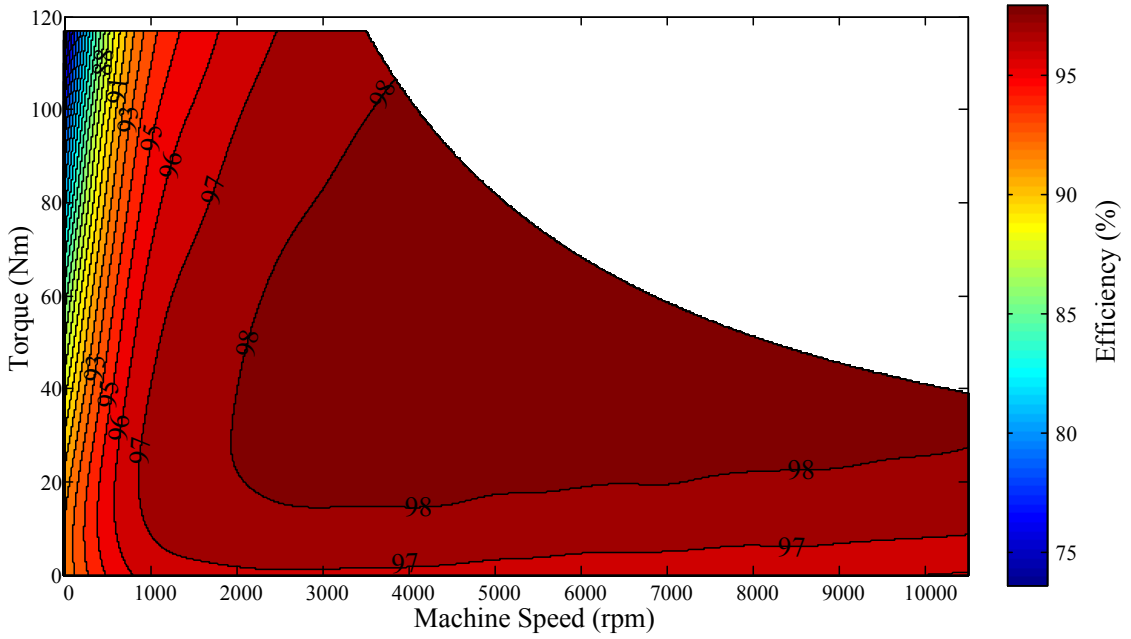

Fig. 6.10 Efficiency Map of the Configuration 2 of the SynRM inside the transient mode torque-speed envelope obtained from FE simulations.

General Conclusion

This work is dedicated to the study and the performance enhancement of the SynRM. The study concentrates on a mid-power automotive application but can be adapted to any VSD application of the SynRM. The first chapter of the thesis puts the work into context. It presents the electric machine in the electric vehicle, the required machine performance and the motor trends. The reasons for choosing the SynRM are discussed in the first chapter as well. The SynRM robustness, ease of control and high efficiency makes it a viable candidate in the next generation of low or mid-power traction applications. However, the SynRM's low power factor, its high torque ripple and its low torque density present obstacles to surmount. The SynRM concept and its equations are presented to fully understand the machine operation. An operation diagram of the SynRM depending on the machine speed is shown and discussed.

After a literature study, it has been found that few publications focused on an explicit method to design the machine rotor which has a complicated topology. The second chapter of the thesis presents an analytical design procedure of the SynRM rotor. This design procedure is based on the flux lines and the uniformity of the magnetic field in a solid rotor. Therefore, an analytical study that uses the electromagnetic equations and the constitutive properties of the material is performed to obtain the equation of the flux lines and field in a solid rotor. This procedure is compared to the circular flux barriers design and shows better results especially on the torque per ampere level. Several design aspects are also studied for the SynRM like the presence of the cut-off, the ribs and the bridges' dimensions and the insulation ratio in the rotor q-axis. This design shows a high torque ripple rate for which an analytical model is hard to obtain. In this regard, an optimization study is proposed in the third chapter to reduce the torque ripple without impacting the machine torque or the saliency ratio. The optimization problem is formalized and treated as well as the associated optimization algorithm. The Nelder-Mead simplex algorithm is thought to be a competitive alternative to evolutionary algorithms like genetic algorithms which

are highly time consuming. The optimization results are shown in the third chapter and FE simulations show that the torque ripple is cut to half its initial value.

The second axes of the study is the impact and the control of the SynRM current harmonics. The current harmonics impact on the machine average torque and the torque ripple in a general m-phase machine is studied in chapter 4. Then, the harmonics injection is applied to a 2-phase machine. The two phase machine has the ability to generate a non-zero average value torque from the 3^{rd} and the 5^{th} current harmonics which is the main reason for this choice. The harmonics injection applied on the 2-phase machine model shows that the torque ripple can be reduced by 40 % at the same average torque. This is done by simultaneously injecting two consecutive odd harmonics at the same amplitude. The third and the fifth harmonics are chosen since they are easier to control than higher harmonics. The current control is studied also in the fourth chapter. The current reference is chosen as the (ab) reference since the (dq) park transformation is found not to have a significant benefit for harmonics control in a 2-phase machine after a study on a general m-phase machine. The SynRM is modelled in Matlab/Simulink and a 4^{th} order RS controller is synthesized. The machine model is linearised around an inductance value in order to determine the RS coefficients. Therefore, the impact of this linearisation is evaluated and a model observer is proposed to estimate to non-linear terms. This observer showed a slight improvement in the control. However, since the RS controller is robust enough to eliminate model variations, the controller shows good results without the model observer as well. Another RS controller is studied to be able to inject harmonics on the whole speed range which is reduced in the perspective to not increase the PWM carrier frequency.

The fifth chapter of this thesis validates experimentally wthe findings of the previous chapters by theory or by simulation. The test bench is shown, and the equipment is described. Afterwards, the machine design based on the analytical procedure presented in chapter 2 is characterized. The current control is also validated, and the limitations are shown and are discussed. Then, the experimental efficiency map of the initial design is presented, and the inital design is compared to the optimized design in chapter 4 for 4 operation points. Concerning the harmonics injection, the experimental data show that the torque ripple can decrease as low to as 4 % without impacting significantly the torque of the machine. An experimental comparison of torque ripple reduction capabilities between the design optimization and harmonics injection is finally shown in the fifth chapter. It has been shown as well that combining the two procedure results in a torque ripple around 3 %.

The sixth chapter presents a design procedure of a SynRM for a traction application. First, the electromagnetic specifications for a mid-power traction application are presented. A design optimization procedure is defined afterwards to optimize the torque per current density of the machine. The conductors per slot and the machine active length are studied and 3 configurations with different strong-points are presented. One configuration requires a low current density while the other has a high power density. The third configuration has in intermediate values. The performance of this configuration is shown using FE simulations.

The prospects of this work are the following:

- Firstly, from a design point of view, the optimization algorithm will be evaluated to include an efficiency constraint and a power factor constraint for the machine design.
- Secondly, since the interaction of the 3^{rd} current harmonic and the 5^{th} current harmonic reduce the torque ripple without theoretically impacting the average torque, this could be extended to 3 phase machines. The harmonics injection will be tested in a 3-phase machine which represents the vast majority of the SynRM configurations.
- Finally, a third prospect would be in developing a general control law that determines the harmonics injection rate ($I_3 = I_5$) directly in function of the operation point without taking into account the machine parameters. This allows to implement the harmonics injection concept to any SynRM without extensively studying its parameters.

References

[1] I. Boldea, L. Tutelea, L. Parsa, and D. Dorrell, "Automotive Electric Propulsion Systems With Reduced or No Permanent Magnets: An Overview," *IEEE Transactions on Industrial Electronics*, vol. 61, pp. 5696–5711, Oct. 2014.

[2] R. R. Moghaddam, *Synchronous reluctance machine (SynRM) in variable speed drives (VSD) applications*. PhD thesis, Royal Institute of Technology, School of Electrical Engineering, Stockholm, Sweden, 2011.

[3] S. Taghavi, *Design of Synchronous Reluctance Machines for Automotive Applications*. PhD thesis, Concordia University, Montreal, Quebec, Canada, 2015.

[4] J. de Santiago, H. Bernhoff, B. Ekergård, S. Eriksson, S. Ferhatovic, R. Waters, and M. Leijon, "Electrical Motor Drivelines in Commercial All-Electric Vehicles: A Review," *IEEE Transactions on Vehicular Technology*, vol. 61, no. 2, pp. 475–484, 2012.

[5] C. Chan, "The state of the art of electric and hybrid vehicles," *Proceedings of the IEEE*, vol. 90, no. 2, pp. 247–275, 2002.

[6] M. Guarnieri, "Looking back to electric cars," in *2012 Third IEEE HISTory of ELectro-technology CONference (HISTELCON)*, pp. 1–6, Sept. 2012.

[7] J. D. Widmer, R. Martin, and M. Kimiabeigi, "Electric vehicle traction motors without rare earth magnets," *Sustainable Materials and Technologies*, vol. 3, pp. 7–13, 2015.

[8] US Department of Energy, "Electric Drive Status and Challenges," 2012.

[9] M. Doppelbauer, "Permanent magnet and field winding synchronous versus induction for full-electric vehicles.," May 2014.

[10] "www.mclaren.com."

[11] G. Pellegrino, A. Vagati, P. Guglielmi, and B. Boazzo, "Performance Comparison Between Surface-Mounted and Interior PM Motor Drives for Electric Vehicle Application," *IEEE Transactions on Industrial Electronics*, vol. 59, no. 2, pp. 803–811, 2012.

[12] T. Finken, M. Felden, and K. Hameyer, "Comparison and design of different electrical machine types regarding their applicability in hybrid electrical vehicles," in *18th International Conference on Electrical Machines, 2008. ICEM 2008*, pp. 1–5, Sept. 2008.

[13] "www.coppermotor.com."

[14] P. M. Ehsani, "Switched Reluctance Motor Drives Switched Reluctance Motor Drives for Propulsion and Regenerative Braking regenerative braking in EV and HEV," in *Transportation Technologies for Sustainability* (M. Ehsani, F.-Y. Wang, and G. L. Brosch, eds.), pp. 939–946, Springer New York, 2013.

[15] H. Hannoun, M. Hilairet, and C. Marchand, "Experimental Validation of a Switched Reluctance Machine Operating in Continuous-Conduction Mode," *IEEE Transactions on Vehicular Technology*, vol. 60, no. 4, pp. 1453–1460, 2011.

[16] H. Cheng, H. Chen, and Z. Yang, "Design indicators and structure optimisation of switched reluctance machine for electric vehicles," *IET Electric Power Applications*, vol. 9, no. 4, pp. 319–331, 2015.

[17] N. Ouddah, *Commande robuste d'une machine a reluctance variable pour la traction de vehicules electriques*. PhD thesis, University of Cergy-Pontoise, Sept. 2015.

[18] M. Rekik, M. Besbes, C. Marchand, B. Multon, S. Loudot, and D. Lhotellier, "High-speed-range enhancement of switched reluctance motor with continuous mode for automotive applications," *European Transactions on Electrical Power*, vol. 18, pp. 674–693, Oct. 2008.

[19] H. Hannoun, M. Hilairet, and C. Marchand, "High performance current control of a switched reluctance machine based on a gain-scheduling PI controller," *Control Engineering Practice*, vol. 19, pp. 1377–1386, Nov. 2011.

[20] H. Hannoun, M. Hilairet, and C. Marchand, "Design of an SRM Speed Control Strategy for a Wide Range of Operating Speeds," *IEEE Transactions on Industrial Electronics*, vol. 57, pp. 2911–2921, Sept. 2010.

[21] G. B. Mariani, *Modelisation et reduction par controle-commande des variations de couple des machines synchrones a reluctance*. PhD thesis, G2ELab Laboratory, Grenoble, France.

[22] M. Hamiti, *Reduction des ondulations de couple d'une machine synchrone a reluctance variable : Approches par la structure et par la commande*. PhD thesis, University of Nancy 1, June 2009.

[23] S. Taghavi and P. Pillay, "A Mechanically Robust Rotor with Transverse-Laminations for a Wide Speed Range Synchronous Reluctance Traction Motor," *IEEE Transactions on Industry Applications*, vol. PP, no. 99, pp. 1–1, 2015.

[24] D. Dorrell, A. Knight, M. Popescu, L. Evans, and D. Staton, "Comparison of different motor design drives for hybrid electric vehicles," in *2010 IEEE Energy Conversion Congress and Exposition (ECCE)*, pp. 3352–3359, Sept. 2010.

[25] A. Boglietti and M. Pastorelli, "Induction and synchronous reluctance motors comparison," in *34th Annual Conference of IEEE Industrial Electronics, 2008. IECON 2008*, pp. 2041–2044, Nov. 2008.

[26] A. Boglietti, A. Cavagnino, M. Pastorelli, and A. Vagati, "Experimental comparison of induction and synchronous reluctance motors performance," in *Industry Applications Conference, 2005. Fourtieth IAS Annual Meeting. Conference Record of the 2005*, vol. 1, pp. 474–479 Vol. 1, Oct. 2005.

[27] S. Taghavi and P. Pillay, "A Sizing Methodology of the Synchronous Reluctance Motor for Traction Applications," *IEEE Journal of Emerging and Selected Topics in Power Electronics*, vol. 2, pp. 329–340, June 2014.

[28] B. Multon, "Historique des machines electriques et plus particulierement des machines a reluctance variable," *revue 3EI*, pp. 3–8, 1995.

[29] J. Kostko, "Polyphase Reaction Synchronous Motors," *J. Amer. Inst. Elec. Ing*, vol. 42, pp. 1162–1168, 1923.

[30] T. Lipo, T. Miller, A. Vagati, I. Boldea, L. Malesani, and T. Fukao, "Synchronous reluctance drives tutorial," in *IEEE-IAS Annu. Meeting*, 1994.

[31] D. Staton, T. Miller, and S. Wood, "Maximising the Saliency Ratio of the Synchronous Reluctance Motor," *Electric Power Applications, IEE Proceedings B*, vol. 140, no. 4, pp. 249–259, 1993.

[32] M. Kamper and A. Volsdhenk, "Effect of Rotor Dimensions and Cross Magnetisation on Ld and Lq Inductances of Reluctance Synchronous Machine with Cageless Flux Barrier Rotor," *Electric Power Applications, IEE Proceedings* -, vol. 141, no. 4, pp. 213–220, 1994.

[33] L. Xu, X. Xu, T. Lipo, and D. Novotny, "Vector Control of a Synchronous Reluctance Motor Including Saturation and Iron Loss," *IEEE Transactions on Industry Applications*, vol. 27, no. 5, pp. 977 –985, 1991.

[34] M. Polikarpova, *Liquid Cooling Solutions for Rotating Permanent Magnet Machines*. PhD thesis, Lappeenranta University of Technology, Finland, 2014.

[35] B. Chalmers and L. Musaba, "Design and field-weakening performance of a synchronous reluctance motor with axially laminated rotor," *IEEE Transactions on Industry Applications*, vol. 34, pp. 1035–1041, Sept. 1998.

[36] R. Betz, R. Lagerquist, M. Jovanovic, T. Miller, and R. Middleton, "Control of Synchronous Reluctance Machines," *IEEE Transactions on Industry Applications*, vol. 29, pp. 1110 –1122, Dec. 1993.

[37] F. B. I. Boldea, Lorand Janosi, "A Modified Direct Torque Control (DTC) of Reluctance Synchronous Motor Sensorless Drive," *Electric Machines & Power Systems*, vol. 28, no. 2, pp. 115–128, 2000.

[38] T. Matsuo and T. Lipo, "Field Oriented Control of Synchronous Reluctance Machine," in *24th Annual IEEE Power Electronics Specialists Conference, 1993. PESC '93 Record*, pp. 425 –431, June 1993.

[39] T. Matsuo, A. El-Antably, and T. Lipo, "A New Control Strategy for Optimum Efficiency Operation of a Synchronous Reluctance Motor," in *Conference Record of the 1996 IEEE Industry Applications Conference, 1996. Thirty-First IAS Annual Meeting, IAS '96*, vol. 1, pp. 109–116 vol.1, Oct. 1996.

[40] H.-D. Lee, S.-J. Kang, and S.-K. Sul, "Efficiency-Optimized Direct Torque Control of Synchronous Reluctance Motor using Feedback Linearization," *IEEE Transactions on Industrial Electronics*, vol. 46, pp. 192 –198, Feb. 1999.

[41] R. Morales-Caporal and M. Pacas, "A Predictive Torque Control for the Synchronous Reluctance Machine Taking Into Account the Magnetic Cross Saturation," *IEEE Transactions on Industrial Electronics*, vol. 54, pp. 1161 –1167, Apr. 2007.

[42] P. Fick and M. Kamper, "Accurate digital current control of the reluctance synchronous machine with constant current angle," in *Africon Conference in Africa, 2002. IEEE AFRICON. 6th*, vol. 2, pp. 685–688 vol.2, Oct. 2002.

[43] X. Zhang, G. Foo, D. Vilathgamuwa, and D. Maskell, "An Improved Robust Field-Weakeaning Algorithm for Direct-Torque-Controlled Synchronous-Reluctance-Motor Drives," *IEEE Transactions on Industrial Electronics*, vol. 62, no. 5, pp. 3255–3264, 2015.

[44] M.-Y. Wei and T.-H. Liu, "Design and Implementation of an Online Tuning Adaptive Controller for Synchronous Reluctance Motor Drives," *IEEE Transactions on Industrial Electronics*, vol. 60, pp. 3644–3657, Sept. 2013.

[45] S.-J. Kang and S.-K. Sul, "Highly dynamic torque control of synchronous reluctance motor," *IEEE Transactions on Power Electronics*, vol. 13, no. 4, pp. 793–798, 1998.

[46] K.-K. Shyu and C.-K. Lai, "Incremental Motion Control of Synchronous Reluctance Motor via Multisegment Sliding Mode Control Method," *IEEE Transactions on Control Systems Technology*, vol. 10, pp. 169–176, Mar. 2002.

[47] E. Daryabeigi, H. Abootorabi Zarchi, G. Arab Markadeh, J. Soltani, and F. Blaabjerg, "Online MTPA Control Approach for Synchronous Reluctance Motor Drives Based on Emotional Controller," *IEEE Transactions on Power Electronics*, vol. 30, pp. 2157–2166, Apr. 2015.

[48] T. Matsuo and T. Lipo, "Rotor Position Detection Scheme for Synchronous Reluctance Motor Based on Current Measurements," *IEEE Transactions on Industry Applications*, vol. 31, no. 4, pp. 860–868, 1995.

[49] K. Wang, Z. Zhu, G. Ombach, M. Koch, S. Zhang, and J. Xu, "Optimal Slot/Pole and Flux-Barrier Layer Number Combinations for Synchronous Reluctance Machines," in *2013 8th International Conference and Exhibition on Ecological Vehicles and Renewable Energies (EVER)*, pp. 1–8, Mar. 2013.

[50] A. Vagati, G. Franceschini, I. Marongiu, and G. Troglia, "Design Criteria of High Performance Synchronous Reluctance Motors," in *Conference Record of the 1992 IEEE Industry Applications Society Annual Meeting, 1992*, pp. 66–73 vol.1, 1992.

[51] X. Bomela and M. Kamper, "Effect of stator chording and rotor skewing on performance of reluctance synchronous machine," *IEEE Transactions on Industry Applications*, vol. 38, pp. 91–100, Jan. 2002.

[52] E. Howard, M. Kamper, and S. Gerber, "Flux barrier and skew design optimisation of reluctance synchronous machines," in *2014 International Conference on Electrical Machines (ICEM)*, pp. 1186–1192, Sept. 2014.

[53] T. Matsuo and T. Lipo, "Rotor Design Optimization of Synchronous Reluctance Machine," *IEEE Transactions on Energy Conversion*, vol. 9, pp. 359–365, June 1994.

[54] A. Vagati, "The synchronous reluctance solution: a new alternative in AC drives," in *, 20th International Conference on Industrial Electronics, Control and Instrumentation, 1994. IECON '94*, vol. 1, pp. 1–13 vol.1, Sept. 1994.

[55] R. Moghaddam, F. Magnussen, and C. Sadarangani, "Theoretical and Experimental Reevaluation of Synchronous Reluctance Machine," *IEEE Transactions on Industrial Electronics*, vol. 57, pp. 6–13, Jan. 2010.

[56] P. J. Lawrenson and S. K. Gupta, "Developments in the Performance and Theory of Segmental-Rotor Reluctance Motors," *Electrical Engineers, Proceedings of the Institution of*, vol. 114, no. 5, pp. 645–653, 1967.

[57] A. J. O. Cruickshank, R. W. Menzies, and A. F. Anderson, "Axially Laminated Anisotropic Rotors for Reluctance Motors," *Electrical Engineers, Proceedings of the Institution of*, vol. 113, no. 12, pp. 2058–2060, 1966.

[58] C.-y. Lin, "Equivalent Circuits of Reluctance Machines," *Power Apparatus and Systems, Part III. Transactions of the American Institute of Electrical Engineers*, vol. 71, no. 1, pp. 1–9, 1952.

[59] A. Tessarolo, M. Degano, and N. Bianchi, "On the analytical estimation of the airgap field in synchronous reluctance machine," in *2014 International Conference on Electrical Machines (ICEM)*, pp. 239–244, Sept. 2014.

[60] J. Ikaheimo, J. Kolehmainen, T. Kansakangas, V. Kivela, and R. Moghaddam, "Synchronous High-Speed Reluctance Machine With Novel Rotor Construction," *IEEE Transactions on Industrial Electronics*, vol. 61, pp. 2969–2975, June 2014.

[61] T. Satou, S. Morimoto, M. Sanada, and Y. Inoue, "A Study on the Rotor Design of the Synchronous Reluctance Motor for EV and HEV Propulsion," in *2013 IEEE 10th International Conference on Power Electronics and Drive Systems (PEDS)*, pp. 1190–1194, Apr. 2013.

[62] S. Rick, M. Felden, M. Hombitzer, and K. Hameyer, "Permanent Magnet Synchronous Reluctance Machine - Bridge Design for Two-Layer Applications," in *Electric Machines Drives Conference (IEMDC), 2013 IEEE International*, pp. 1376–1383, May 2013.

[63] R.-R. Moghaddam, F. Magnussen, and C. Sadarangani, "Novel rotor design optimization of Synchronous Reluctance Machine for low torque ripple," in *2012 XXth International Conference on Electrical Machines (ICEM)*, pp. 720–724, Sept. 2012.

[64] N. Bianchi, S. Bolognani, D. Bon, and M. Pre, "Rotor Flux-Barrier Design for Torque Ripple Reduction in Synchronous Reluctance and PM-Assisted Synchronous Reluctance Motors," *IEEE Transactions on Industry Applications*, vol. 45, no. 3, pp. 921–928, 2009.

[65] N. Bianchi, S. Bolognani, D. Bon, and M. Dai Pre, "Torque Harmonic Compensation in a Synchronous Reluctance Motor," *IEEE Transactions on Energy Conversion*, vol. 23, pp. 466–473, June 2008.

[66] A. Vagati, M. Pastorelli, G. Franceschini, and C. Petrache, "Design of Low-Torque-Ripple Synchronous Reluctance Motors," in *, Conference Record of the 1997 IEEE Industry Applications Conference, 1997. Thirty-Second IAS Annual Meeting, IAS '97*, vol. 1, pp. 286–293 vol.1, Oct. 1997.

[67] J. M. Park, S. I. Kim, J. P. Hong, and J. H. Lee, "Rotor Design on Torque Ripple Reduction for a Synchronous Reluctance Motor With Concentrated Winding Using Response Surface Methodology," *IEEE Transactions on Magnetics*, vol. 42, pp. 3479–3481, Oct. 2006.

[68] M. Sanada, K. Hiramoto, S. Morimoto, and Y. Takeda, "Torque ripple improvement for synchronous reluctance motor using an asymmetric flux barrier arrangement," *IEEE Transactions on Industry Applications*, vol. 40, pp. 1076–1082, July 2004.

[69] P. Alotto, M. Barcaro, N. Bianchi, and M. Guarnieri, "Optimization of Interior PM Motors With Machaon Rotor Flux Barriers," *IEEE Transactions on Magnetics*, vol. 47, no. 5, pp. 958–961, 2011.

[70] R. Moghaddam, F. Magnussen, and C. Sadarangani, "Novel rotor design optimization of synchronous reluctance machine for high torque density," in *6th IET International Conference on Power Electronics, Machines and Drives (PEMD 2012)*, pp. 1–4, Mar. 2012.

[71] F. Cupertino, G.-M. Pellegrino, E. Armando, and C. Gerada, "A SyR and IPM machine design methodology assisted by optimization algorithms," in *2012 IEEE Energy Conversion Congress and Exposition (ECCE)*, pp. 3686–3691, Sept. 2012.

[72] J. Mathews and R. Howell, *Complex Analysis for Mathematics and Engineering*. Jones & Bartlett Publishers, 2012.

[73] B. NOGAREDE, "Machines tournantes : principes et constitution," *Techniques de l'ingenieur Generalites sur les machines electriques tournantes*, vol. base documentaire : TIB250DUO., Feb. 2001. fre.

[74] R. R. Moghaddam, F. Magnussen, and C. Sadarangani, "Novel Rotor Design Optimization of Synchronous Reluctance Machine for High Torque Density," in *6th IET International Conference on Power Electronics, Machines and Drives (PEMD 2012)*, pp. 1–4, Mar. 2012.

[75] R.-R. Moghaddam and F. Gyllensten, "Novel High-Performance SynRM Design Method: An Easy Approach for A Complicated Rotor Topology," *IEEE Transactions on Industrial Electronics*, vol. 61, pp. 5058–5065, Sept. 2014.

[76] E. Armando, P. Guglielmi, G. Pellegrino, M. Pastorelli, and A. Vagati, "Accurate Modeling and Performance Analysis of IPM-PMASR Motors," *IEEE Transactions on Industry Applications*, vol. 45, pp. 123–130, Jan. 2009.

[77] A. Vagati, B. Boazzo, P. Guglielmi, and G. Pellegrino, "Ferrite assisted synchronous reluctance machines: A general approach," in *2012 XXth International Conference on Electrical Machines (ICEM)*, pp. 1315–1321, Sept. 2012.

[78] P. Guglielmi, N. Giraudo, G. Pellegrino, and A. Vagati, "P.M. assisted synchronous reluctance drive for minimal hybrid application," in *Conference Record of the 2004 IEEE Industry Applications Conference, 2004. 39th IAS Annual Meeting*, vol. 1, pp. –306, Oct. 2004.

[79] T. A. Lipo, "Synchronous Reluctance Machines-A Viable Alternative for AC Drives?," *Electric Machines & Power Systems*, vol. 19, pp. 659–671, Nov. 1991.

[80] A. Vagati, "Synchronous Reluctance Electrical Motor having a Low Torque-Ripple Design," Oct. 1998. U.S. Classification: 310/185; 310/152; 310/163; 310/211; 310/216.107 International Classification: H02K 1926; H02K 2100; H02K 2302.

[81] M. Gamba, G. Pellegrino, and F. Cupertino, "Optimal number of rotor parameters for the automatic design of Synchronous Reluctance machines," in *2014 International Conference on Electrical Machines (ICEM)*, pp. 1334–1340, Sept. 2014.

[82] G. Bertotti, "General properties of power losses in soft ferromagnetic materials," *IEEE Transactions on Magnetics*, vol. 24, pp. 621–630, Jan. 1988.

[83] G. Pellegrino and F. Cupertino, "FEA-based multi-objective optimization of IPM motor design including rotor losses," in *2010 IEEE Energy Conversion Congress and Exposition (ECCE)*, pp. 3659–3666, Sept. 2010.

[84] E. Semail, X. Kestelyn, and A. Bouscayrol, "Right harmonic spectrum for the back-electromotive force of an n-phase synchronous motor," in *Conference Record of the 2004 IEEE Industry Applications Conference, 2004. 39th IAS Annual Meeting*, vol. 1, p. 78, Oct. 2004.

[85] E. Semail, A. Bouscayrol, and J.-P. Hautier, "Vectorial formalism for analysis and design of polyphase synchronous machines," *The European Physical Journal - Applied Physics*, vol. 22, pp. 207–220, June 2003.

[86] F. Colamartino, C. Marchand, and A. Razek, "Torque ripple minimization in permanent magnet synchronous servodrive," *IEEE Transactions on Energy Conversion*, vol. 14, pp. 616–621, Sept. 1999.

[87] L. Xu and W. Fu, "Evaluation of third harmonic component effects in five-phase synchronous reluctance motor drive using time-stepping finite-element method," *IEEE Transactions on Industry Applications*, vol. 38, no. 3, pp. 638–644, 2002.

[88] H. Toliyat, M. Rahimian, and T. Lipo, "dq modeling of five phase synchronous reluctance machines including third harmonic of air-gap MMF," in *, Conference Record of the 1991 IEEE Industry Applications Society Annual Meeting, 1991*, pp. 231–237 vol.1, Sept. 1991.

[89] H. Toliyat, S. Waikar, and T. Lipo, "Analysis and simulation of five-phase synchronous reluctance machines including third harmonic of airgap MMF," *IEEE Transactions on Industry Applications*, vol. 34, pp. 332–339, Mar. 1998.

[90] S.-S. Liou, H. Woodson, and J. Hsu, "Steady-state performance of reluctance motors under combined fundamental and third-harmonic excitation. I. Theoretical analysis," *IEEE Transactions on Energy Conversion*, vol. 7, pp. 192–201, Mar. 1992.

[91] J. Hsu, S.-S. Liou, and H. H. Woodson, "Peaked-MMF smooth-torque reluctance motors," *IEEE Transactions on Energy Conversion*, vol. 5, pp. 104–109, Mar. 1990.

[92] H. Toliyat, L. Xu, and T. Lipo, "A five-phase reluctance motor with high specific torque," *IEEE Transactions on Industry Applications*, vol. 28, pp. 659–667, May 1992.

[93] L. Xu, "Rotor structure selections of nonsine five-phase synchronous reluctance machines for improved torque capability," *IEEE Transactions on Industry Applications*, vol. 36, pp. 1111–1117, July 2000.

[94] R. Shi, H. Toliyat, and A. El-Antably, "Field oriented control of five-phase synchronous reluctance motor drive with flexible 3/sup rd/ harmonic current injection for high specific torque," in *Conference Record of the 2001 IEEE Industry Applications Conference, 2001. Thirty-Sixth IAS Annual Meeting*, vol. 3, pp. 2097–2103 vol.3, Sept. 2001.

[95] J. Coulomb, "A methodology for the determination of global electromechanical quantities from a finite element analysis and its application to the evaluation of magnetic forces, torques and stiffness," *IEEE Transactions on Magnetics*, vol. 19, pp. 2514–2519, Nov. 1983.

[96] N. L. Schmitz and D. W. Novotny, *Introductory electromechanics*. Ronald Press, 1965.

[97] I. Tabatabaei, J. Faiz, H. Lesani, and M. T. Nabavi-Razavi, "Modeling and Simulation of a Salient-pole Synchronous Generator with Dynamic Eccentricity using Modified Winding Function Theory," *IEEE Transactions on Magnetics*, vol. 40, no. 3, pp. 1550–1555, 2004.

[98] J. Gojko, D. Momir, and O. Aleksandar, "Skew and Linear Rise of MMF across Slot Modelling-Winding Function Approach," *IEEE Transactions on Energy Conversion*, vol. 14, no. 3, pp. 315–320, 1999.

[99] L. Xu, F. Liang, and T. Lipo, "Transient Model of a Doubly Excited Reluctance Motor," *IEEE Transactions on Energy Conversion*, vol. 6, no. 1, pp. 126–133, 1991.

[100] N. Al-Nuaim and H. Toliyat, "A novel method for modeling dynamic air-gap eccentricity in synchronous machines based on modified winding function theory," *IEEE Transactions on Energy Conversion*, vol. 13, no. 2, pp. 156–162, 1998.

[101] J. Faiz and I. Tabatabaei, "Extension of winding function theory for nonuniform air gap in electric machinery," *IEEE Transactions on Magnetics*, vol. 38, pp. 3654–3657, Nov. 2002.

[102] T. Lubin, T. Hamiti, H. Razik, and A. Rezzoug, "Comparison Between Finite-Element Analysis and Winding Function Theory for Inductances and Torque Calculation of a Synchronous Reluctance Machine," *IEEE Transactions on Magnetics*, vol. 43, no. 8, pp. 3406–3410, 2007.

[103] P. Neti and S. Nandi, "Determination of effective air-gap length of synchronous reluctance motors (SynchRel) from experimental data," *IEEE Transactions on Industry Applications*, vol. 42, pp. 454–464, Mar. 2006.

[104] A. Tessarolo, M. Mezzarobba, and M. Degano, "Analytical calculation of air-gap armature reaction field including slotting effects in fractional-slot concentrated-coil SPM multiphase machines," in *2011 International Conference on Power Engineering, Energy and Electrical Drives (POWERENG)*, pp. 1–6, 2011.

[105] A. Tessarolo, "Accurate Computation of Multiphase Synchronous Machine Inductances Based on Winding Function Theory," *IEEE Transactions on Energy Conversion*, vol. 27, no. 4, pp. 895–904, 2012.

[106] R. Park, "Two-reaction theory of synchronous machines generalized method of analysis-part I," *American Institute of Electrical Engineers, Transactions of the*, vol. 48, pp. 716–727, July 1929.

[107] R. Park, "Two-reaction theory of synchronous machines-II," *American Institute of Electrical Engineers, Transactions of the*, vol. 52, pp. 352–354, June 1933.

[108] S. Yammine, M. Fadel, D.-M. Nguyen, D. Harribey, and L. Albert, "(in press) Phase Current Control of a Two Phase Synchronous Reluctance Machine.," in *41st Annual Conference of the IEEE Industrial Electronics Society IECON*, Nov. 2015.

[109] M. Kamper, F. van der Merwe, and S. Williamson, "Direct finite element design optimisation of the cageless reluctance synchronous machine," *IEEE Transactions on Energy Conversion*, vol. 11, pp. 547–555, Sept. 1996.